2010-12-16

Modeling of Flow in an In Vitro Aneurysm Model: A Fluid-Structure Interaction Approach

Qing Hao
University of Miami, q.hao@umiami.edu

UNIVERSITY OF MIAMI

MODELING OF FLOW IN AN IN VITRO ANEURYSM MODEL: A FLUID-STRUCTURE INTERACTION APPROACH

By

Qing Hao

A DISSERTATION

Submitted to the Faculty
of the University of Miami
in partial fulfillment of the requirements for
the degree of Doctor of Philosophy

Coral Gables, Florida

December 2010

UNIVERSITY OF MIAMI

A dissertation submitted in partial fulfillment of
the requirements for the degree of
Doctor of Philosophy

MODELING OF FLOW IN AN IN VITRO ANEURYSM MODEL: A FLUID-STRUCTURE INTERACTION APPROACH

Qing Hao

Approved:

_____ Baruch B. Lieber, Ph.D. Professor of Bimedical Engineering	_____ Terri A. Scandura, Ph.D. Dean of the Graduate School
_____ Weiyong Gu, Ph.D. Professor of Bimedical Engineering	_____ Chun-Yuh Huang, Ph.D. Assistant Professor of Biomedical Engineering

_____
Danny Bluestein, Ph.D.
Professor of Biomedical Engineering
SUNY Stony Brook

HAO, QING (Ph.D., Biomedical Engineering)

Modeling of Flow in an vitro Aneurysm Model: (December 2010)
A Fluid-Structure Interaction Approach

Abstract of a dissertation at the University of Miami.

Dissertation supervised by Professor Baruch B. Lieber
No. of pages in text. (111)

Flow velocity field, vorticity and circulation and wall shear stresses were simulated by FSI approach under conditions of pulsatile flow in a scale model of the rabbit elastin-induced aneurysm. The flow pattern inside the aneurysm sac confirmed the in vitro experimental findings that in diastole time period the flow inside the aneurysm sac is a stable circular clock-wise flow, while in systole time period higher velocity enters into the aneurysm sac and during systole and diastole time period an anti-clock circular flow pattern emerged near the distal neck; in the 3-D aneurysm sac, the kinetic energy per point is about 0.0002 (m2/s2); while in the symmetrical plane of the aneurysm sac, the kinetic energy per point is about 0.00024 (m2/s2). In one cycle, the shape of the intraaneurysmal energy profile is in agreement with the experimental data; The shear stress near the proximal neck experienced higher shear stress (peak value 0.35 Pa) than the distal neck (peak value 0.2 Pa), while in the aneurysm dome, the shear stress is always the lowest (0.0065 Pa). The ratio of shear stresses in the proximal neck vs. distal neck is around 1.75, similar to the experimental findings that the wall shear rate ratio of proximal neck vs. distal neck is 1.5 to 2.

ACKNOWLEDGEMENTS

I would like to thank Dr. Baruch B. Lieber for his invaluable guidance and advising throughout this journey. I would have not finished without his help.

I also would like to thank Adina staff for their technical support and help in the email communications. Special thanks go to the members of our research group in Miami for the discussions.

Finally, my profound thanks to my family, my father, Hao Chuanjing, and my mother, Xiao Guifang for their support, patience and love.

TABLE OF CONTENTS

LIST OF FIGURES

LIST OF TABLES

CHAPTER 1. INTRODUCTION

1.1 Stroke and Cerebral Aneurysm

Stroke is the most common life-threatening neurological disease, the leading cause of adult disability, and the third leading cause of death. In the United States alone, about 795,000 people experience a new or recurrent stroke annually (about 600,000 of these are first attacks). Of all strokes, 87 percent are ischemic, 10 percent are intracerebral hemorrhage, and 3 percent are subarachnoid hemorrhage. According to the 2009 AHA report, stroke mortality was 143,579 (56,586 males, 86,993 females), accounting for about one of every 17 deaths in the United States. When considered separately from other cardiovascular diseases, stroke ranks No. 3 among all causes of death, behind diseases of the heart and cancer. The estimated direct and indirect cost of stroke for 2009 is $68.9 billion [AHA, 2009].

Ischemic stroke results primarily from proximal originating emboli, such as ventricular or atrial thrombi, that are dislodged and travel to the cerebral circulation. In addition ischemic stroke can result from intracranial atherosclerosis, although it is estimated that only about 10% of ischemic strokes in the western hemisphere are due to intracranial atherosclerosis. Atherosclerotic lesions are composed of fat, cholesterol, and other substances that collect on the wall of the arteries to form a sticky plaque. Over time, the plaque builds up and impedes the flow of blood through the vessel, which can cause the blood to clot. If the clot

breaks loose and moves through the blood vessels to the brain it will cause a cerebral embolism.

Hemorrhagic stroke occurs when a cerebral blood vessel bursts bleeding into the brain. The brain is very sensitive to bleeding and damage can occur very rapidly. Bleeding irritates the brain tissue, causing swelling. Bleeding also increases pressure on the brain and presses it against the skull. Hemorrhagic strokes are grouped as intracerebral hemorrhage and subarachnoid hemorrhage (SAH) according to location of the blood vessel.

Subarachnoid hemorrhage is bleeding in the subarachnoid space - the area between the arachnoid membrane and the pia mater surrounding the brain. Subarachnoid hemorrhage occurs due to rupture of a cerebral aneurysm or head injury. Intracerebral hemorrhage is bleeding in the brain caused by a blood vessel rupture in the head. It can be caused by abnormalities of the blood vessels (aneurysm or vascular malformation); or high blood pressure (hypertensive intracerebral hemorrhage); or protein deposits along blood vessels (amyloid angiopathy); or traumatic brain injury.

In the cerebral circulation, blood enters the cranial vault under arterial pressure through the left and right internal carotid arteries and the left and right vertebral arteries. The vertebral arteries join to makeup the basilar artery forming the posterior circulation. Each internal carotid artery divides to become the anterior cerebral artery (ACA) and the middle cerebral artery (MCA) forming the anterior circulation. The anterior and posterior circulations join via the posterior communicating arteries (PCoA) at the circle of Willis, which lies at the base of

the brain, within the subarachnoid space. Aneurysms can occur at any of the cerebral vasculature branch points; however, 90% of them occur at the circle of Willis. An aneurysm is defined as a localized pathological dilatation of an artery. Cerebral aneurysms are generally asymptomatic but when they burst the consequences are in most cases severe neurological deficits and fatality. [Kassell, 1990, ISAT Collaborative Group, 2002]

The ACA is the most common site of ruptured aneurysms, followed by the MCA and the posterior circulation [Brisman, 2006]. Aneurysms in the internal carotid artery (ICA) are most often encountered at the origin of the PCoA, followed by the carotid bifurcation, and the origin of the ophthalmic artery. Few aneurysms are located in the cavernous portion of the ICA. However, approximately 10% of giant aneurysms (larger than 25 mm in diameter) are located in the cavernous segment. Multiple aneurysms are found in 20% to 30% of patients with SAH that results from aneurysm rupture. [Kassel, 1990]

The risk of rupture for intact aneurysms is approximately 1% to 2% per year. At least 15% of patients die after the initial hemorrhage. For patients who survive acute hemorrhage, the mortality rate during the first 2 weeks is 20% to 30% and the morbidity rate is about 20%. Rebleeding is a major cause of death and disability in untreated patients. The risk of rebleeding during the first 2 weeks after hemorrhage is approximately 20%, increases to 33% at 1 month and 50% at 6 months. Mortality from the second hemorrhage is approximately 40% to 50%. Thus, the need for therapeutic intervention is obvious. [Wakhloo, 1998]

1.2 Current Treatment of Cerebral Aneurysm

Current treatment options for cerebral aneurysm are surgical clipping, endovascular embolization including coiling and onyx, stent-assistant coiling and flow diversion. Modern microsurgical and anesthetic techniques and improved anesthetic agent have enabled the direct clipping of some giant intracranial aneurysms. Depending upon where the aneurysm is located, an incision is typically made behind the hairline or on the back of the head. Next, a section of bone, or bone plate, is removed from the skull. The surgeon approaches the aneurysm in the cleft between the skull and the brain and not through brain tissue. Under a microscope, the aneurysm is then carefully separated from the normal blood vessels and brain. The aneurysm is then completely obliterated with a tiny metal clip. This keeps blood from entering the aneurysm. As a result, future bleeding is prevented and nearby brain tissue is protected from further damage. The bone plate is then wired securely into place and the wound is closed.

Endovascular coiling of cerebral aneurysm include the delivery of small metallic coils into the aneurysm sac through a microcatheter that are detached by electrolyzing a fusible metal. Since all the intervention is performed through the introduction of a catheter in the femoral artery, avoiding open head surgery, this approach is minimally invasive. Technical improvements in microcatheter and coil technology extended the range of treatable aneurysms using endovascular approach so that it is feasible to manage 80 to 90% of intracranial aneurysms [Mitchell, 2004]

Minimally invasive approaches for aneurysm treatment have focused on primary endosaccular (intra-aneurysmal) occlusion via balloon and/or coil technologies, with no regard for the pathology of the aneurysm-parent vessel complex. Aneurysm therapy using retrievable coils is considered at present a valid alternative to direct surgical exclusion, especially for high-risk patients. The rational for this approach is to reduce flow within the aneurysm through the implantation of platinum coils. Ideally, the alteration of flow should promote the formation of a stable thrombus initially, maturing to an organized one within a few weeks, with the eventual exclusion of the aneurysm from the circulation. Endovascular treatment of aneurysm has been proven successful in numerous trials. However, complications such as aneurysm perforation, recanalization, parent artery occlusion, and cerebral embolization still persist. Thrombus generated at the irregular surface of the aneurysm entrance may lead to parent artery occlusion or embolic showers. Aneurysm perforation may occur during catheterization or the placement of coils into the aneurysm. Preexisting thrombus within the aneurysm sac may be sheared off into the parent trunk. In addition, coil movement and compaction which occurs several months after their placement may foster aneurysm revascularization or regrowth [Wakhloo, 1998]. Intrinsic technical limitations (e.g., coil flexibility, shape, and dimensions) prevent the tight packing of aneurysms, especially those with wide necks, without compromising the parent artery. Clearly, novel approaches are required for a safer, more definitive endovascular treatment of aneurysms.

A liquid embolic material, Onyx was approved by FDA in United States for the treatment of intracranial aneurysms. This material is an ethylene vinyl alcohol copolymer dissolved in the organic solvent dimethyl sulfoxide (DMSO) and opacified to x-rays with tantalum powder. Once coming into contact with an ionic solution the DMSO dissipates and the Onyx solidifies into a spongy, cohesive material. It is delivered to the aneurysm via a microcatheter placed inside the aneurysm after the neck of the aneurysm is temporarily occluded by a balloon, which reduces the risk of the copolymer exiting the aneurysm and entering the native circulation [Lubicz, 2005; Cekirge, 2006; Simmon, 2010; Wolfe, 2010]. Also there is report that metallic embolization coils were combined with the Onyx liquid embolic agent in the aneurysm sac to achieve a more durable result after endovascular treatment. This therapeutic procedure was performed in selected cases in which, based on the authors' experiences, either coil embolization or Onyx alone would likely have failed [Cekirge, 2007]. Wide-necked cerebral aneurysms still represents a challenging problem. Instead of coiling alone, clinicians can combine a neuroform microstent (Boscton Scientific Inc., Natick, MA) or the Enterpise stent (Codman J&J, Raynham, MA) with coils to provide a solution the treatment of unruptured wide-necked cerebral aneurysms [Simmon, 2010]. However, delayed spontaneous asymptomatic occlusion of the parent vessel occurred in two patients which were detected on routine follow-up was reported [Cekirge, 2006]. There is another report that the Onyx mass within the aneurysm was removed from patient after endovascular treatment of an

unruptured giant posterior communicating artery aneurysm with Onyx due to mass effect and compression on the right cerebral peduncle [Van Loock, 2009].

1.3 Development of Flow Diverters

In early 90s, a few investigators suggested to use intravascular, porous, metallic stents that will act as flow diverters to occlude carotid and vertebral artery aneurysms while preserving the parent vessel [Wakhloo 1994, Geremia 1994]. The idea was that stents will redirect flow away from the aneurysm sac and the sluggish flow within the aneurysm will promote thrombosis of the aneurysm followed by formation of a thin layer of neointima that will cover the luminal surface of the stent and thus exclude the aneurysm from the circulation. After some preliminary testing of the idea in laboratory animal models of aneurysms it became apparent that the concept works some of the times but not in other times and an optimization of the design properties of the device such as porosity, filament diameter and number of filaments is needed to achieve high, repeatable aneurysm occlusion rate.

A preliminary laser-induced fluorescence (LIF) study was conducted to qualitatively assess the potential of existing stents to act as flow diverters in sufficiently alter intra-aneurysmal flow [Lieber, 1997 & 2002]. Pulsatile flow patterns in an experimental flow apparatus were visualized by injecting fluorescing rhodamine dye that was excited by an argon ion laser. The test cells consisted of a rectangular flow channel with a sidewall aneurysm model. The

dimensions of the model were designed to coincide with experimentally created side-wall, venous pouch aneurysm in the canine. A rectangular flow channel rather than a circular tube was employed to obtain a longitudinal view of flow inside the aneurysm and in the parent vessel before and after flow diverter placement. This experiment examined the impact of woven nitinol stents of various porosities on the intra-aneurysmal flow patterns at two different flow conditions in the parent artery; namely, high and low hemodynamic settings. Four stents with porosities ranging from 76% to 85% were utilized. The high hemodynamic settings were those typically found in large arteries (e.g., the carotid artery) where as low hemodynamic settings represented smaller arteries (e.g., the vertebral artery). The hemodynamic conditions were described in terms of the dimensionless dynamic similarity parameters, i.e., the Reynolds and Womersley numbers. These experiments demonstrated that the tested devices did not have an appreciable effect on the intraaneurismal flow for the high hemodynamic setting. However, for the low hemodynamic setting the presence of the stent partially decoupled aneurismal flow from that of the parent vessel and reduced momentum exchange between the two. These observations provided a proof of concept that stenting alone dramatically alters intra-aneurysmal flow patterns. Further, it provided the understanding that the device properties have to be tailored to the local hemodynamics to achieve the desired decoupling.

In a subsequent study the effect of flow diversion on intra-aneurysmal flow patterns was investigated quantitatively using Particle Image Velocimetry (PIV) in a side-wall aneurysm model [Lieber, 1998 & 2002; Liou, 2004]. The test

cell, now with a cylindrical parent artery and a spherical sidewall aneurysm and was designed to complement the previous LIF studies and determine quantitatively the effect of stent filament diameter on intra-aneurysmal vorticity. Pulsatile flow over three helical stents with 76% porosity but different filament sizes was studied. Intra-aneurysmal vorticity was evaluated and the hydrodynamic circulation was subsequently calculated as the surface integral of the vorticity. The results show that flow the diverter altered intra-aneurysmal flow patterns considerably (Figure 1-1). Substantial reduction of intra-aneurysmal vorticity was observed for all the stented cases studied. The mean hydrodynamic circulation inside the aneurysm was reduced to less than 3% for all stented cases when compared to the nonstented case. By reducing the filament diameter, for constant porosity, a further reduction of the mean circulation of up to 30% was obtained. All the flow diverter studied in the PIV experiments, demonstrated that the pattern of the intra-aneurysmal flow changes significantly after device implantation. The typical vortex seen in the nonstented case was no longer present after device placement. It broke down into small vortices, which changed in shape and intensity depending on flow conditions. After stenting, intra-aneurysmal vortical flow activity was decreased to a slow counterclockwise (entering from the proximal neck) motion close to the flow diverter filaments. Fluid motion at the aneurysm dome was barely noticeable, showing that fluid in that region is virtually stagnant.

Concurrent with the PIV experiments, quantification of intra-aneurysmal velocity patterns was explored using computational models. Changes in local

hemodynamics due to flow diverter placement in an aneurysm model were examined computationally in a three-dimensional configuration using a commercial software package FIDAP (Distributed by Fluent Inc., Lebanon, NH). The aneurysm model was designed to replicate the model used in the PIV experiments, namely a cylindrical tube with a spherical sidewall aneurysm. The model was studied under incompressible, pulsatile, viscous, Newtonian conditions with rigid boundaries. The fluid dynamic similarity parameters were set to be representative of large cerebral arteries.

The results of the computational fluid dynamics (CFD) simulations of flow diversion versus the control showed substantial differences in flow patterns inside the aneurismal pouch (Figure 1-2). Higher shear rates were observed at the distal aneurysm neck after stenting, but were confined to a smaller region and were unidirectional compared to the nonstented model. Flow activity inside the stented aneurysm model was significantly diminished and flow inside the parent vessel was less undulated and directed past the orifice. The last observation highlights another advantage of CFD. Using computational methods, it is possible to examine the flow behavior in the parent vessel in a three dimensional configuration subsequent to stenting. Experimentally it is difficult to investigate the flow field inside the parent vessel after stenting due to the obstruction of the field of view by the interposed stent.

Results obtained with the CFD simulations compared favorably with the PIV experimental data. The simulations showed that the flow activity inside the aneurysm pouch is of an order of magnitude smaller than inside the parent vessel

and it is further reduced after stenting. The characteristic flow pattern of nonstented aneurysms, that include distal inflow and proximal outflow from the sac through the main part of the pulse and reverse formation during the acceleration phase of systole, could no longer be found after stenting. Also, the growing undulated vortex, which dominated nonstented aneurismal flow, was abolished after stenting. The observed flow reduction inside the aneurysm due to stenting and the restriction of mass and momentum exchange between the fluids trapped inside the sac and parent vessel flow contributed to the promotion of flow stasis in the dome. The maximum flow rate into the nonstented aneurysm took place during systole. At minimum flow rate in the parent vessel the aneurismal vortex was drawn into the parental vessel. This action was responsible for large fluctuations in magnitude and direction of the wall shear stress, particularly close to the distal part of the ostium. Consequently, this was the location where the highest shear rate values occur in both models.

Various animal models have been employed over the last few decades to investigate various aspects of human brain aneurysms including, genesis, growth and rupture. More recently larger animals have been employed to investigate various minimally invasive devices for aneurysm exclusion for the circulation. The elastase induced aneurysm at the proximal end of the right common carotid artery of the New Zealand White Rabbit has recently emerged as the most widely acceptable model for studying treatment modalities for aneurysms [1997 & 1998 Miskolczi; 1999 Cloft]. The rabbit model has several advantages which makes it the most attractive model. The created aneurysms are similar in size and

geometric features to human intracranial aneurysms, the coagulation cascade and the pH of the blood in that species is the most similar to humans among none-primates. In addition this model is an arterial model which means that there is no suture line at the neck of the aneurysm. Because of its location, the aneurysm is subjected to high shear stresses similar to ophthalmic aneurysms in humans. It has also been found that the elastic lamina in the wall of these experimental aneurysms is markedly reduced just as it is in human aneurysms. Limitation of this model is that the Reynolds and Womersley numbers in the rabbit parent artery are about 2 to 3 times the corresponding values in human cerebral vessels. Other models are constructed using vein pouches sutured onto a hole which is punched in the arterial wall (usually common carotid). The advantage of the surgical approach using a vein pouch is that various parent vessel-aneurysm configurations (lateral, bifurcation, terminal) can be constructed using different anastomoses (side-to-side, end-to-side). Another advantage of this model is the short turnaround time required for its completion and it is preferred by companies for testing deployment methodologies of devices. However, these models are not suitable for investigating the inflammatory response to the implant and scar tissue formation around the neck due to the suture line. Another limitation is that the aneurysm sac itself is made of vein tissue such that the vascular response to the implant is unlike the response of arterial tissue [Stehbens, 1997].

In an effort to optimize flow diverting devices before implantation in the animal Seong et al, [2007] conducted a bench top flow dynamics experiment on a series of six flow diverters that were tested in an elastomeric replica of the

elastase induced aneurysm in rabbit. The geometry of the model wes designed to be an averaged representative of the anatomy of elastase-induced saccular aneurysm model in rabbit scaled up by a factor of 1.36. The silicone model was incorporated into a mock circulation loop and a programmable reciprocating piston pump (CompuFlow 1000MR, Shelly medical imaging technology, Ontario, Canada) was used to simulate the rabbit aortic flow wave forms. The compliant model was placed in a fluid filled rectangular Plexiglas box. The fluid in the box around the model was of the same properties as the working fluid to facilitate an optical path free of distortion. The model was subjected to the pulsatile flow and images were obtained with a charge coupled device (CCD) camera. The distensibility of the ascending aorta was determined from the images by measuring changes in the caliber of the vessel between systole and diastole. An average wall thickness of 0.6 mm yielded about 10% change in the caliber of the ascending aorta of the silicone model between systole and diastole. An aqueous glycerol mixture consisting of 41 parts water and 59 parts pure glycerin by volume was used to obtain a working fluid with a refractive index of 1.411, which matches that of the elastomer model. Flow through the model was analyzed using a PIV system (TSI Inc., Shoreview, MN). Six different diverters were implanted in the model to investigate the influence of the flow diverters on intraaneurysmal flow activity. The nominal diameter of all the flow diverters was 5.5 mm and three nominal porosities of 65%, 70%, and 75% were tested. For each porosity, there were two devices, one with low and one with high (about twice as high) pore density.

The findings of that study can be briefly summarized as follows. The mean hydrodynamic circulation after implanting the diverters was reduced to 14% or less of the mean hydrodynamic circulation before implantation. Mean kinetic energy in the aneurysm was reduced to 29% or less of its value in the control. Overall, a high pore density flow diverter with 70% porosity (Diverter No. 4) yielded the best reduction of flow activity in the aneurysm of the six diverters investigated in this study. The mean flow rate in the representative large perforator (the vertebral artery) after diverter placement in the parent artery across its origin was not markedly compromised compared to the control. The cycle averaged flow rate in the vertebral artery after jailing remained more than 86% of its flow rate before placement of the diverter. Local wall shear rate (WSR) in the aneurysm did not change appreciably after implantation of the diverters.

A flow diverter, although it looks like a stent, its purpose is markedly different in purpose and structure. Stents are porous, tubular devices constructed of metal or synthetic filaments. Endovascular stenting involves the percutaneous placement of the stent device into the lumen of a blood vessel to prevent its abrupt closure. The goal of stent therapy is to maintain blood flow through the dilated vessel and to prevent restenosis. The main purpose of the stent is to oppose the elastic recoil of the vessel wall and to cover the disrupted intimal surface. The efficiency of vessel expansion through stent implantation depends on the intrinsic and spontaneous radial expansive force of the stent, the diameter of the recipient vessel, and the intrinsic mural pressure of the vascular wall itself. In plastically deformable (balloon-expandable) stents, effective vessel expansion is also related

to the dilatation capability and diameter of the balloon itself, whereas elastic (self-expanding) stents provide a secondary, delayed radial expansion that defines the ultimate diameter of the vessel. This, however, is not the purpose of a flow diverter that is used in the treatment of intracranial aneurysms.

The purpose of flow diverters is to redirect blood flow away from the aneurysm and re-establish physiological flow conditions in the parent vessel. Vital side branches (perforators) covered by the flow diverter, however, are not obliterated. This is due to the fact that the pressure gradient across the mesh is sufficient to keep the side branches open. The lack of an outlet from an aneurysm, on the other hand, requires only redirection of the flow to achieve stasis within. Therefore, due to their different purpose, the design requirements of a flow diverter as a vascular graft are vastly different from those of a stent. Compliance matching of the vessel wall and the vascular graft, especially for small diameter arteries, is believed to be important for the endothelial response of the artery and long term patency. In addition, current, stiff stents may lead to vessel kinking with diminishing flow through the stented segment, particularly in tortuous, dilated vessels.

1.4 The Study Goal

When evaluating flow changes in an aneurysm as a result of changes in device parameters such as porosity, pore density and filament diameter, we can apply either experimental or computational techniques. Compared to experiments,

computations have an advantage in terms of cost and they can reveal information that is either unavailable or limited in experiments. For example, in PIV experiments, once the flow diverter is implanted, the flow inside parent artery through the device is concealed by the diverter. Another advantage of computations is that they afford parametric studies with relative ease. For the past 30 years (CFD) has been developed into a mature science and it has been a powerful tool in engineering design. However, most engineering applications do not require the elucidation of the interaction between the fluid and its confining boundaries which is not the case of blood flow in arteries where the viscoelastic properties of the arteries and their mechanical interaction with the pressurized flowing blood are important. In addition, the interaction between an elastic bioimplant and the surrounding vasculature is important as well.

In the past, due to the high degree of complexity, flow diverters and the surrounding vascular were considered as rigid boundaries in computational simulations [1997 Aenis, 1997; Ford, 2005 &2008; Hoi, 2006; Castro, 2006; Cebral, 2006 & 2008;, Chien, 2008; Rayz, 2008; Boussel 2009; Tsuei, 2009; Sforza 2010]. These investigations yielded useful information; however, more comprehensive reliable information can be obtained if boundary properties and motion can be modeled as well as the elasticity of the bioimplant. This is due to the fact that the phasic relationship between pressure and flow is dependent on the viscoelasticity of the vascular system and intra aneurismal flow properties can be markedly different between rigid and compliant boundaries. Fluid Structure Interaction (FSI) is a computational research field that bridges solid mechanics

with fluid mechanics. In principle, the fluid domain is considered and solved initially such that the load it exerts on the vascular wall and the bioimplant is resolved. The deformation of the solid due to the applied loads is then calculated. The new boundaries now can serve as input to the flow domain to recalculate the flow and its loads on the solid again. The process is repeated iteratively until balance and convergence is achieved.

The goal of this study is to develop an FSI model of the vascular replica of the elastase induced aneurysm in rabbit that was used in the PIV experiments [Seong 2007]. The results of the computational model can then be compared to the PIV data for validation purposes. While beyond the scope of this investigation, once a stable computational solver has been achieved we can depart from the experiments that have been performed and test new designs of flow diverting devices in order to optimize their efficacy in reducing intraaneurysmal flow. We can initially test the same structural design and investigate the influence of different design parameters such as porosity, filament diameter, vascular wall elasticity, and flow diverter radial flexibility. Later, we will be able to investigate different designs that are based on other manufacturing technologies such as laser cutting in which the windows generated by the design pattern are different than simple diamonds. Thereafter simulations can be commenced on specific geometries of patients' aneurysms that are obtained with any of the clinical available imaging modalities such as MRA, or Cone-Beam CT (3D angiography). We will be able to conduct the simulation of vascular intervention by virtual implantation of the devices in the computational model and predict a priori the

potential for success of the bioimplant in excluding a particular human aneurysm from the circulation. Therefore, the device can be optimized before the actual intervention takes place for the maximum benefit of the patient.

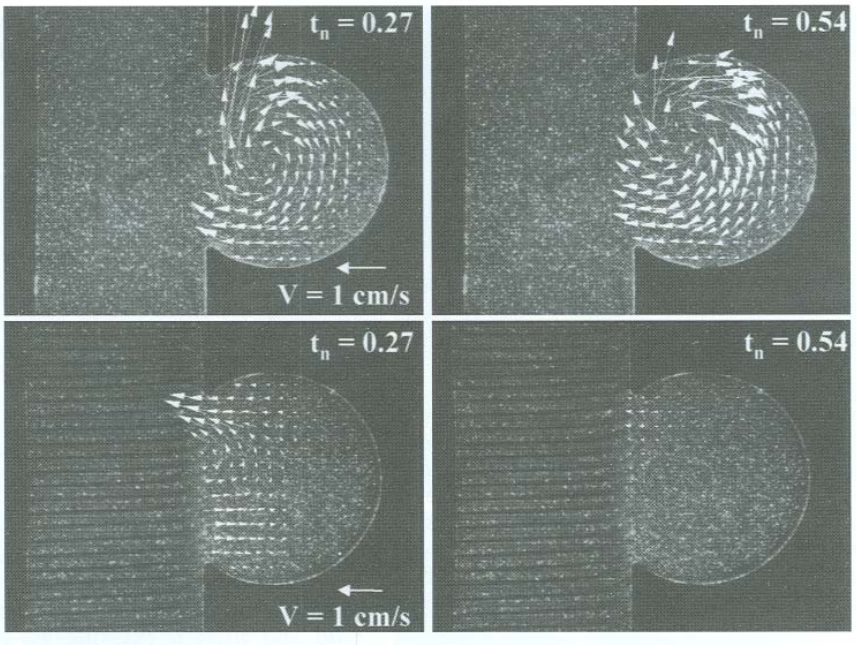

Figure 1-1. Velocity field inside the aneurysm for the nonstented case (top panels) and one of the stented cases, at two points in the cardiac cycle (bottom panels). The flow conditions in the parent artery are described by a Reynolds number of 175 and a Womrsley number of 2.54. t_n is the normalized time coordinate with respect to the duration of the cardiac cycle. Flow enters from the bottom of the picture (From [Lieber 2002]).

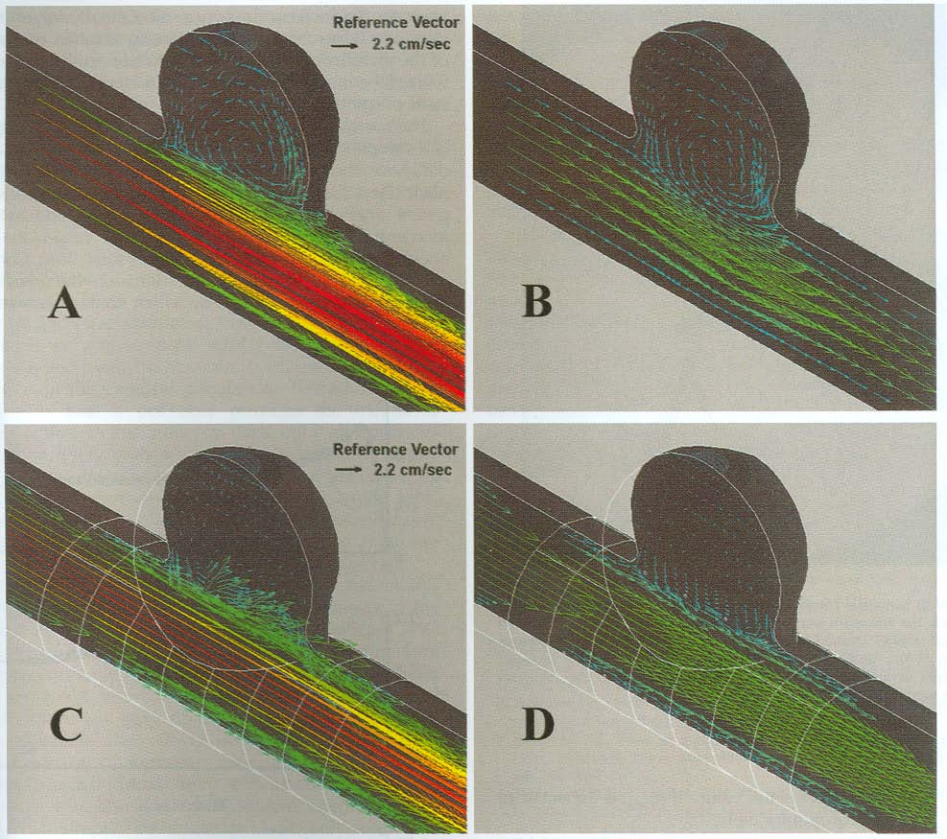

Figure 1-2. CFD simulation for a nonstented side wall aneurysm (top panels). Bottom panels show the stented case. Panels A and C are the velocity profile for the parent artery and the aneurysm at peak systole, whereas panels B and D at end diastole (From [Aenis, 1997]).

CHAPTER 2. NUMERICAL METHODS AND MODEL VALIDATIONS

In this chapter we discuss fluid and solid mechanics as applicable to the field of vascular mechanics and hemodynamics. Specific details about the elastase induced aneurysm model in rabbit is discussed in chapter 3.

2.1 The Governing Equations of Fluid Mechanics

The physical laws describing blood flow in arteries are the conservation of mass and the conservation of momentum. Temperature gradients (or heat transfer) are minimal, blood density does not change and flow is considered as incompressible. Therefore, conservation of energy is not required and will not be involved in this study.

2.1.1. The Conservation of Mass and Momentum

Conservation of mass applied to a fluid passing through an infinitesimal fixed control volume in a cartesian inertial coordinate system yields the equation of continuity:

$$\frac{\partial \rho}{\partial t} + \nabla \bullet \left(\rho V \right) = 0 \qquad (2.1)$$

Conservation of momentum is simply Newton's second law applied to a fluid passing through an infinitesimal control volume, which yields the Navier-Stokes equation:

$$\frac{\partial \rho \vec{V}}{\partial t} + \nabla \bullet \left(\rho \vec{V} \vec{V} - \vec{\tau} \right) = \vec{f} \tag{2.2}$$

And the non-conservative forms of continuity and Navier-Stokes equations:

$$\frac{\partial \rho}{\partial t} + \vec{V} \bullet \nabla \rho + \rho \nabla \bullet \vec{V} = 0 \tag{2.3}$$

$$\rho \frac{\partial \vec{V}}{\partial t} + \rho \vec{V} \bullet \nabla \vec{V} - \nabla \bullet \vec{\tau} = \vec{f} \tag{2.4}$$

where, t is the time, ρ is the density, $\vec{V}$ is the velocity vector, $\vec{f}$ is the body force vector of the fluid medium, $\vec{\tau}$ is the stress tensor. The above equations are based on the Eulerian approach for the description of the continuum motion: the characteristic properties of the medium are considered as functions of time and space in the frame of reference.

In solid mechanics, the Lagrangian scheme, in which each individual node of the computational mesh follows the associated material particle during motion, is widely used. In fluid mechanics, however, the Eulerian scheme is better suited. In the Euilerian scheme the computational mesh is fixed and the continuum moves with respect to the grid. When any part of the computational domain is deformable, the Eulerian description of fluid flow is no longer applicable and the Lagrangian description must be used. To meet this challenge and to combine the advantages of the above classical kinematic descriptions, while minimizing their respective drawbacks as far as possible, an Arbitrary-Lagrangian-Eulerian (ALE) formulation is a possible compromise. In the ALE

description, the nodes of the computational mesh may be moved with the continuum in the normal Lagrangian fashion, or be held fixed in the Eulerian manner, or, be moved in some arbitrarily specified way to give a continuous rezoning capability. Because of this freedom in moving the computational mesh offered by the ALE description, greater distortions of the continuum can be handled than would be allowed by a purely Lagrangian method, with more resolution than that afforded by a purely Eulerian approach. Obviously, the Navier-Stokes equations discussed so far need to be rewritten in the ALE system.

2.1.2 Arbitrary Lagrangian Eulerian (ALE) Method

Considering a transformation such that the new coordinate is the sum of the initial coordinate and its displacement:

$$x = \xi + d(\xi, \tau) \tag{2.5}$$

$$t = \tau \tag{2.6}$$

where the moving coordinate system (x, t) has been transformed into a new coordinate system (ξ, τ). The vector $\mathrm{d}(\xi, \tau)$ is used to deal with the arbitrarily moving coordinates. The time derivative of an arbitrary function, $f(x, t) = f\left(\xi + d(\xi, \tau), \tau\right)$, is

$$\frac{\partial f}{\partial \tau} = \frac{\partial f}{\partial t} + \frac{\partial x}{\partial \tau} \bullet \frac{\partial f}{\partial x} \tag{2.7}$$

Using $w \equiv \frac{\partial x}{\partial \tau} = \frac{\partial d}{\partial \tau}$ to represent the moving coordinate velocity, we have

$$\frac{\partial f}{\partial t} = \frac{\partial f}{\partial \tau} - \frac{\partial x}{\partial \tau} \bullet \frac{\partial f}{\partial x} = \frac{\partial f}{\partial \tau} - w \bullet \nabla f \tag{2.8}$$

When this equation is applied to time derivatives in the Navier-Stokes equations that are expressed in a purely Eulerian coordinate system, the differential forms of ALE equations are obtained. For example, in the ALE system, the nonconservative continuity equation becomes,

$$\frac{\partial \rho}{\partial \tau} + \left(\vec{V} - \vec{W}\right) \bullet \nabla \rho + \rho \nabla \bullet \vec{V} = 0 \tag{2.9}$$

Hence, the only difference between an ALE formulation and the Eulerian formulation is that the relative velocity replaces the convective velocity. Furthermore, the case of $\vec{W} = \vec{V}$ corresponds to a purely Eulerian description.

Applying the above equations to the Newtonian incompressible laminar flow, we get:

Continuity: $v_{i,j} = 0$

Momentum: $\rho\left(\frac{\partial v_i}{\partial t} + v_{i,j} v_j\right) = \tau_{ij,j} + f_i^B$

Constitutive relations: $\tau_{ij} = -p\delta_{ij} + 2\mu e_{ij}$

Here we have:

v_i =velocity of fluid in direction

ρ =mass density

τ_{ij} =components of stress tensor

f_i^B =components of body force vector

p =pressure

δ_{ij} =Kronecker delta

μ =fluid (laminar) viscosity

e_{ij} =components of velocity strain tensor = $\frac{1}{2}\left(v_{i,j} + v_{j,i}\right)$

In hemodynamics, Newtonian fluid is often used as constitutive model for blood properties despite then known shear thinning property of blood. Other constitutive models used are the Herschel-Bulkley model, the Bingham model, the Bird-Carreau model, the Cross model, the Power-Law model, the Casson model, and the Quemada model [1992 Chandran]. Blood is a non-Newtonian fluid which belongs to the shear thinning kind. At low shear rates, the apparent viscosity increases markedly, because the red blood cells tend to aggregate and form rouleaux, but at an increasing rate of shear, the aggregates gradually break up and after the rate of shear reaches about 50 sec^{-1}, the viscosity coefficient approaches an asymptotic value of 3.5 cP. On the other hand, in small tubes the apparent viscosity at higher rates of shear is smaller than it is in larger tubes. This progressive diminution with tube size begins to be detectable with tubes of less than 1mm internal diameter. However, for blood flow in major arteries, the approximation of Newtonian flow is feasible and makes the problem much easier to manage [1990 MaDonald].

2.2 Solid mechanics

The following are the basic aspects of solid mechanics applicable to the simulations here:

Engineering strain, is defined as: $e_0 = \frac{l - l_0}{l_0}$

Stretch is defined as: $\lambda = \frac{l}{l_0}$

Small strains are strains of less than about 2%.

Engineering stress, is defined as: $\sigma = \frac{F}{A_0}$

Cauchy stress, or the true stress, is defined as:

$$\tau = \frac{F}{A} = \frac{\sigma A_0}{A}$$

The simplest vascular model is the linear elastic material model, where the strain and stress satisfy:

$${}^t_0\sigma = C \bullet {}^t_0e$$

Where ${}^t_0\sigma$ is engineering stress, ${}^t_0e$ is engineering strain, and C is a matrix related to the material constitutive relation. In elastic isotropic material, the components of matrix C are the Young's modulus, E, and the Poisson's ratio, ν.

In biomechanics the Mooney-Rivlin model is used more often to describe soft arterial tissue than elastic model. The simplified Mooney-Rivlin material model that is commonly used in biomaterials modeling is based on the following expression:

$$W = C_1\left(I_1 - 3\right) + C_2\left(I_2 - 3\right) + D_1\left[e^{D_2\left(I_1 - 3\right)} - 1\right] \qquad (2.10)$$

Where I_1 and I_2 are the first and second strain invariants. C_1, C_2, D_1 and D_2 are material constants. This model is commonly chosen because it provides very good fit to experimental data. It is also available in the software package ADINA [2006 Bathe].

In application of computational biomechanical models to arteries, the following assumptions are usually made:

(1) The wall is considered to be a continuum. Assuming the artery wall is a continuum implies that an infinitesimal volume may be considered to be a material particle in the neighborhood of which there is always more material present. With this assumption, we may consider a quantity, such as mechanical stress, to be defined at a point in the medium.

(2) The wall is considered to be homogeneous. Homogeneous material is a material whose properties, at any given load, are not function of position within the body. With this assumption, no distinction can be made among the elastic contributions by each component of the tissue. However, by studying the orientation and shapes of the components of the artery wall, we may conclude that some dictate the global material properties of the tissue in certain direction, while other components are predominant in the other directions. The hypothesis of homogeneity therefore implies that the components are arranged such that the global elastic properties do not vary with position. This is not to be confused with the material symmetry or isotropy.

(3) Isotropy. A material is said to be isotropic when the material properties are invariant under rotations. In reality, the inspection of the microstructure of cardiovascular tissue demonstrates that the material is anisotropic. The concentric elastic lamellae of the

blood vessels would seem to indicate a circumferential symmetry of the tissue. Thus, an orthotropic model would be a more appropriate assumption (Chuong, 1986). But in many studies, the material is assumed to be isotropic.

(4) Incompressibility. All real materials are compressible to some degree. In the case of vascular tissue, incompressibility is well accepted. The experiments by Carew, et al. (1968) are often quoted as justification for this assumption. Carew et al. immersed arterial segments in water enclosed in a cylinder and showed that the total volume of the tissue and water in the cylinder did not change with increasing of the pressure and longitudinal stretch. This indicates that arterial tissue is almost incompressible.

(5) Material nonlinearity. The stress-strain relationship of cardiovascular tissue is nonlinear due to the composite nature of tissue components. The arterial wall is composed of three concentric layers. The inner most layer, the intima consists of a monolayer of endothelial cells (endothelium) providing a smooth surface in contact with blood and playing a role of a mechanosensor to wall shear stress. The middle layer, the media is a thick layer containing smooth muscle cells and elastic fibers (elastin) intermingled and arranged in a helical fashion. The adventia is the outer layer and is composed of fibrous collagenous tissue. Collagen, elastin and ground substances together behave as a composite with a nonlinear response. Separately, each component has unique mechanical properties. [Humphrey, 1995; Zhao, 1998]

Simpler models of the arterial wall are also used in computational models of the biomechanics of arteries. The use of a linearly elastic model is supported by measurements which show that in the physiological pressure range the wall motion is limited and thus in that narrow range the complex viscoelastic modulus can be

approximated as incrementally linear [Milnor, 1989]. This is due to the fact that in the physiological range collagen offers little stress support and most of the stress is supported by the smooth muscle, connective tissue, and elastin that is considered virtually a linearly elastic material [Fung 1993]. Furthermore, in this investigation we simulate an in virto experiment which was conducted in a silicone vascular replica that has liner elastic properties so further validation simulations and analysis will be conducted with a linear elastic material of elasticity equivalent to the one used in the experiments.

2.3 Boundary and Initial Conditions

2.3.1. Initial Condition

It is obvious that the closer the initial guess for the pressure and velocity field is, the faster and easier the program converges. Although initial conditions are not required in steady-state analyses, they are used as a "guessed" solution at the start of the equilibrium iterations. A good initial condition, may not only accelerate the convergence during equilibrium iterations, but also be a key factor in obtaining solutions in certain cases.

2.3.2 Boundary Condition

The usual boundary conditions used in Adina included prescribed velocity, and prescribed pressure. For FSI simulation, we will have FSI boundaries in addition of non-

slip wall condition. The boundary of the fluid domain is divided into the following regions for the assignment of boundary conditions: inlet, outlet, and the fluid-structure interaction interface, in some case, a non-slip wall condition. The applied boundary conditions on the non-FSI regions are (i) a time dependent fully developed velocity profile on inlet and (ii) a time dependent normal traction (due to luminal pressure) on outlet.

2.4 Model Validation

The straight circular pipe flow was chosen for the validation of the fluid-structure interaction CFD validation. The fluid is modeled as laminar Newtonian flow, with density of 1153 kg/m^3, viscosity as 4.0 cP; the material parameters of the vascular wall are listed as following: For elastic model, Elasticity as 1.2 MPa, and Poisson ratio as 0.49. The internal diameter is 10mm, while the thickness is 1mm.

2.4.1. Poiseuille Flow

For pipe flow, the Navier-Stokes equations can be simplified to the Hagen-Poiseuille equations with a velocity distribution profile shown in Eq. 2.11.

$$u_s = \frac{dp}{ds} \bullet \frac{1}{4\mu} \bullet \left(r^2 - a^2\right) \tag{2.11}$$

The flow rate is given by:

$$Q = \int_0^a u_s 2\pi r dr = -\frac{dp}{dx} \bullet \frac{1}{8\mu} \bullet \pi a^4 \tag{2.12}$$

The shear stress at the inner cylindrical surface of the tube wall and which acts in the axial direction is given by:

$$\tau_s = -\tau_{rx}(a) = -\mu \left(\frac{du_s}{dr} \right)\Bigg|_{r=a} = -\frac{dp}{dx} \bullet \frac{a}{2} = \frac{4\mu Q}{\pi a^3} \tag{2.13}$$

The sign difference between τ_s and τ_{rx} is that τ_s is taken to represent the shear stress exerted by the fluid on the tube wall.

For flow simulation in a rigid tube, the wall is treated as a non-slip boundary. The solution was repeated using three sets of meshes with 5*16*24, 5*16*48, 5*32*48 elements (where the product r*s*z, represents the number of elements in the radial direction r, times the number of elements in the azimuthal direction, s, times the number of elements in the axial direction, z), to check mesh independence of the solution by running the ADINA-F program. A comparison between the numerical result and the analytical solution is shown in Fig 2-1. The error between analytical solution of Poiseuille flow and numerical solution of velocity is about 2.53%, 2.50%, and 0.64% for the three meshes, respectively. Even for the coarsest mesh, the results are in good agreement with the theoretical values.

2.4.2. Womersley flow in a rigid tube

Flow in a tube in which the driving pressure varies in time is governed by:

$$\rho\frac{\partial u}{\partial t}+\frac{1}{\rho}\frac{\partial p}{\partial x}=\mu\left(\frac{\partial^2 u}{\partial r^2}+\frac{1}{r}\frac{\partial u}{\partial r}\right) \tag{2.14}$$

A pulsatile pressure gradient can be decomposed into a Fourier series and for simplicity the time varying pressure gradient of one harmonic only can be considered. Assuming linearity and superposition holds, the complete solution can be obtain by summation of the solutions of all harmonics

$$\frac{\partial p}{\partial x}=M\cos(\omega t) \tag{2.15}$$

Using the Bessel equation, the velocity profile can be solved as:

$$u=\frac{AR^2}{\mu i\alpha^2}[1-\frac{J_0(\alpha y i^{3/2})}{J_0(\alpha i^{3/2})}]e^{i\omega t} \tag{2.16}$$

Here, R is the radius of the tube; α the Womersley number; μ the fluid viscosity; J_0 the zero order Bessel function, $y=r/R$, the radius ratio.

A comparison between the analytical solution and the ADINA numerical simulation is shown in Fig 2-2. The error is about 3.1%.

2.4.3. Womersley flow in an elastic tube

The linear wave propagation equation for viscous blood flow in a longitudinally tethered elastic vessel is given by the Moens-Korteweg formula:

$$c = \sqrt{\frac{Eh}{2\rho R_i}} \tag{2.17}$$

Where E, Young's Modulus, R_i is the internal radius of the tube, ρ is the density of the vessel, and h is the thickness of the artery wall. The theoretical value of the wave speed, c, is about 10.3407 m/s, while the computational value is 10.64 m/s, corresponding to an error of about 2.9%.

The axial velocity distribution according to Womesley's theory [Zamir 2005] is:

$$u(x,y,t) = \frac{AR^2}{\mu \quad i\alpha^2}[1 - \frac{J_0(\alpha y i^{3/2})}{J_0(\alpha i^{3/2})}]e^{i\omega(t-x/c)} \tag{2.18}$$

Where $y = \frac{r}{R_i}$.

A comparison between the numerical simulation and the analytical solution is shown in Fig 2-3. The maximum error between the two solutions for flow in the elastic tube is about 3.3%.

The radial velocity of the fluid on the inner wall of the tube, and hence the radial velocity of the tube is [Zamir 2005]:

$$v(x,R,t) = u_s \frac{2R\omega}{i\Lambda^2 c}[1 - G \bullet g]e^{i\varpi(t-x/c)} \tag{2.19}$$

Here, $\Lambda = \left(\frac{i-1}{\sqrt{2}}\right) \bullet \alpha$

$\alpha = R\sqrt{\frac{\rho\omega}{\mu}}$, the Womersley number;

$G = \frac{2 + z(2\sigma - 1)}{z(2\sigma - g)}$, and $g = \frac{2J_1(\Lambda)}{\Lambda J_0(\Lambda)}$

$u_s = -\frac{k_s R^2}{4\mu}$ is the maximum velocity of the steady flow, $k_s = \frac{dp_s}{dx}$ is the pressure gradient σ is the poisson ratio of the tube material.,

Since the wave speed, *c*, appear in the formula for the radial velocity both in the time dependent exponent (as in the axial velocity) and in denominator of the velocity magnitude we can no longer use the lineraized form of the of the wave propagation velocity (Eq 2.17), which will result in a large error. A more accurate expression for the wave propagation velocity has been derived by Womersley for the feely moving elastic tube that needs to be used here [Lieber & Sadasivan 2006]

$$\frac{c}{c_0} = \sqrt{2(1-\Phi)}1 + \left[k/2 - \Phi\mathrm{T} \pm \sqrt{\{1 + k/2 - \Phi\mathrm{T}\}^2 + (1-\sigma^2)(\Phi^2 - (1-2k)\Phi - 2k)} \right]^{-\frac{1}{2}} \tag{2.20}$$

Here, $\Phi = \frac{2J_1(\alpha i^{3/2})}{\alpha i^{3/2} J_0(\alpha i^{3/2})}$,

$T = k/2 + \sigma - 1/4$,

$k = \frac{h\rho}{R\rho_0}$,

To compare the numerical simulations with the theoretical derivation we compare the radial velocity of a point in the inner surface of the tube in the middle of the tube axis. The results are shown in Fig 2-4. The radial velocity at this location from the simulation

appears to be in agreement with the theoretical solution both in magnitude and phase. However, the amplitude of numerical simulation is about 9% smaller the amplitude of the analytical solution, and there is 1.3 degrees lag. These differences, however, can be attributed to the fact that in the derivation of the theoretical solution a thin tube wall was assumed, which is not the case in the simulation where the wall thickness is 20% of the inner radius.

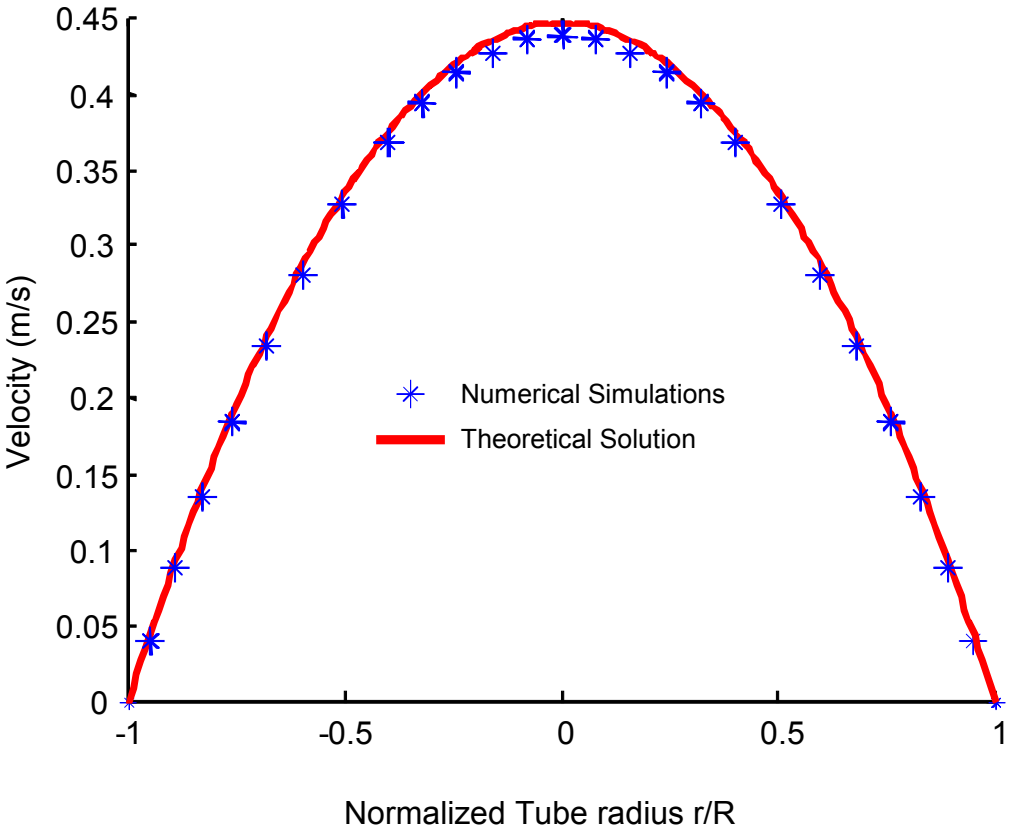

Figure 2-1 Comparison between the analytical and numerical solutions for steady (Poisuille) flow in a rigid tube

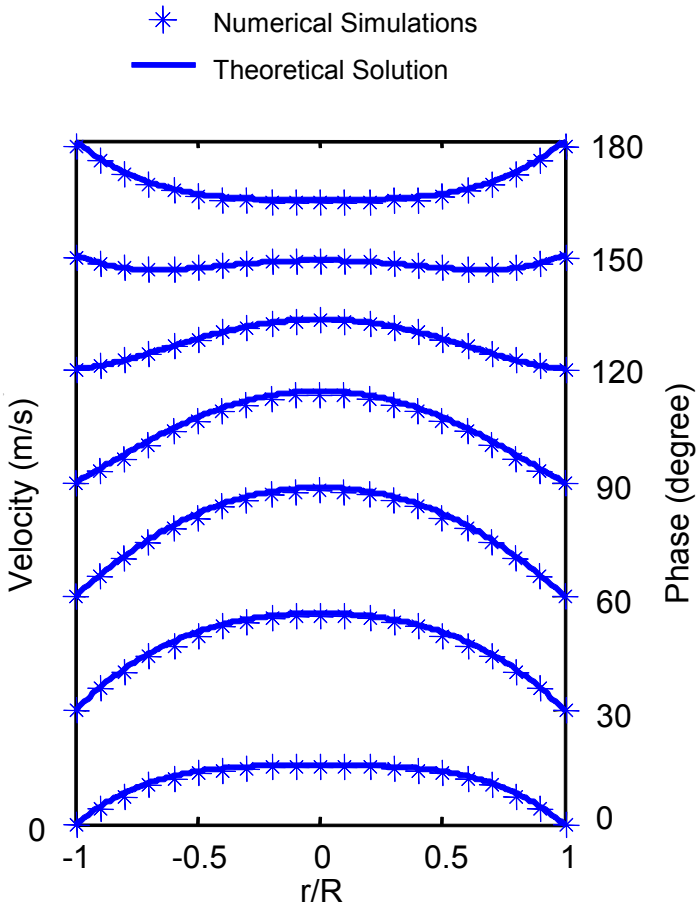

Figure 2-2 Comparison between the analytical and numerical solution for pulsatile (Womersley flow) velocity profiles in rigid tube.

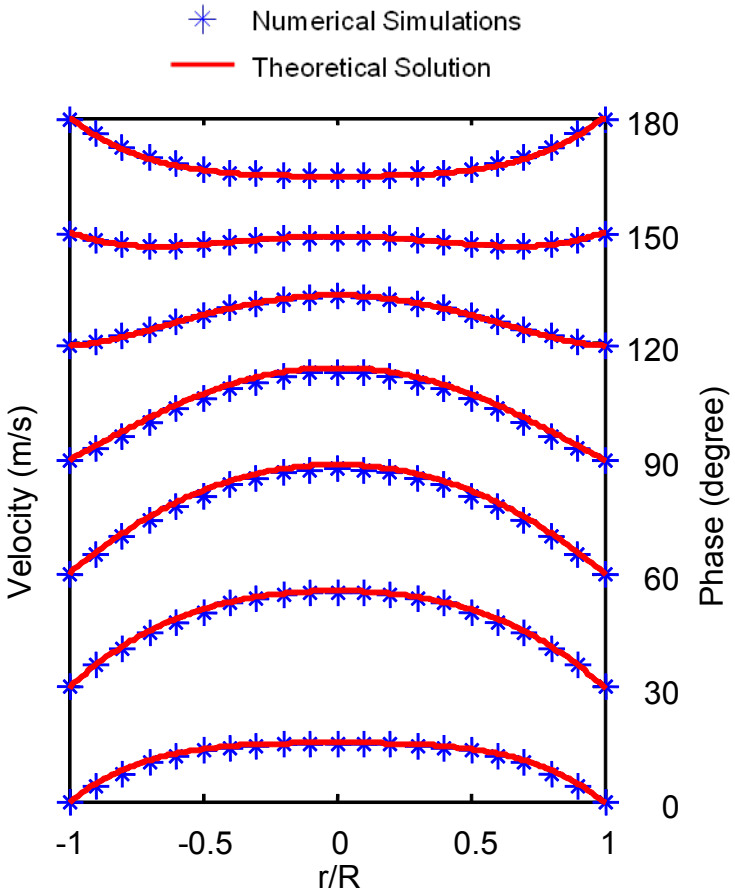

Figure 2-3 Comparison between the analytical and numerical solution for pulsatile (Womersley flow) axial velocity profiles in an elastic tube

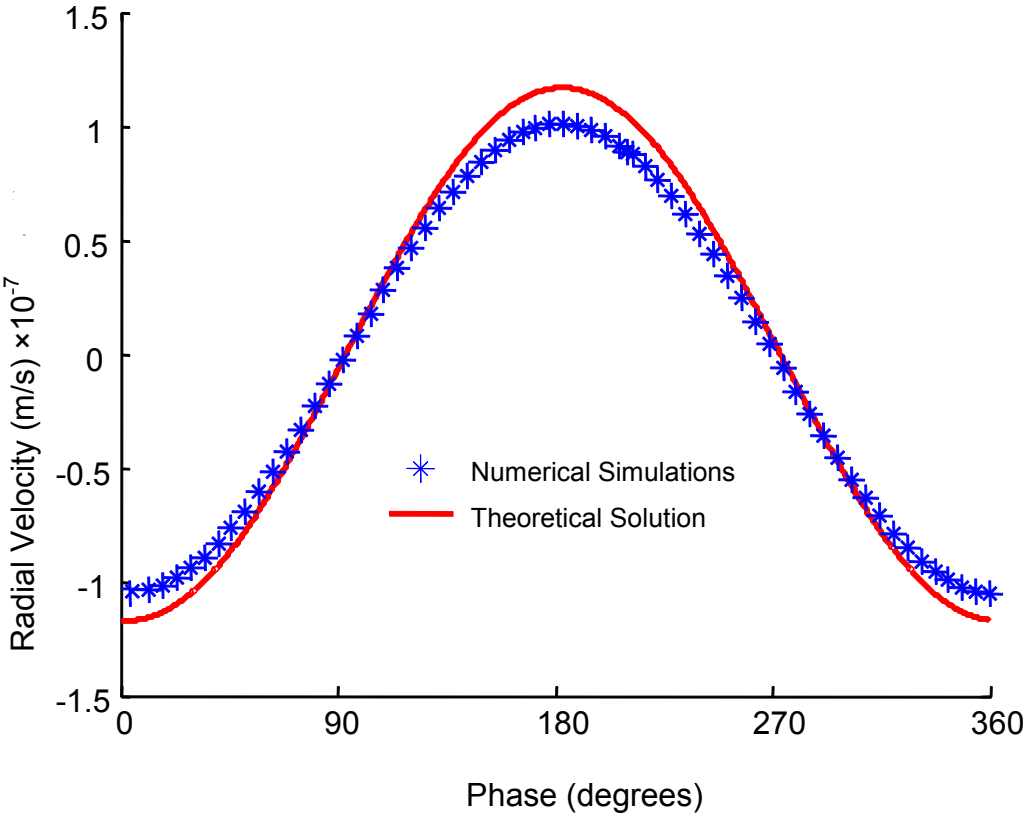

Figure 2-4. Radial velocity profile for a point on the inner wall of the tube and axially located in the center of the tube during one pulsatile cycle

CHAPTER 3. ANEURYSM FSI MODEL AND RESULTS

3.1 The Silicone Replica 3-D Model

The silicone model of the elastase induced aneurysm model in rabbit that was used in the experiments was originally constructed using Pro/Engineer 2001 (PTC, Needham, MA) [Seong 2005 & 2007]. This geometry was used as the lumen of the computational model or the geometry for the fluid section. The solid wall of the model extends about 0.6 mm beyond the fluid domain and is of uniform thickness. To construct the wall in the computational domain, the fluid model was first reconstructed in SolidWorks 2005 (Dassault SolidWorks Corp., Concord, MA) by using the same geometrical parameters. A 0.6mm thick layer on the model can be built by utilizing the outward shell function in SolidWorks. The fluid part and solid part of the aneurysm model that was constructed in SolidWorks are shown in Figure 3-1 and 3-2. Both geometries of the solid part and fluid part are read into ADINA 8.5 (ADINA R&D, Inc., Watertown, MA) through the module ADINA-M. In the model, we selected the free-form 10-node solid element for the solid part, and Flow-Condition-Based Interaction (FCBI) 3-D free-form 4-node fluid element for fluid part. Meshing of the model is done in ADINA. For the coarsest mesh a global size of 0.001mm for fluid part and 0.0015mm for the solid part were selected with the exception of the aneurysm sac that is meshed using 0.0005 mm size mesh, as shown in Figure 3-3. Finer meshes for the whole model were used as well and the simulations results were compared to ensure that the solutions are mesh independent. The different resolution meshes are listed in Table 3-1. Mesh independent

solutions (Figure 3-5) were obtained for mesh set 3, whose aneurysm sac mesh is shown in Figure 3-4.

3.2. Governing Equations and Boundary Conditions

The fluid is assumed to be homogeneous, incompressible and Newtonian. Flow is assumed to be laminar, and the mass and momentum conservation laws implemented with the continuity and the Navier-Stokes equations are adopted in an Arbitrary Lagrangian-Eulerian (ALE) formulation. The ALE formulation introduces a moving coordinate system to model the deformation of the fluid domain. In ALE form the continuity and Navier-Stokes equations are given by:

$$\frac{\partial \rho_f}{\partial t} + \rho_f \nabla \bullet \vec{v} = 0 \tag{3.1a}$$

$$\rho_f \frac{\partial \vec{v}}{\partial t} + \rho_f \left(\left(\vec{v} - \dot{\vec{d}}_f \right) \bullet \nabla \right) \vec{v} = \nabla \bullet \tau_f + \vec{f}_f^B \tag{3.1b}$$

Where ρ_f is the fluid density, $\vec{v}$ is the fluid velocity vector, $\dot{\vec{d}}_f$ is the moving coordinate velocity, τ_f is the fluid stress tensor, $\vec{f}_f^B$ are the body forces per unit volume, respectively. In the model, fluid density is taken as ρ = 1153 kg/m3 and the dynamic viscosity is μ = 0.004 Pa s.

The structural domain is described by using a Lagrangian formulation. The governing equilibrium equations are:

$$\nabla \bullet \tau_s + f_s^B = \rho_s \frac{\partial^2 u_s}{\partial t^2} \tag{3.2}$$

Where τ_s is the Cauchy stress stressor tensor, f_s^B are body forces per unit volume, ρ_s is the solid density, u_s are the unknown displacements, respectively. The stresses are evaluated using the relevant constitutive relations [Bathe 2007].

Coupling of the fluid and structural response can be achieved numerically in the conditions of displacement compatibility and traction equilibrium along the structure–fluid interfaces.

Displacement compatibility:

$$d_f = d_s \tag{3.3}$$

And traction equilibrium:

$$f_f = f_s \tag{3.4}$$

Where d_f and d_s are the displacements, f_f and f_s are the tractions of the fluid and solid, respectively [Bathe, 2004]. The wall is assumed to be isotropic, linear, elastic and incompressible [Carew, 1968] with a Young's Modulus E = 0.82 MPa [Scotti, 2009] and a Poisson's ratio υ = 0.49, and the wall is assumed to undergo large displacements and small strains.

The boundary of the fluid domain is divided into inlet, outlet, and the fluid-structure-interaction interface, as shown in Figure 3-1. The inlet boundary condition is a time dependent plug velocity profile and the outlet boundary condition is a time

dependent outlet pressure. The wave forms of flow rate and pressure are shown in Figure 3-6. In order to achieve faster convergence in the time dependent simulations of the FSI computations, a quasi steady–state simulation was first conducted during which the whole model was pressurized to typical mean arterial pressure. The results of these initial simulations can then be used as initial condition for the transient simulations. In this way the steady-state fluid flow results provide a better initial guess for transient simulations. The simulations are carried for a time period longer than three pulsatile cycles with a time step duration of $\Delta t = 0.0025$ seconds until the results are stable.

The flow through the elastic model is solved using ADINA-FSI. The procedure of the solution method can be described as follows. Starting from an initial fluid domain, the Navier-Stokes equations (3.1b) are solved first. Then the equilibrium equations (3.2) are solved with input from the flow field to determine the wall displacement. Thereafter, the Navier-Stokes equations are solved again over the newly adjusted domain. This process is repeated until desired accuracy is reached. The stopping criterion is:

$$\left\| f^i - f^{i-1} \right\| / \left\| f^i \right\| \le TOL \tag{3.5}$$

where f can be velocities or displacement; i signifies the i^{th} interation, TOL is the selected convergence tolerance criterion, in this case a value of 0.001 was selected.

It is known that convergence is difficult to achieve when the wall is significantly compliant [Bathe 2004 & 2007]. ADINA uses an automatic incremental iterative technique to reach convergence when the regular iterative procedure fails. At a given iteration step, when convergence from the fluid part is reached, ADINA takes the

changes of the pressure and stress fields of the fluid part as input and tries to determine the corresponding changes of the wall displacement. If convergence for the wall part cannot be obtained, ADINA reduces the size of the input by half and tries to determine the wall displacement in two increments. This is repeated until convergence or a default reduction limit is reached.

For the solid domain, the translational degrees of freedom in X-, Y- and Z-direction were not constrained, while rotational degrees of freedom around the X-, Y-, Z-axes were set to zero in the whole solid model due to symmetry. The FSI boundaries common to the fluid and solid must be identical. In addition boundary conditions have to be specified at non-common boundaries. In the fluid domain, velocity or flow rate is specified while at the outlets the luminal outlet pressure is specified. In the solid domain, the inlet and outlet faces are all set to be fixed, or translation in X-, Y- or Z-directions of the faces is set to zero. The flow dynamics similarity parameters of Reynolds and Womersley numbers, which are customary in pulsatile arterial flows, were set to be 908.9, and 6.79 in the simulations, respectively. In the PIV experiments the Reynolds and Womersley numbers were 971 and 9.38, respectively [Seong, 2007].

3.3. Results

3.3.1 The pressure gradient and the flow rate wave

The input data on the open boundaries include the inlet flow velocity, and the outlet pressures. From the computed results, we can calculate the inlet pressure. This way we can get the pressure gradient between the inlet and outlet boundaries of the computational flow domain. Also, from the known velocity distributions at the outlets the

flow rates through each outlet can be calculated. In the companion PIV experiments, the flow rate in the descending aorta, was about 60% of inflow through the ascending aorta, the rest of the inflow (40%) went through the other four smaller branches, namely, the right vertebral artery, the right subclavian artery, the left common carotid artery, and the left subclavian artery. To achieve similar flow distribution in the computational simulations, the pressure applied to the four smaller branches was 0.6 mmHg less than the pressure applied to the descending aorta. The computational results show that 58% of flow rate exited the model through the descending aorta. The flow rates in each of the smaller branches are shown in Figure 3-7. In PIV experiments [Seong 2005 & 2007, Asher 2010], the vertebral artery branch flow rate was recorded as 0.62 ml/s and 0.41 ml/s, respectively, as peak flow, while the numerical result shows it is 0.58 ml/s as peak flow, the peak flow rate in ascending aorta (inlet boundary) were both set as 25 ml/s in experiment and numerical model .

3.3.2. The velocity fields

The velocity in parent artery is much higher than that in the aneurysm sac as shown in Figure 3-8. The following figures depict only the velocity inside the aneurysm in the plane of symmetry of the aneurysm sac. During the acceleration phase of systole the flow rushes into the aneurysm sac from the proximal neck and exits through the distal neck in a counterclockwise fashion.(see Figure 3-9 to 3-11) It is only at about peak systole and during the deceleration phase of systole, that flow begins to rotate clockwise at the base of the aneurysm and a vortex is established with its center moving further up into the aneurysm (see Figure 3-12 to 3-15). During the small diastolic peak, a counter-

clockwise rotating vortex develops at the distal end of aneurysm (see Figure 3-16 to 18), this vortex quickly disappeared as a clock-wise rotation developed near the proximal end of the aneurysm and this clockwise rotation inside the aneurysm continues well into the late diastolic period. From late diastole to early systole, flow keeps a low amplitude clockwise rotation inside the aneurysm sac.

Peak flow rate through the vertebral artery was measured as 0.62 ml/s [Seong, 2007] and 0.41 ml/s [Trager, 2010]. In the numerical simulations peak flow is 0.58 ml/s. Since peak flow rate in ascending aorta was set to 25 ml/s both in the experiments and the simulations, flow through the vertebral artery is similar to the results obtained by Seong's study [Seong, 2007].

3.3.3. The vorticity inside the aneurysm

The vorticity is defined as:

$$\vec{\zeta} = \left(\frac{\partial w}{\partial y} - \frac{\partial v}{\partial z}\right) \bullet \vec{i} + \left(\frac{\partial u}{\partial z} - \frac{\partial w}{\partial x}\right) \bullet \vec{j} + \left(\frac{\partial v}{\partial x} - \frac{\partial u}{\partial y}\right) \bullet \vec{k} \tag{3.6}$$

Vorticity in the plane of symmetry simplifies to the last term in equation 3.6.

$$\vec{\zeta} = \left(\frac{\partial v}{\partial x} - \frac{\partial u}{\partial y}\right) \bullet \vec{k} \tag{3.7}$$

Figure 3-24 to 3-42 show vorticity coutours in the plane of symmetry inside the aneurysm sac. During most of diastole , the vorticity magnitude is almost zero, but during systole the vorticity changes rapidly. Rapid positive vorticity intensification starts at the proximal

and distal neck area, which means that clockwise vortex formation increases first in these two areas. Later during systole, negative vorticity appears near the distal neck where a counterclockwise vortex is formed.

To evaluate the vorticity over one pulsatile cycle, circulation inside the aneurysm was adopted:

$$\Gamma = \iint_A \vec{\zeta} \bullet \vec{n}\, dA \tag{3.8}$$

Here, $\vec{\zeta}$ is the vorticity, A is the normal plane area. Circulation has the similar mathematical expression as volume flow rate. We integrate the vorticity component over the symmetrical plane of the aneurysm sac in one cycle to get the instantaneous hydrodynamic circulation (Figure 3-43).

Comparing with the experiment results [Seong, 2007], the computational result of circulation is much smaller than experiments. One reason is that the flow rate wave is different and time period is different, but the real reason might be that in the experiment, every PIV frame shows 3-D particles' velocity, and these particles are not necessarily in the symmetrical plane, so the circulation in the experiments might include circulation values from multiple planes. One of the similarities is that in most time within one cycle the circulation is negative, which agrees with the fact that the flow pattern inside the aneurysm is clock-wise; during the small diastolic peak, the circulation is positive and this agrees with the anti-clockwise flow pattern.

3.3.4. The kinetic energy inside the aneurysm

Calculation of the kinetic energy in the aneurysm sac was obtained by sum of squares of the magnitudes of the velocity vectors inside the aneurysm for each time point in the pulsatile cycle. Thus, a time dependent measure of the kinetic energy inside the aneurysm throughout the cycle can be obtained. The results, shown in Figure 3-44 and 3-45, demonstrate that there are three energy peaks in the aneurysm in one cycle. The shape of the intraaneurysmal energy profile is in agreement with the experimental data (See Figure 3-45 (c), compare with 3-45(a)), however the level of the kinetic energy between the simulation and the experiments is different due to the differing hemodynamics. The first peak occurs during systole period, while second and the largest peak occurs during the transition from late systole to early diastole. This period in the pulsatile cycle is marked by an adverse pressure gradient in the parent vessel and flow instability that imparts the largest flow activity inside the aneurysm. The third smallest peak occurs in diastolic part of the cycle. To compare with the experimental result, we divided the kinetic energy by node number; in the 3-D aneurysm, the kinetic energy per point is about 0.0002 (m^2/s^2) (Figure 3-44 (b)), while in the symmetrical plane, the kinetic energy per point is about 0.00024 (m^2/s^2). (Figure 3-45 (b))

3.3.5. The shear stress

There is evidence that wall shear stress is related to thrombus [Ku, 1985]. For this reason we evaluated wall shear stress variation in one cycle inside the aneurysm sac at

proximal neck, dome and distal neck, as shown in Figure 3-46. Maximal wall shear stress near proximal neck is about 0.35 Pa; maximal wall shear stress near the distal neck is about 0.2 Pa; while the dome area's maximal wall shear stress around 0.0065 Pa. The dome area is always the area with lowest shear stress. In a straight segment of the parent artery wall shear stress varied between 0.01 to 0.1 Pa. In the PIV experiment, the ratio of wall shear rate on proximal neck to distal neck is about 1.5 to 2. Similarly in numerical result, wall shear stress ratio on proximal neck to distal neck is about 1.75. The proximal neck experiences the higher maximum shear stress than distal neck.

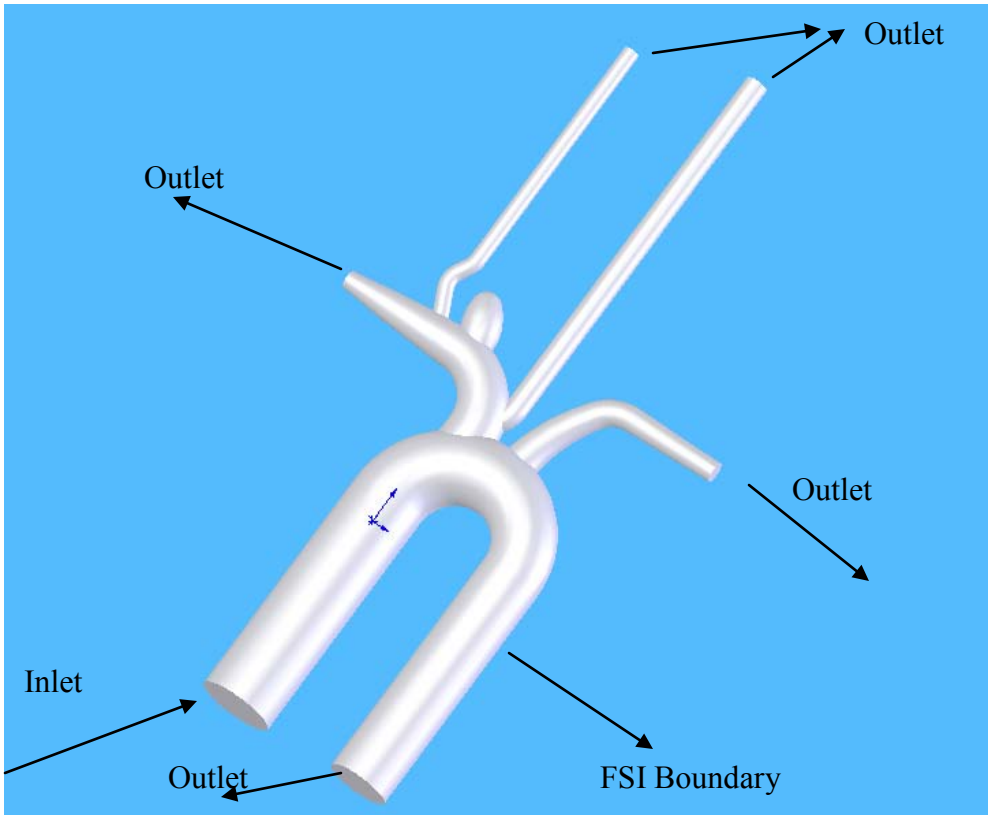

(a)

Figure 3-1. The fluid part of the aneurysm model constructed in SolidWorks.

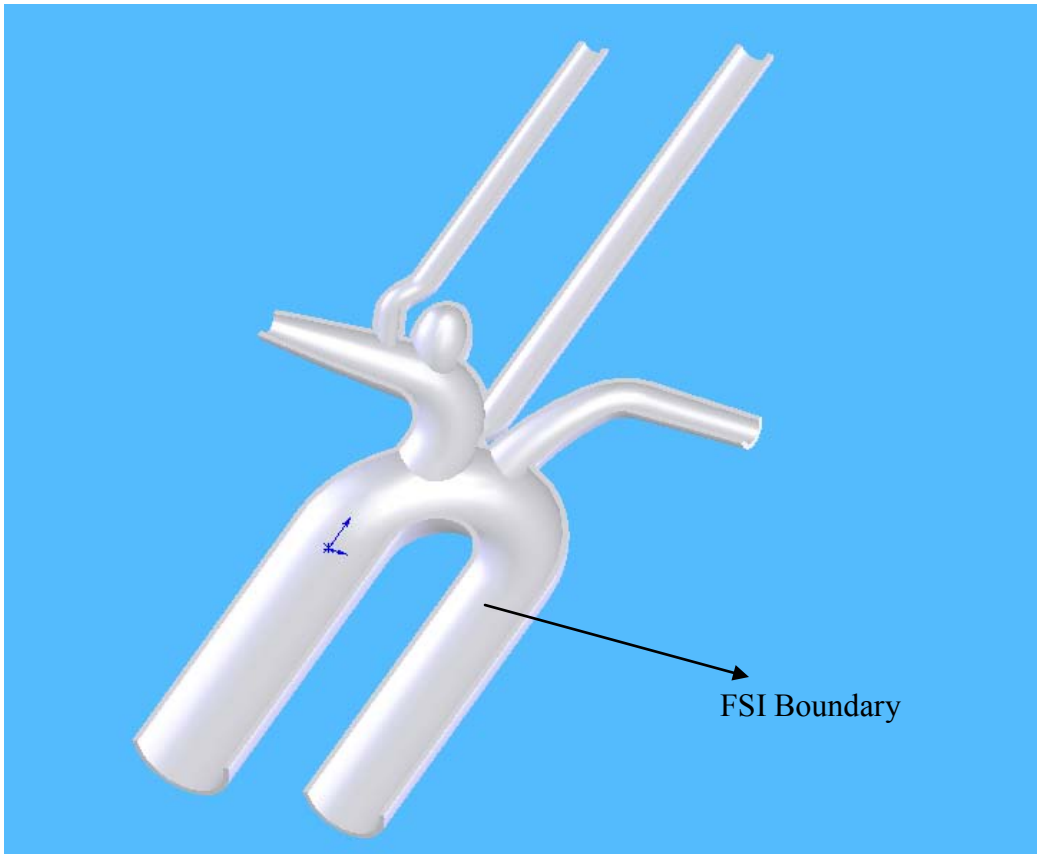

(b)

Figure 3-2. The solid part of the aneurysm model constructed in SolidWorks.

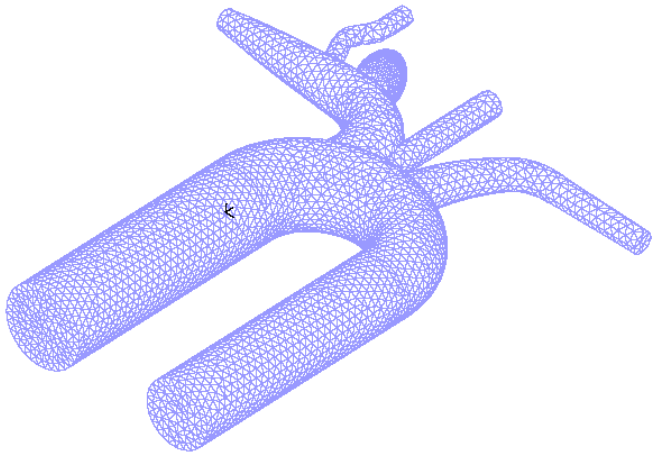

(a)

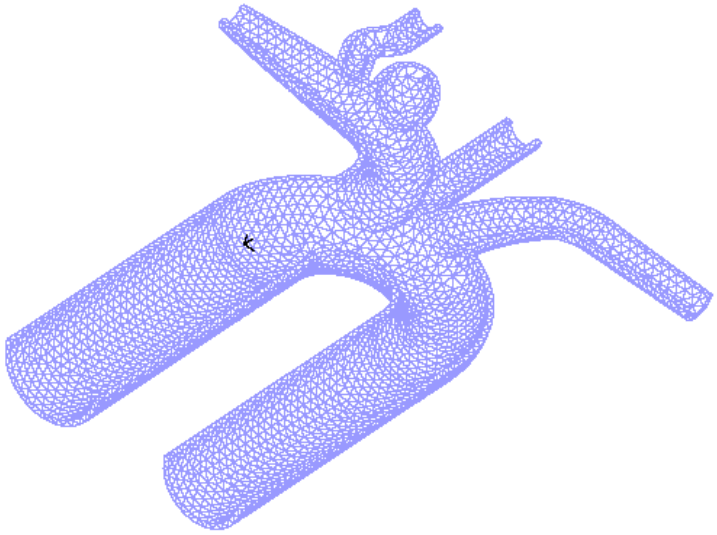

(b)

Figure 3-3. The coarsest meshes for the fluid part (a), and solid part (b) (half is shown).

Table 3-1. Meshes of various density used for the aneurysm model.

	Mesh Set 1	Mesh Set 2	Mesh Set 3	Mesh Set 4
Aneurysm sac mesh size (m)	0.0005	0.0005	0.0004	0.0003
The remaining part mesh size (m)	0.001	0.009	0.0008	0.00075
Aneurysm sac elements number	6595	6595	13402	27640
The remaining part elements number	46016	56356	80756	104425
Total elements number	52611	62951	94159	132065

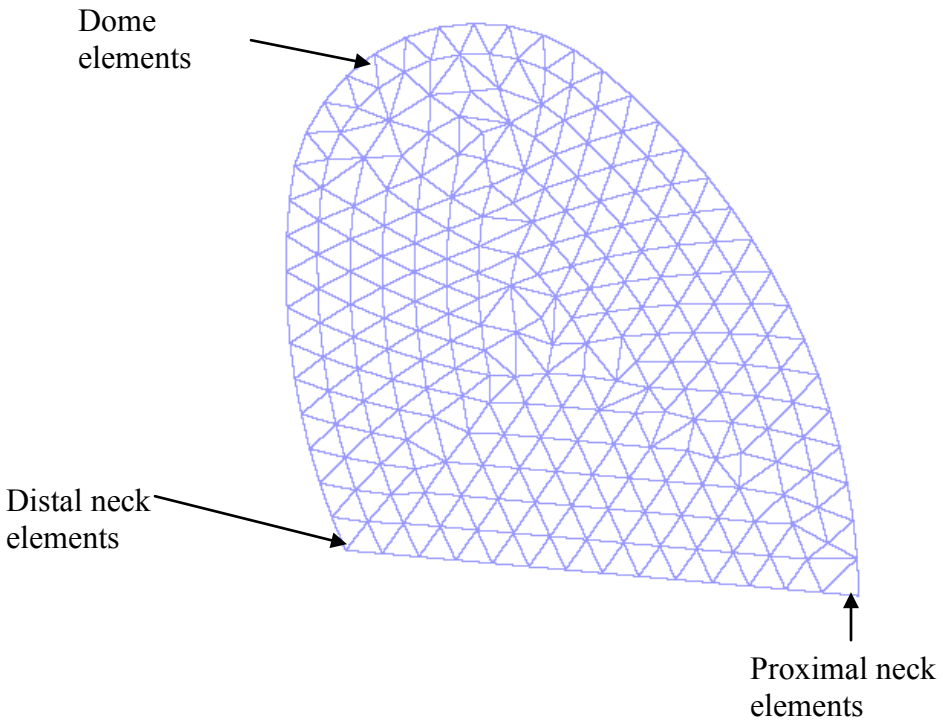

Figure 3-4. The aneurysm sac mesh in Mesh Set # 3, and the location of dome element, proximal element and distal element

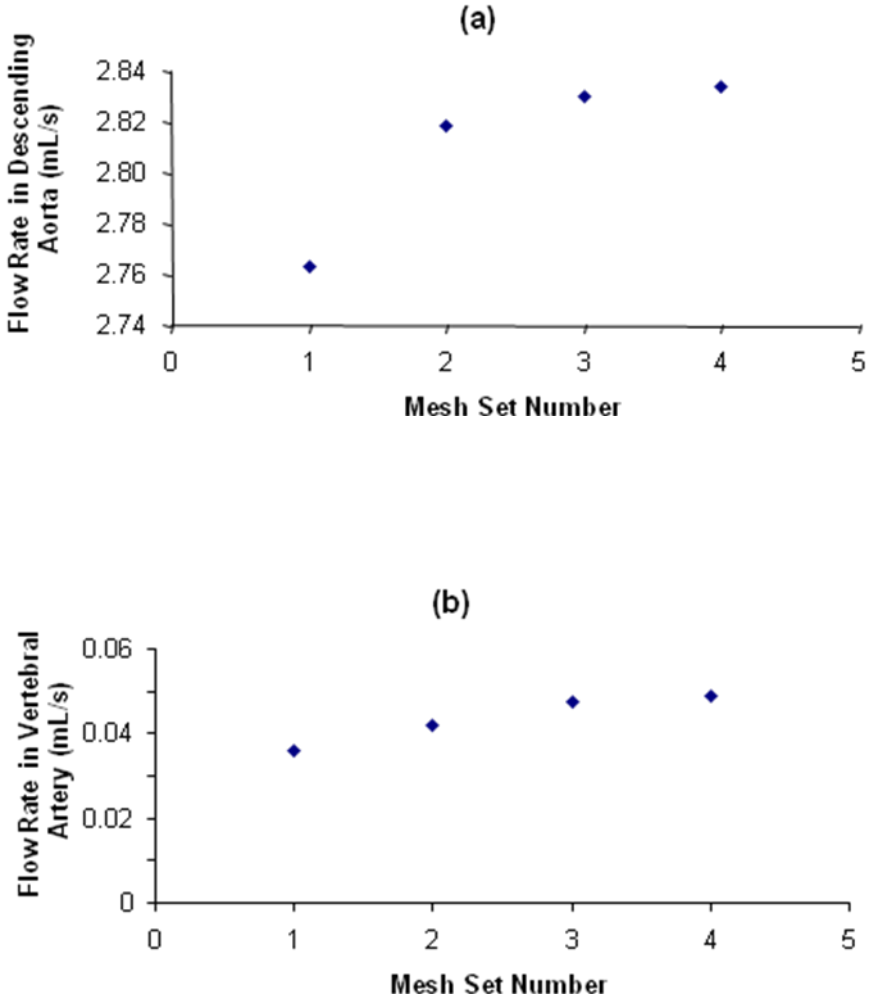

Figure 3-5. Average flow rate in the descending aorta (a), and in the vertebral artery (b) as a function of mesh sizes that shown in table 3-1.

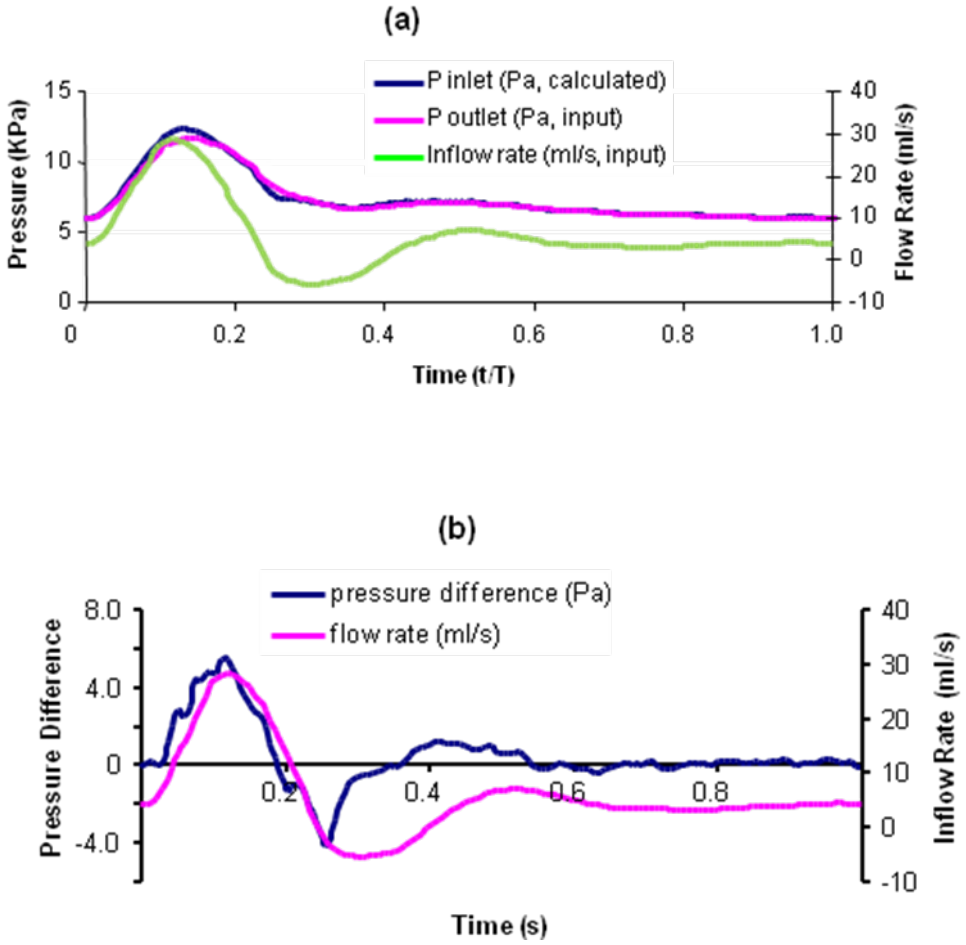

Fig 3-6. Waveforms of flow rate into the model and pressures at the inlet and outlets of the model (a). Pressure difference between the inlet and outlet (b).

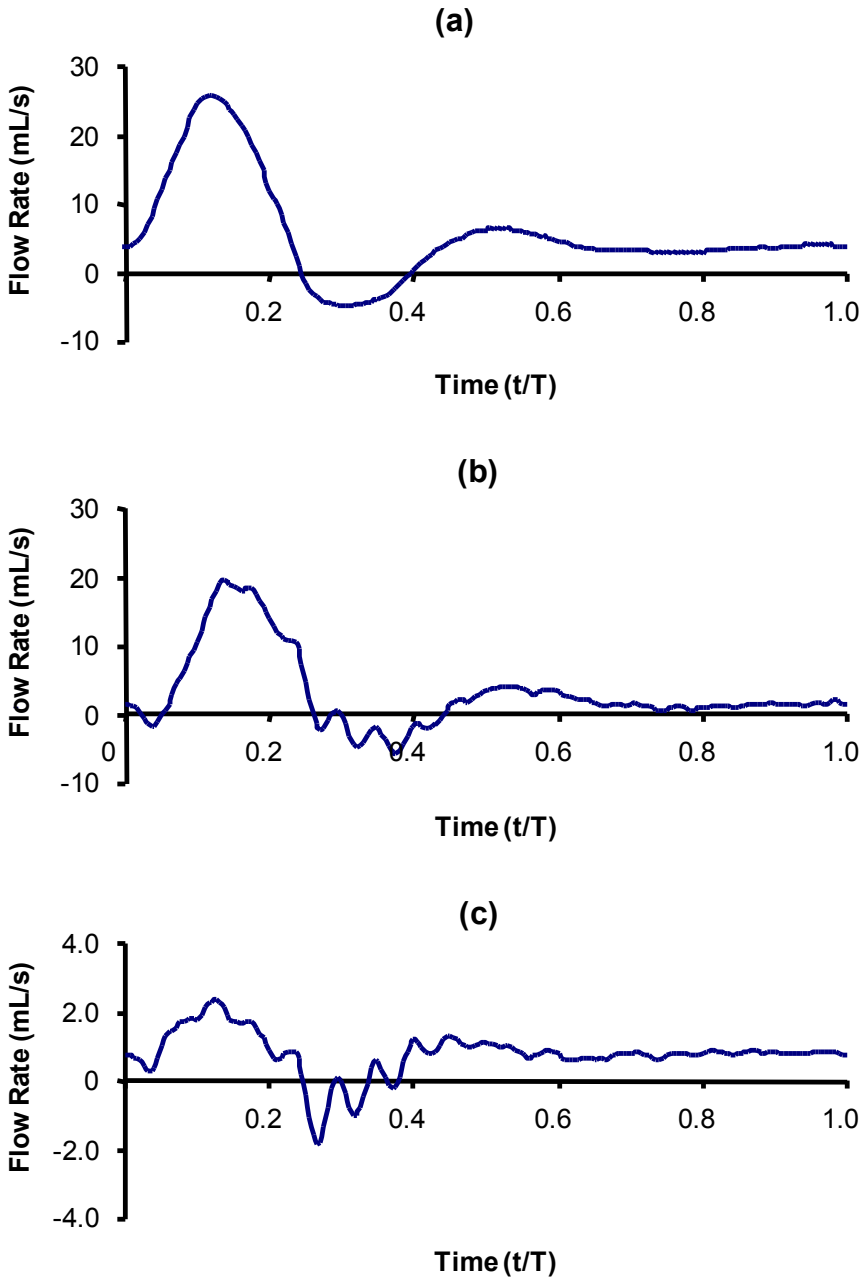

Figure 3-7. Flow rates in the branches: (a) ascending aorta; (b) descending aorta; (c) right subclavian artery, of the aneurysm model.

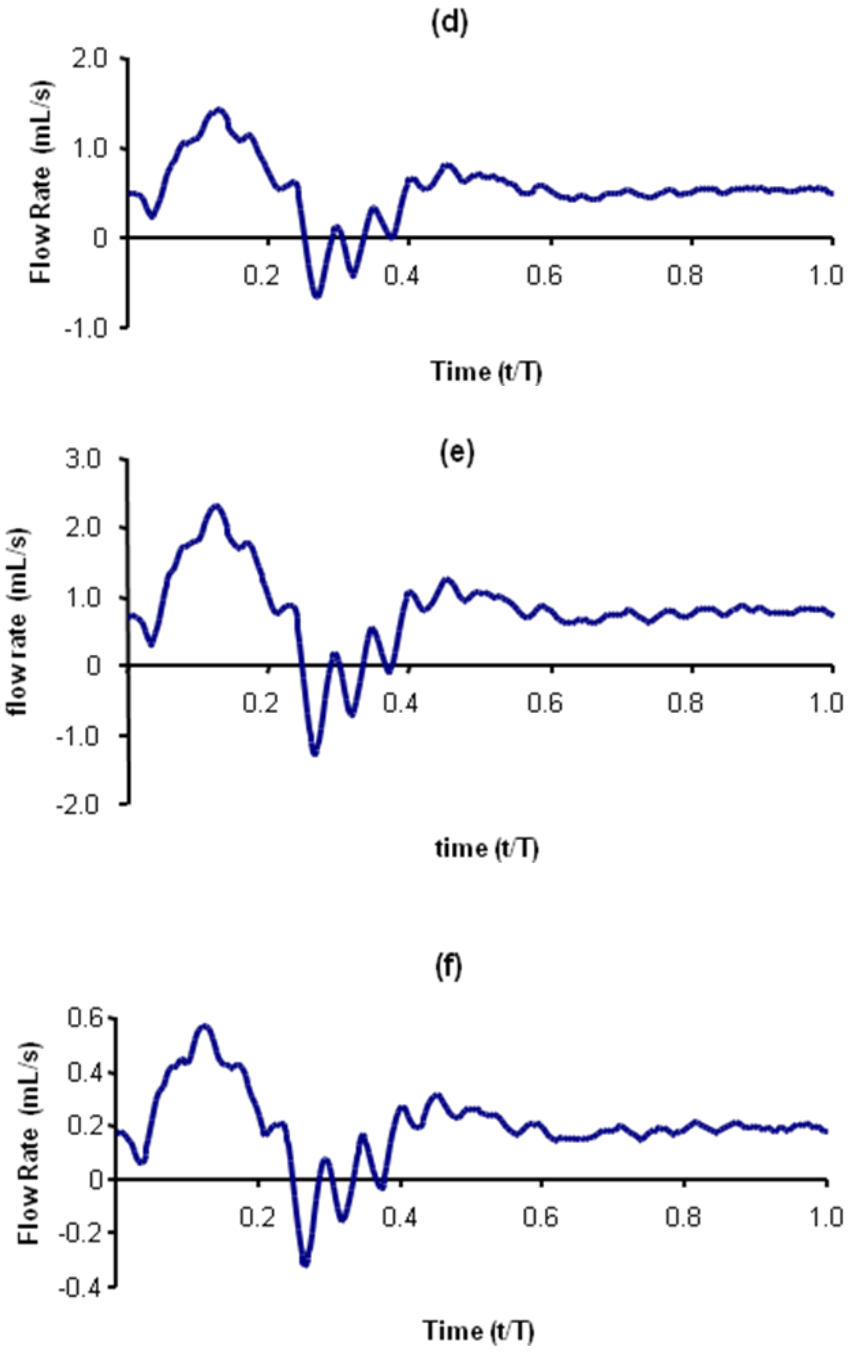

Figure 3-7. Flow rates in the branches: (d) left subclavian; (e) left common carotid artery; (f) vertebral artery, of the aneurysm model.

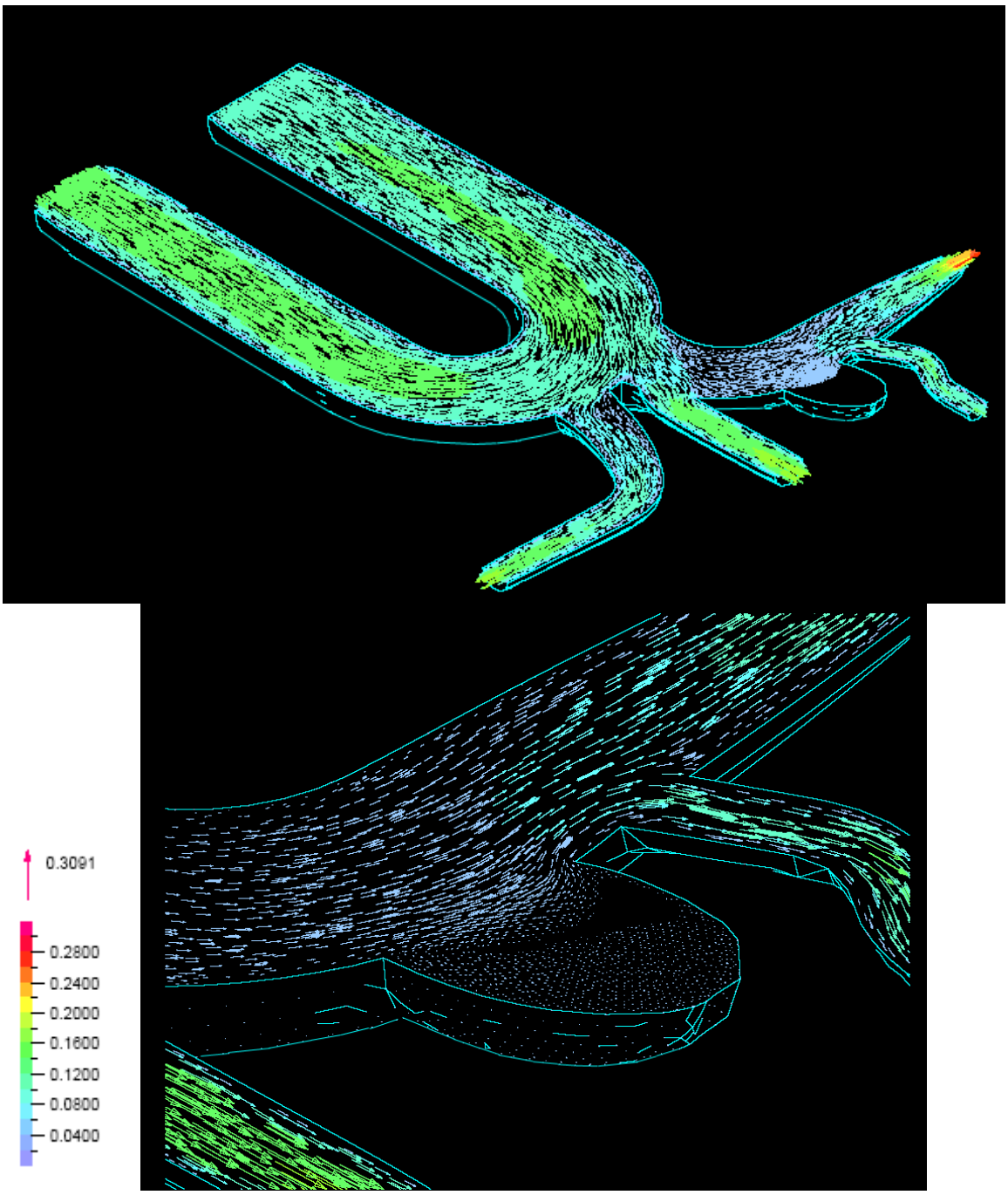

Figure 3-8. The velocity field in the aneurysm model at time t/T=0.132 (velocity units are m/s). The velocity scale is shown by the vector above the color scale.

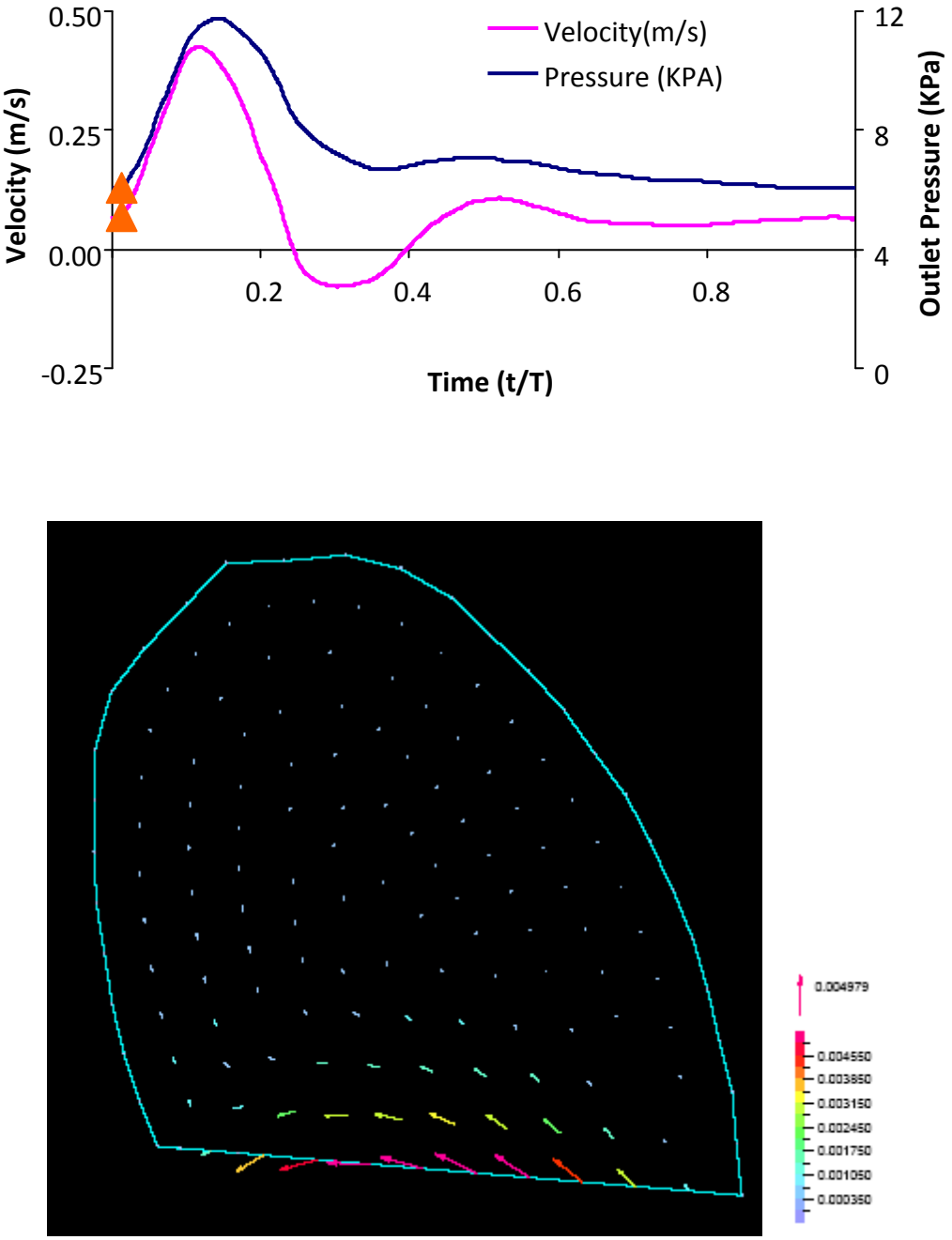

Figure 3-9. The velocity field inside the aneurysm sac at t/T =0.012 (orange triangles in the top inset). The velocity scale is shown by the vector above the color scale. Velocity units are m/s.

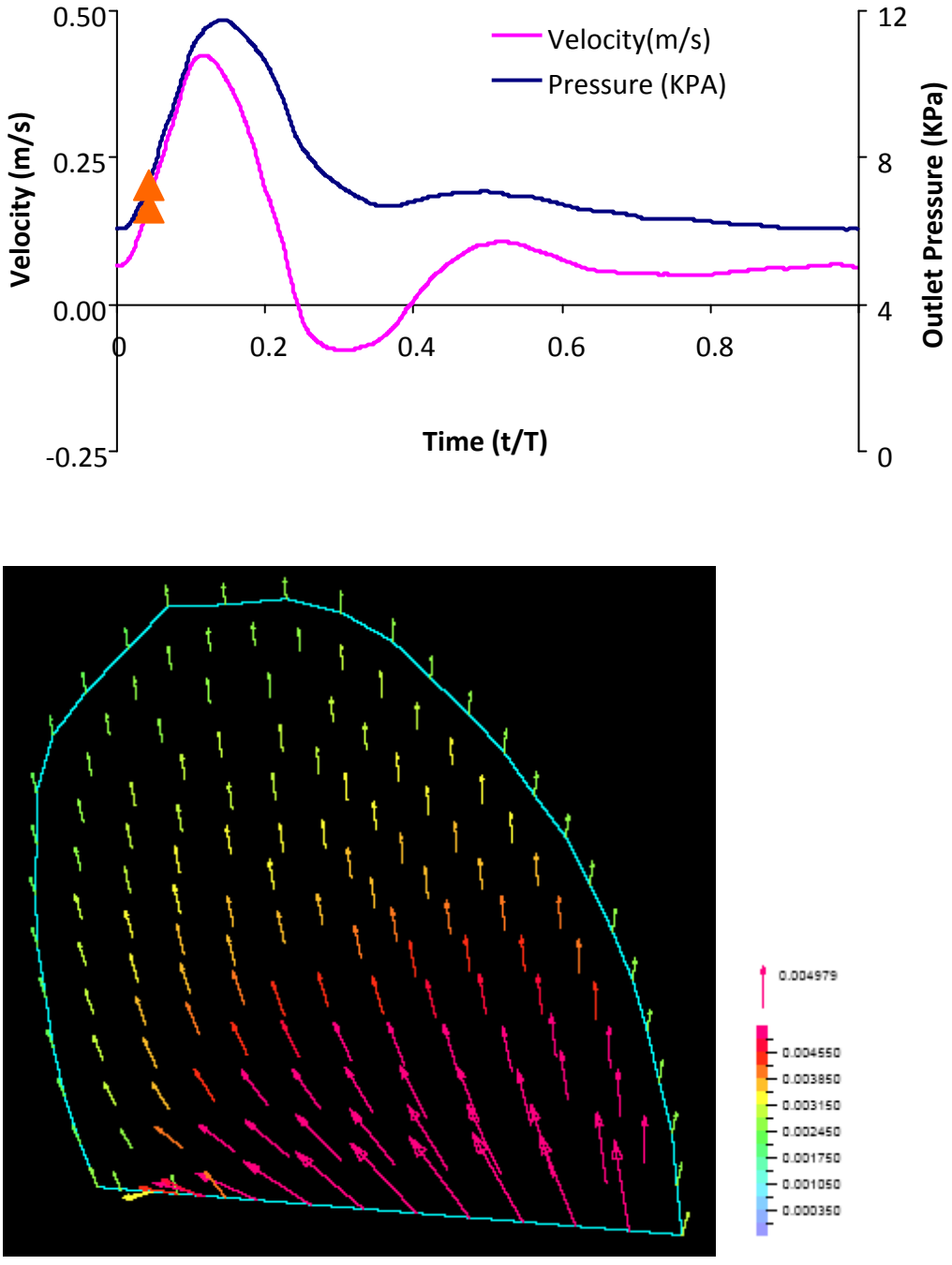

Figure 3-10. The velocity field inside the aneurysm sac at t/T =0.042 (orange triangles in the top inset). The velocity scale is shown by the vector above the color scale. Velocity units are m/s.

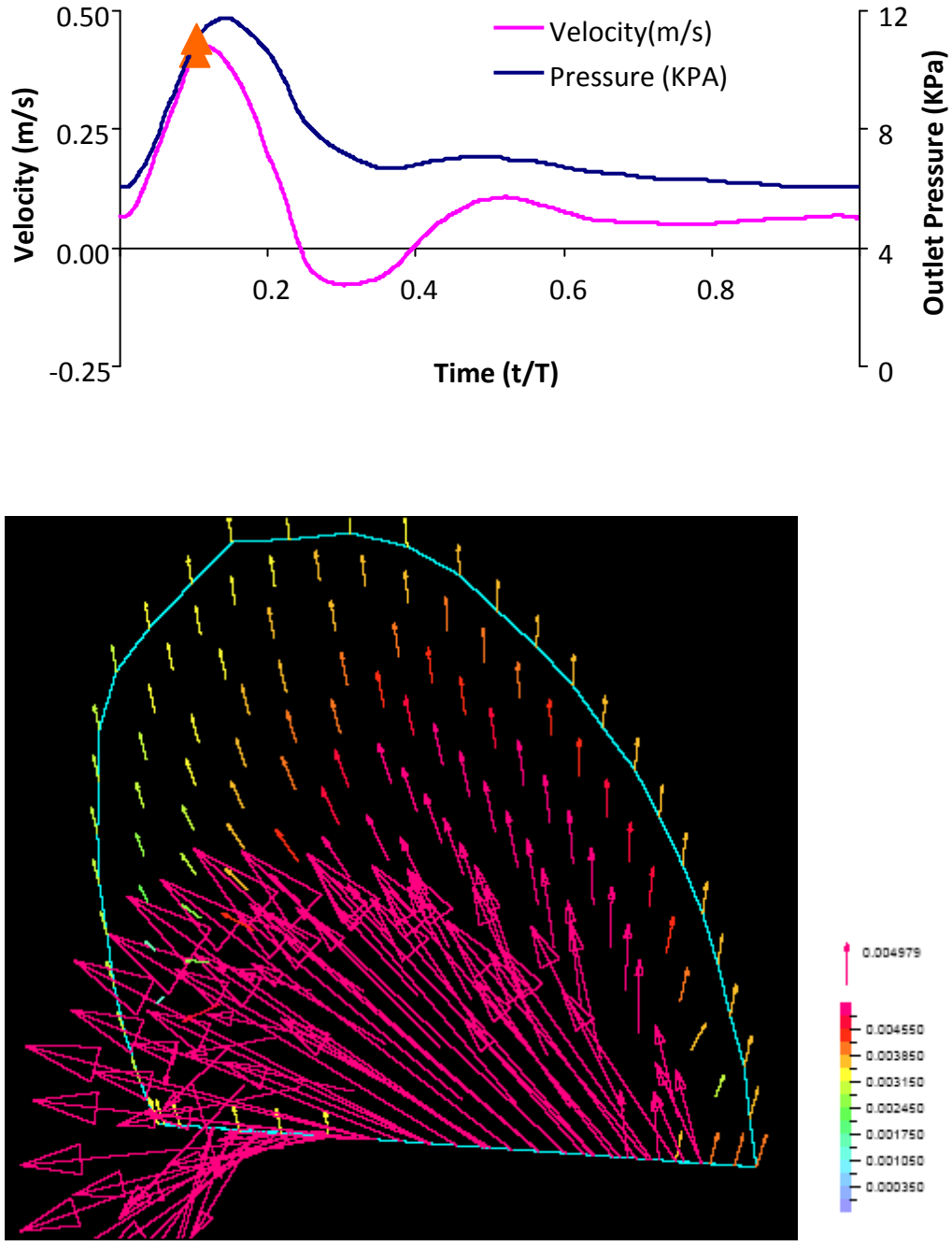

Figure 3-11. The velocity field inside the aneurysm sac at t/T =0.102 (orange triangles in the top inset). The velocity scale is shown by the vector above the color scale. Velocity units are m/s.

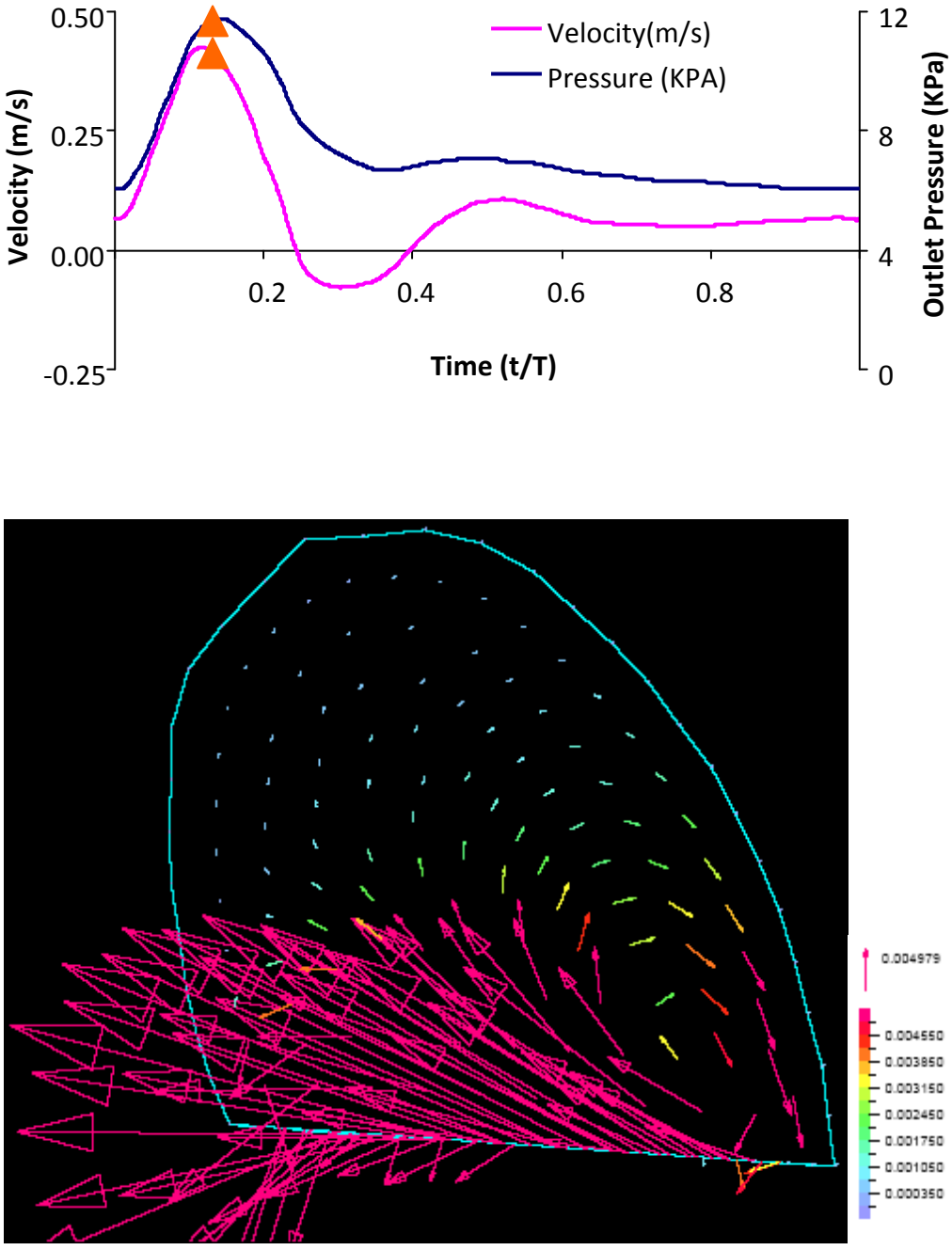

Figure 3-12. The velocity field inside the aneurysm sac at t/T =0.132 (orange triangles in the top inset). The velocity scale is shown by the vector above the color scale. Velocity units are m/s.

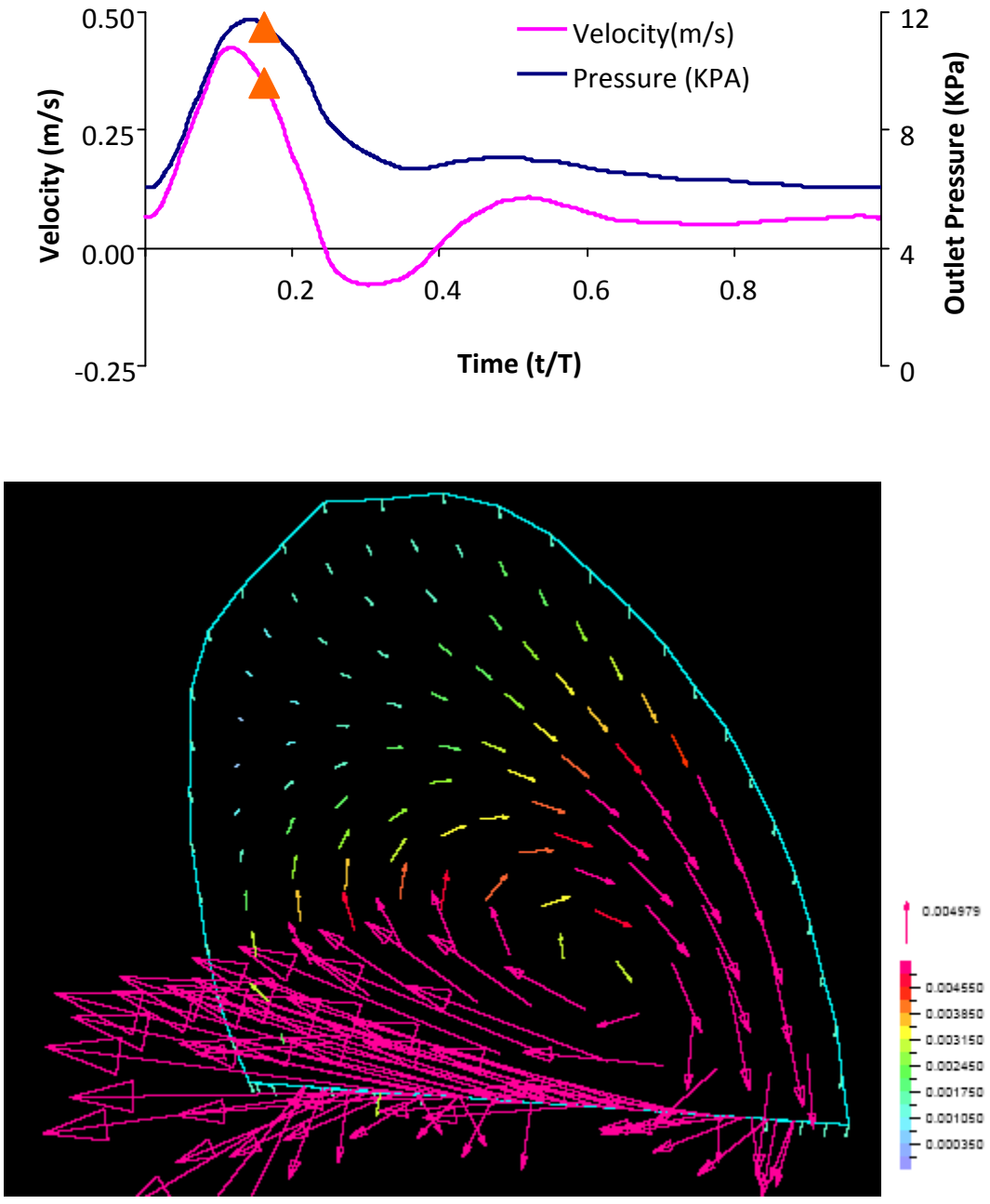

Figure 3-13. The velocity field inside the aneurysm sac at t/T =0.162 (orange triangles in the top inset). The velocity scale is shown by the vector above the color scale. Velocity units are m/s.

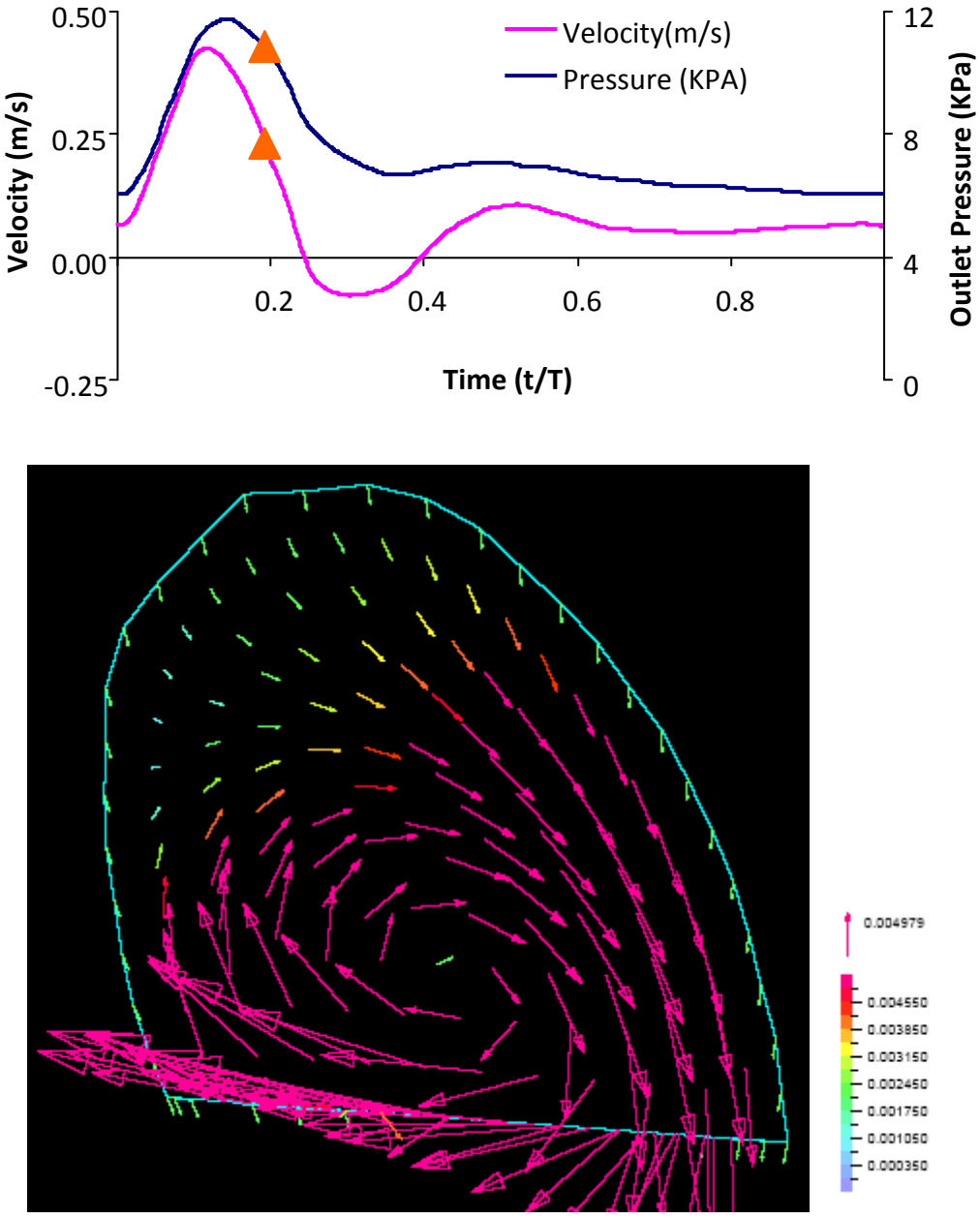

Figure 3-14. The velocity field inside the aneurysm sac at t/T =0.192 (orange triangles in the top inset). The velocity scale is shown by the vector above the color scale. Velocity units are m/s.

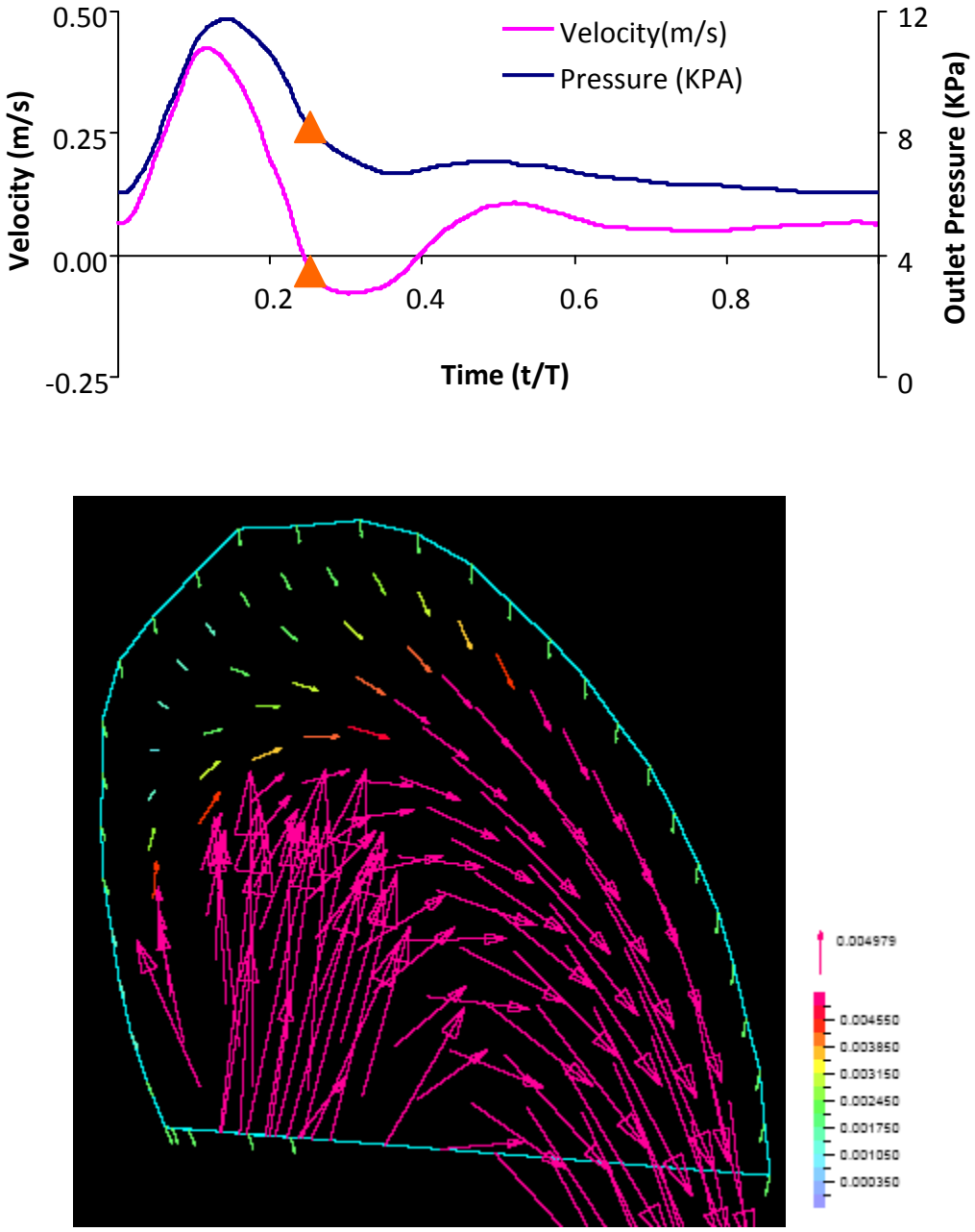

Figure 3-15. The velocity field inside the aneurysm sac at t/T =0.252 (orange triangles in the top inset). The velocity scale is shown by the vector above the color scale. Velocity units are m/s.

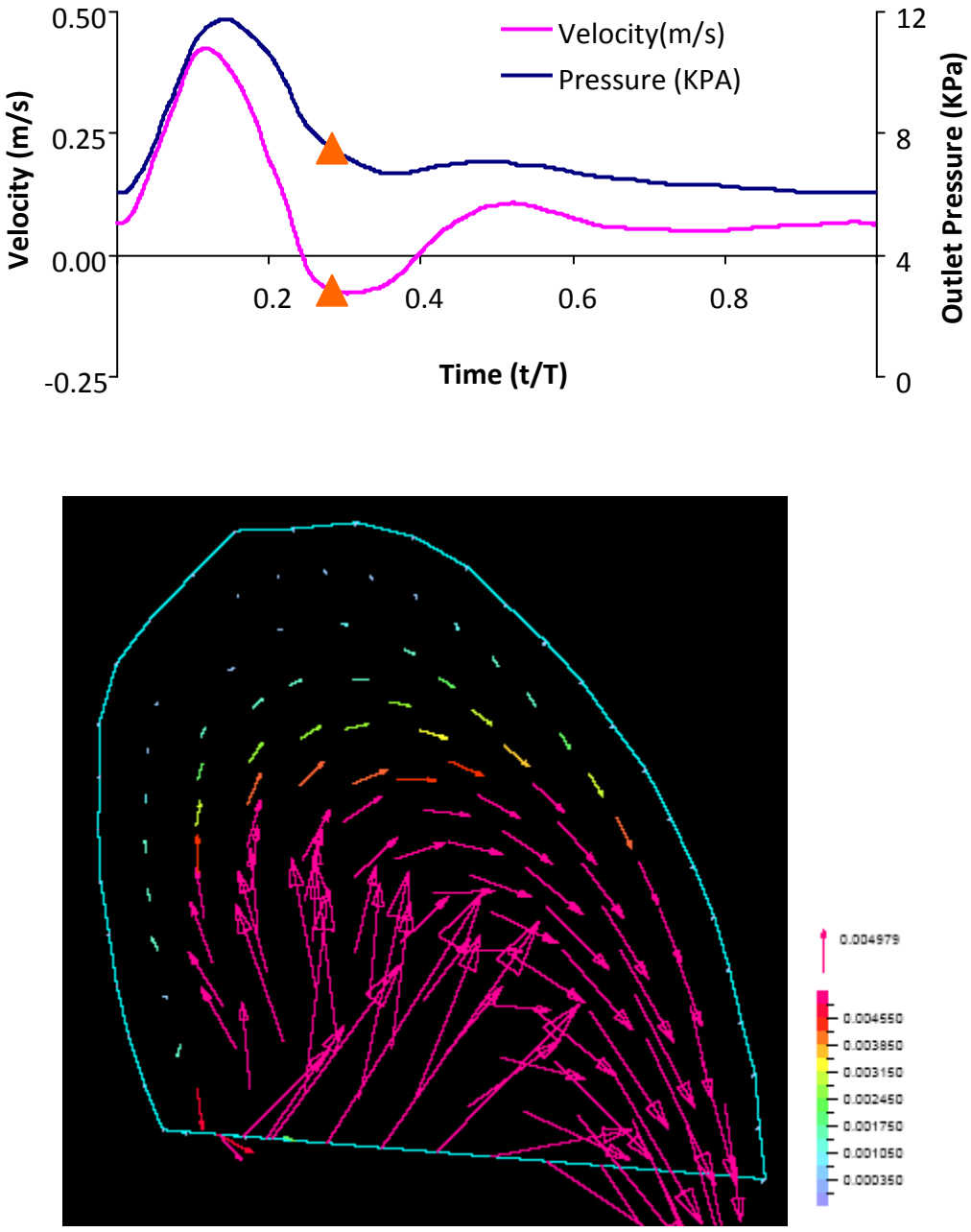

Figure 3-16. The velocity field inside the aneurysm sac at t/T =0.282 (orange triangles in the top inset). The velocity scale is shown by the vector above the color scale. Velocity units are m/s.

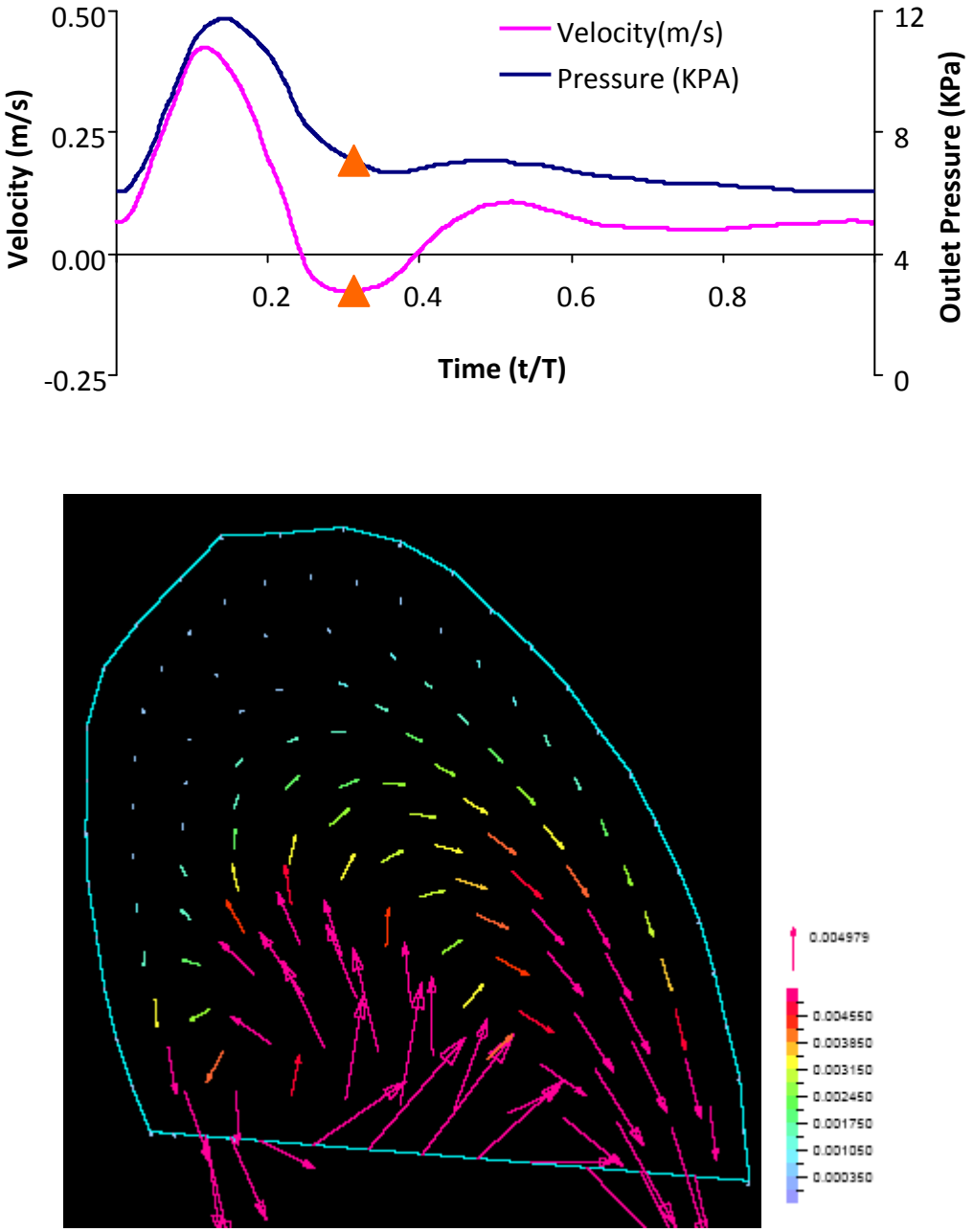

Figure 3-17. The velocity field inside the aneurysm sac at t/T =0.312 (orange triangles in the top inset). The velocity scale is shown by the vector above the color scale. Velocity units are m/s.

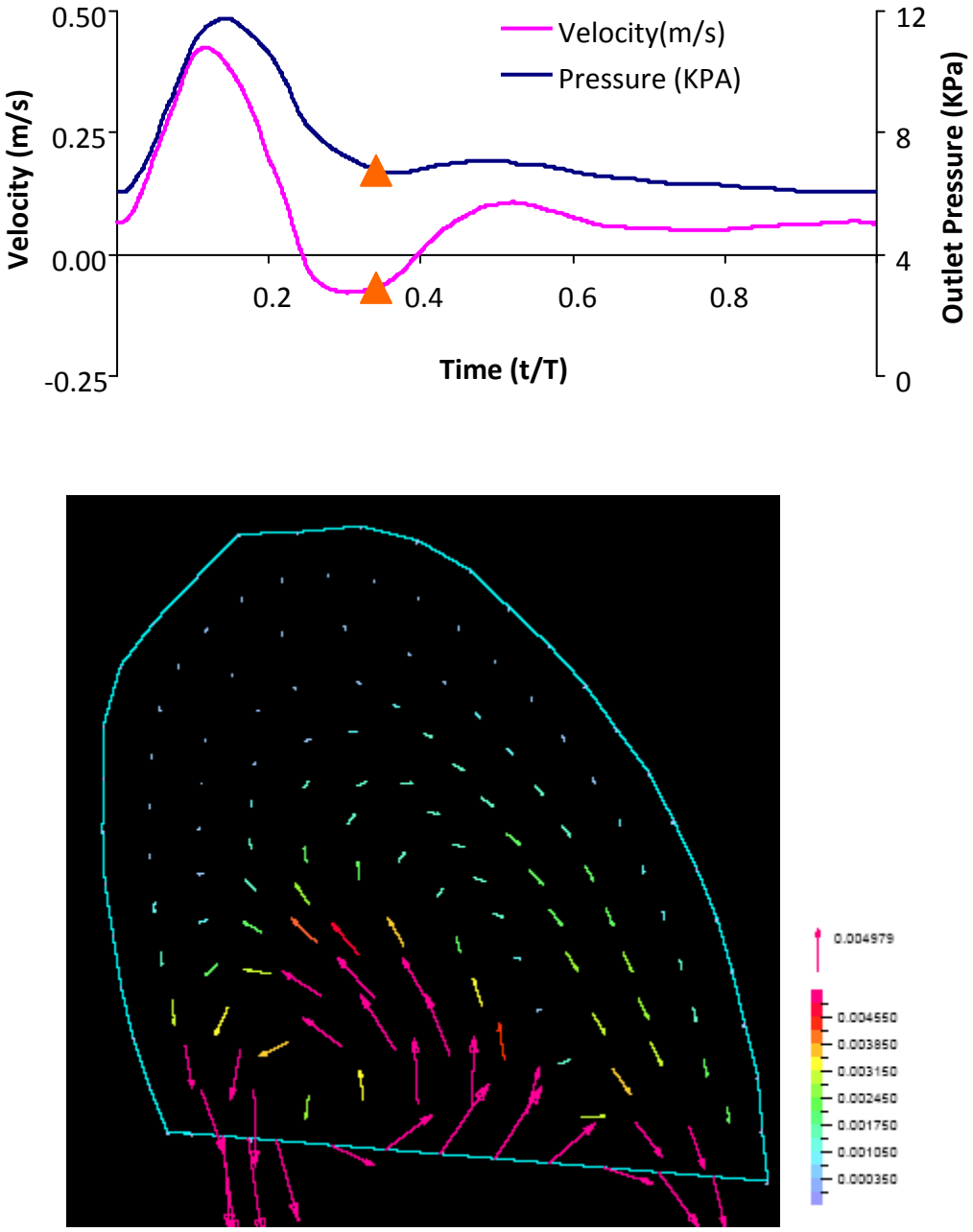

Figure 3-18. The velocity field inside the aneurysm sac at t/T =0.342 (orange triangles in the top inset). The velocity scale is shown by the vector above the color scale. Velocity units are m/s.

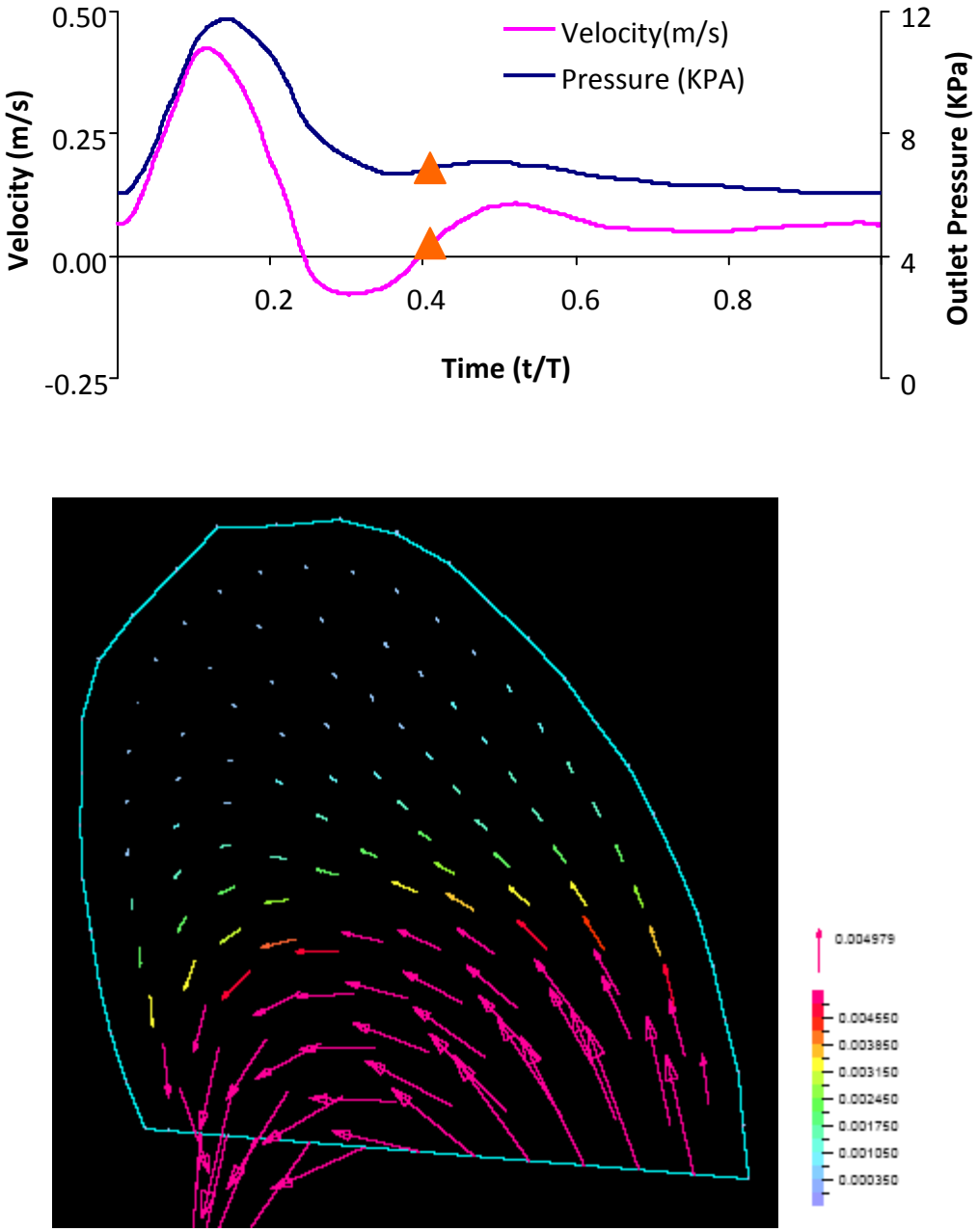

Figure 3-19. The velocity field inside the aneurysm sac at t/T =0.410 (orange triangles in the top inset). The velocity scale is shown by the vector above the color scale. Velocity units are m/s.

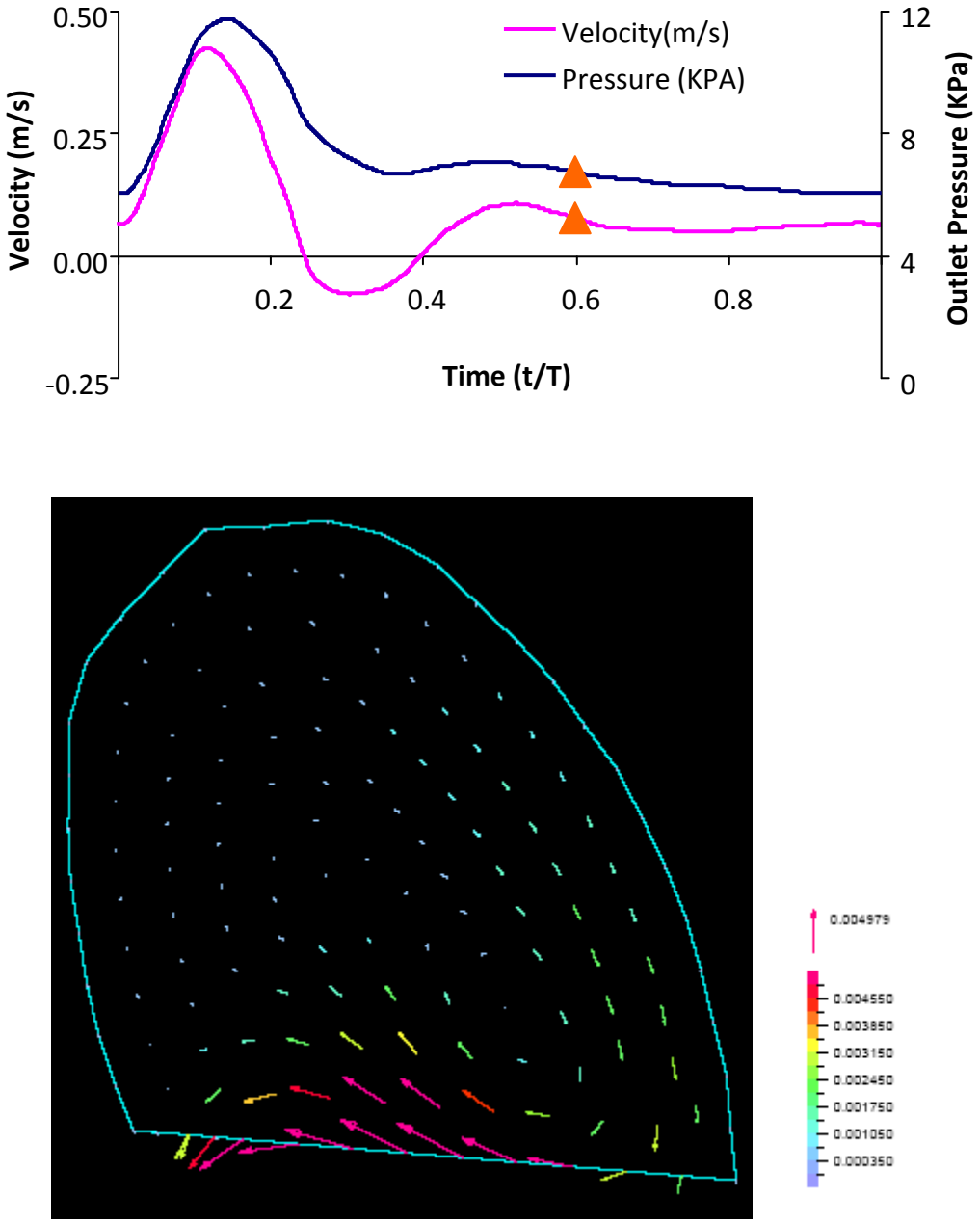

Figure 3-20. The velocity field inside the aneurysm sac at t/T =0.5975 (orange triangles in the top inset). The velocity scale is shown by the vector above the color scale. Velocity units are m/s.

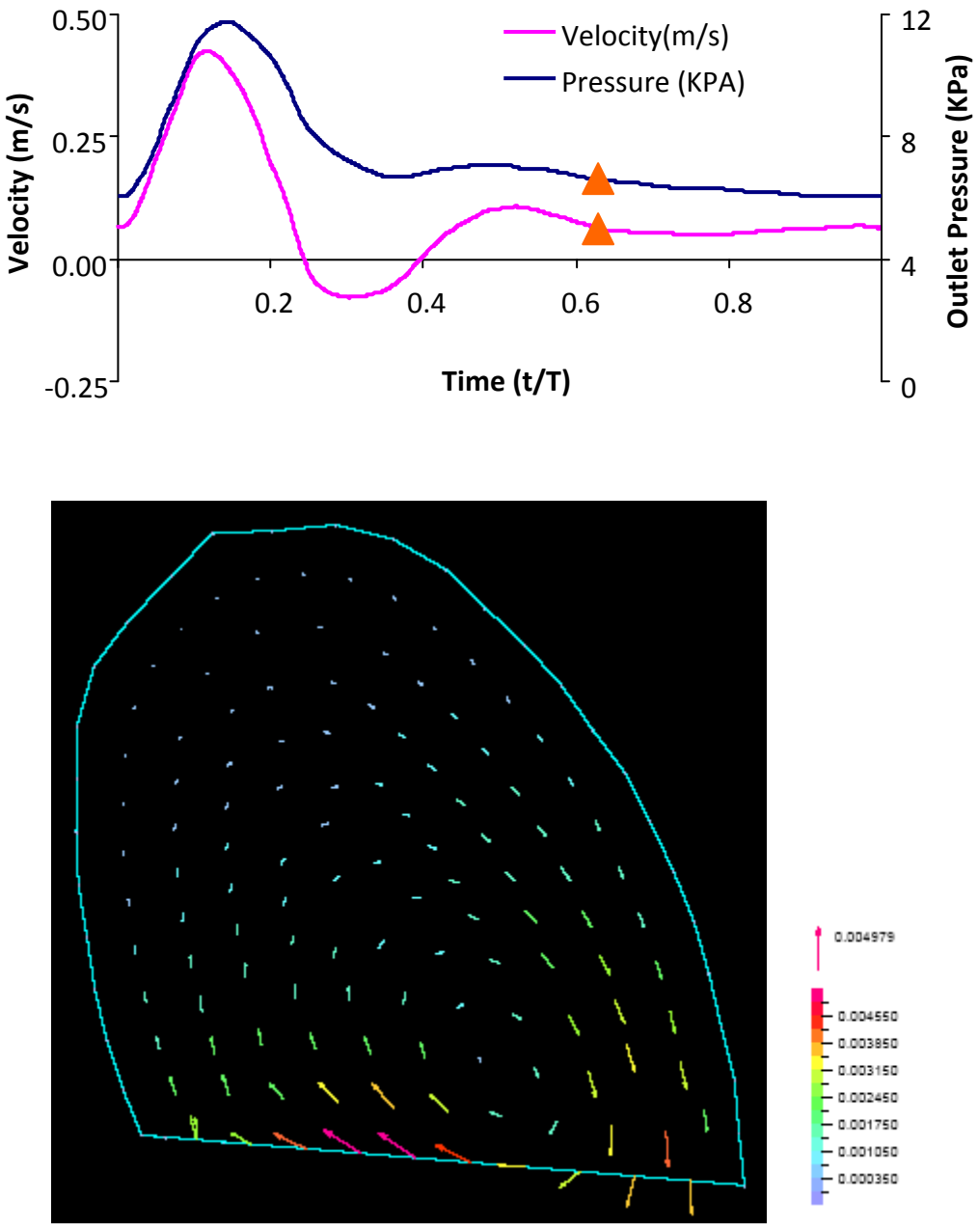

Figure 3-21. The velocity field inside the aneurysm sac at t/T =0.6275 (orange triangles in the top inset). The velocity scale is shown by the vector above the color scale. Velocity units are m/s.

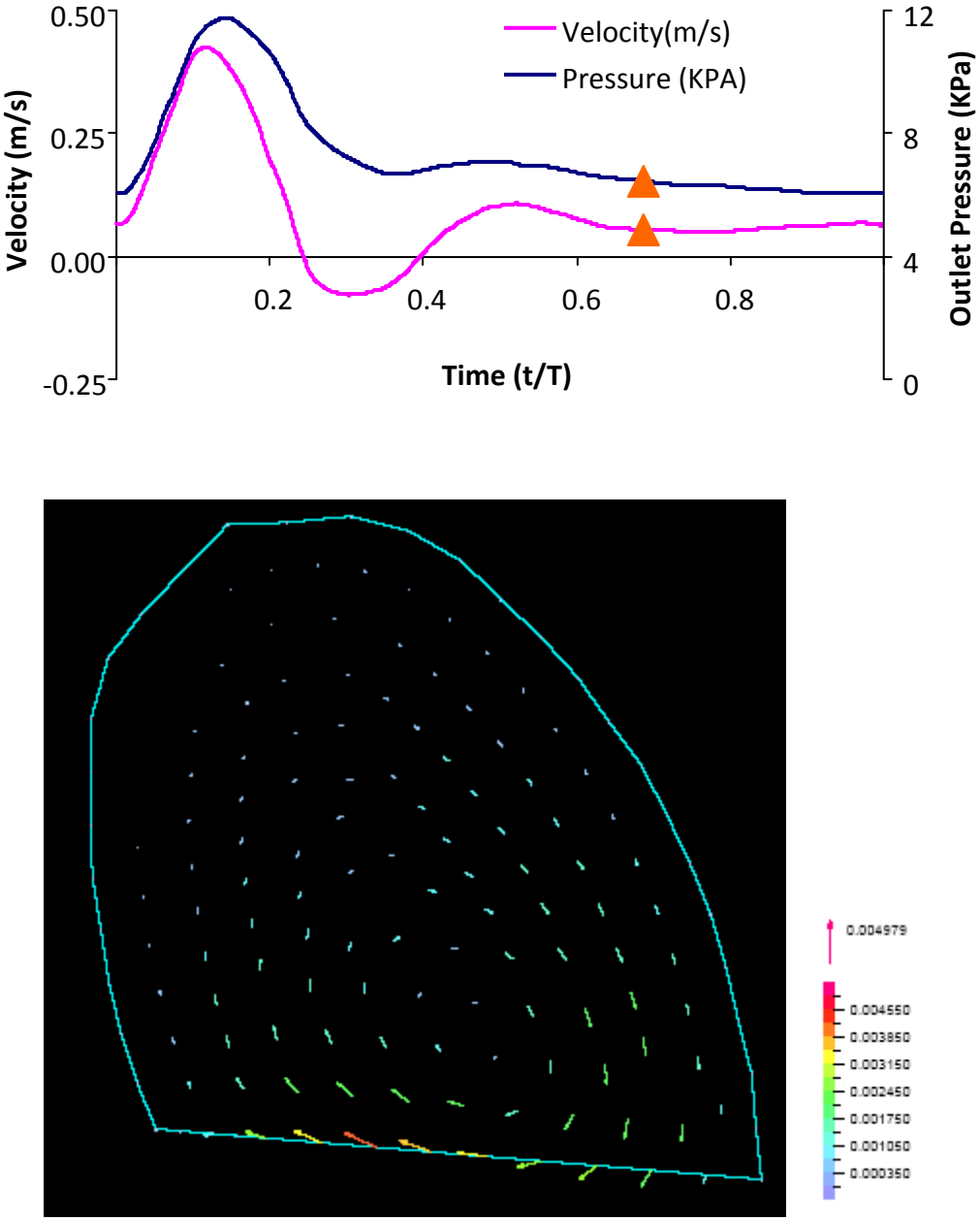

Figure 3-22. The velocity field inside the aneurysm sac at t/T =0.6875 (orange triangles in the top inset). The velocity scale is shown by the vector above the color scale. Velocity units are m/s.

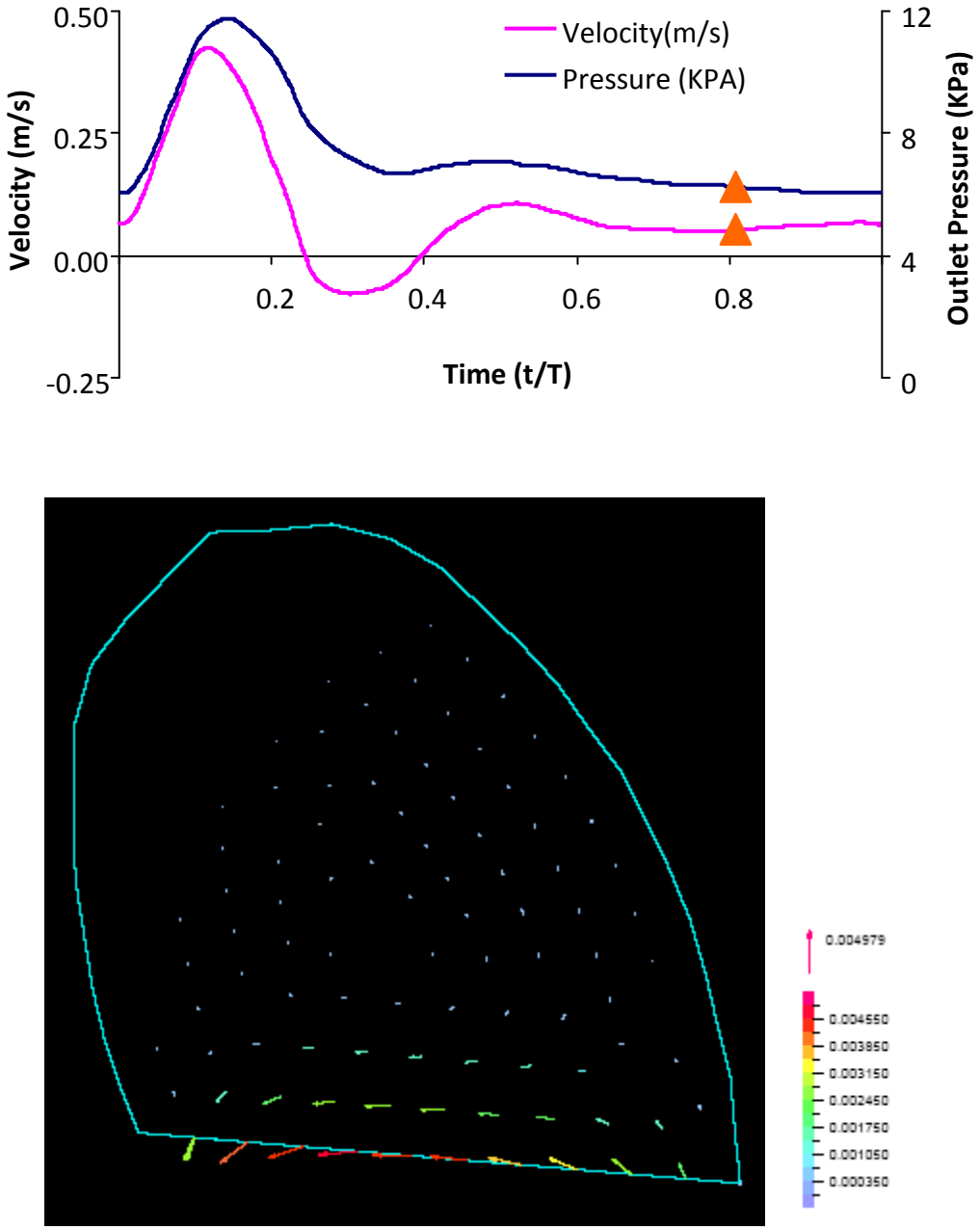

Figure 3-23. The velocity field inside the aneurysm sac at t/T =0.8075 (orange triangles in the top inset). The velocity scale is shown by the vector above the color scale. Velocity units are m/s.

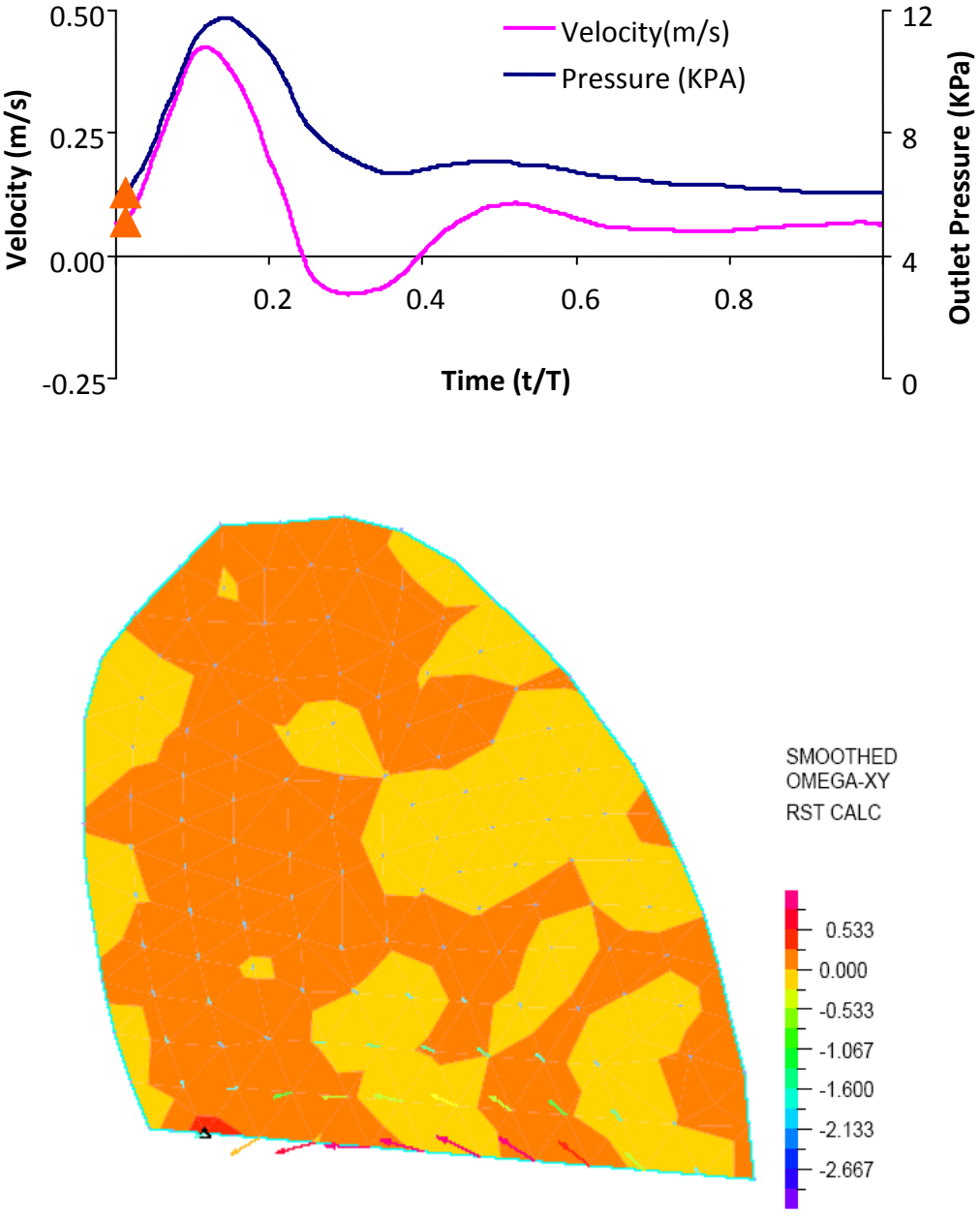

Figure 3-24. Contours of vorticity in the plane of symmetry of the aneurysm (x-y plane) at t/T =0.012 (orange triangle in the top inset). Vorticity units shown by the color scale are sec^{-1}. Velocity vectors are superposed on the vorticity contours.

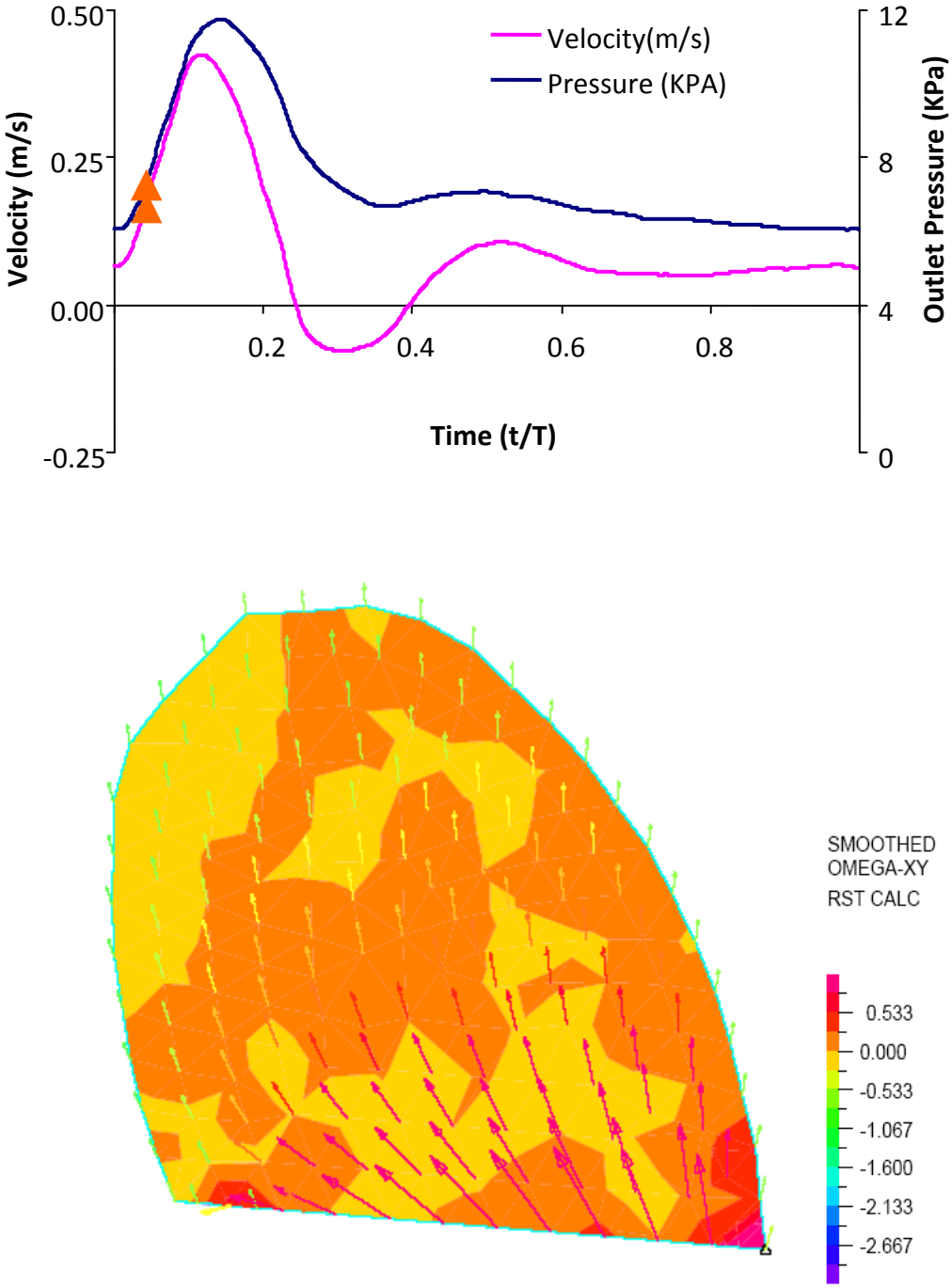

Figure 3-25. Contours of vorticity in the plane of symmetry of the aneurysm (x-y plane) at t/T =0.042 (orange triangle in the top inset). Vorticity units shown by the color scale are sec^{-1}. Velocity vectors are superposed on the vorticity contours.

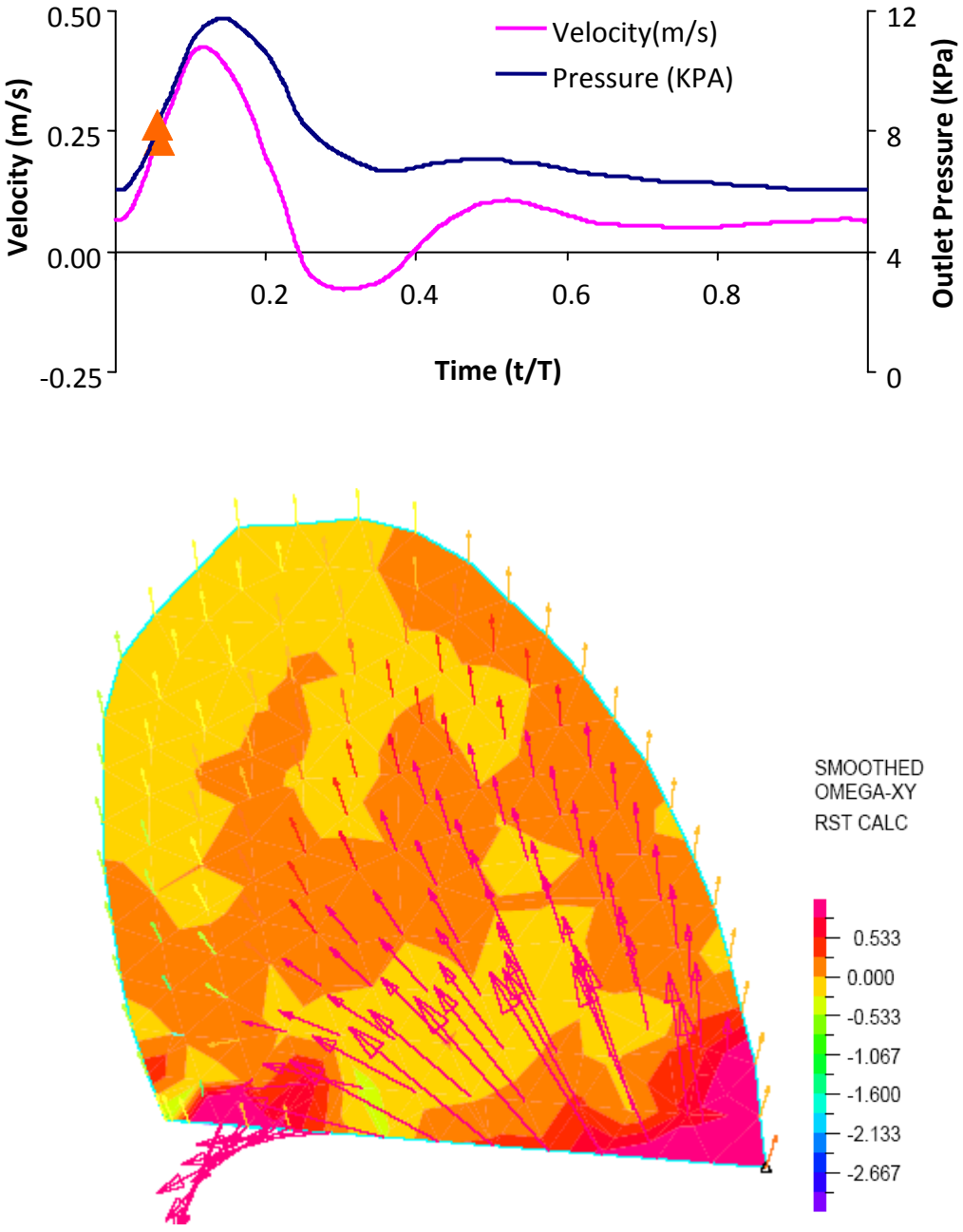

(c)

Figure 3-26. Contours of vorticity in the plane of symmetry of the aneurysm (x-y plane) at t/T =0.057 (orange triangle in the top inset). Vorticity units shown by the color scale are sec^{-1}. Velocity vectors are superposed on the vorticity contours.

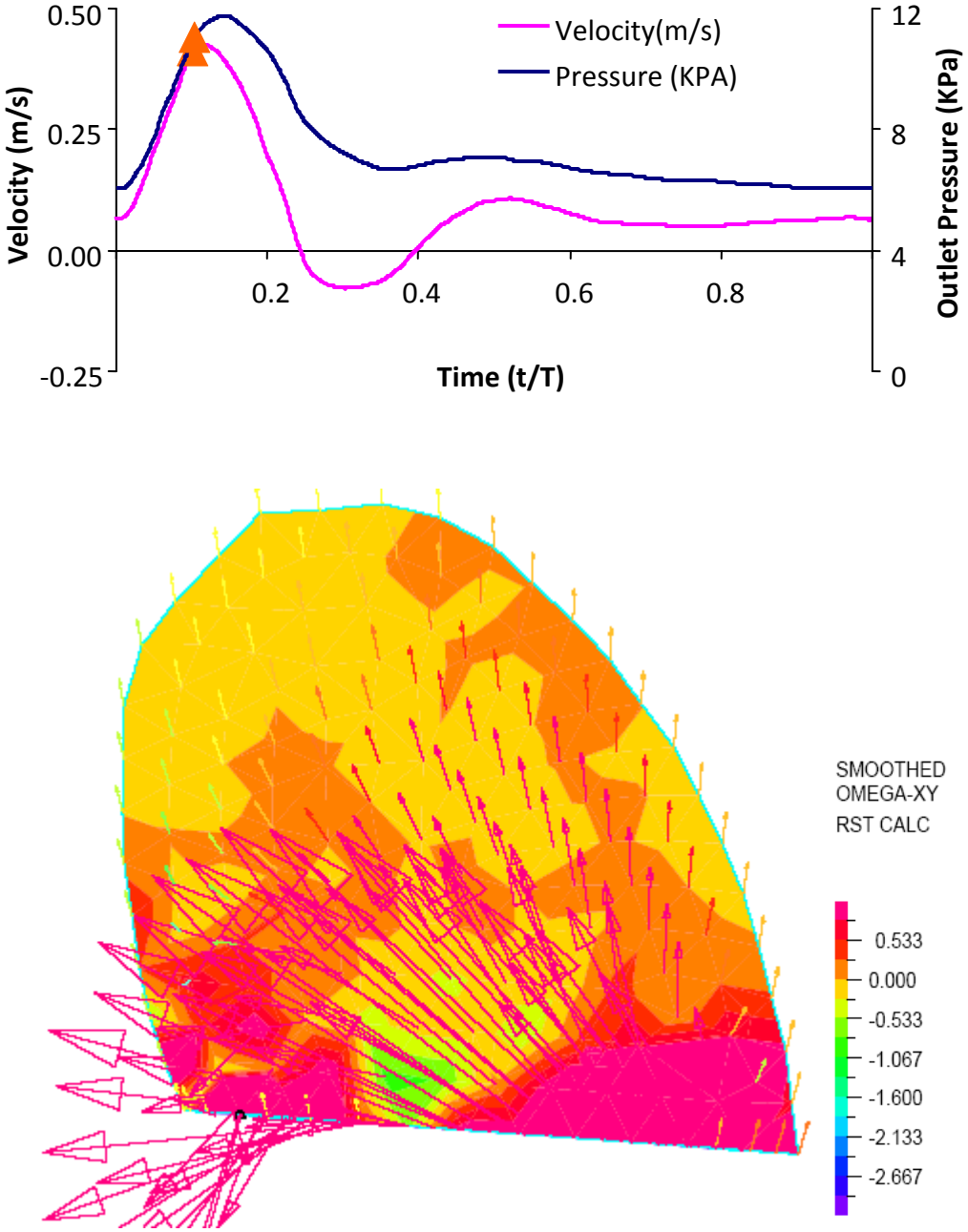

Figure 3-27. Contours of vorticity in the plane of symmetry of the aneurysm (x-y plane) at t/T =0.102 (orange triangle in the top inset). Vorticity units shown by the color scale are sec^{-1}. Velocity vectors are superposed on the vorticity contours.

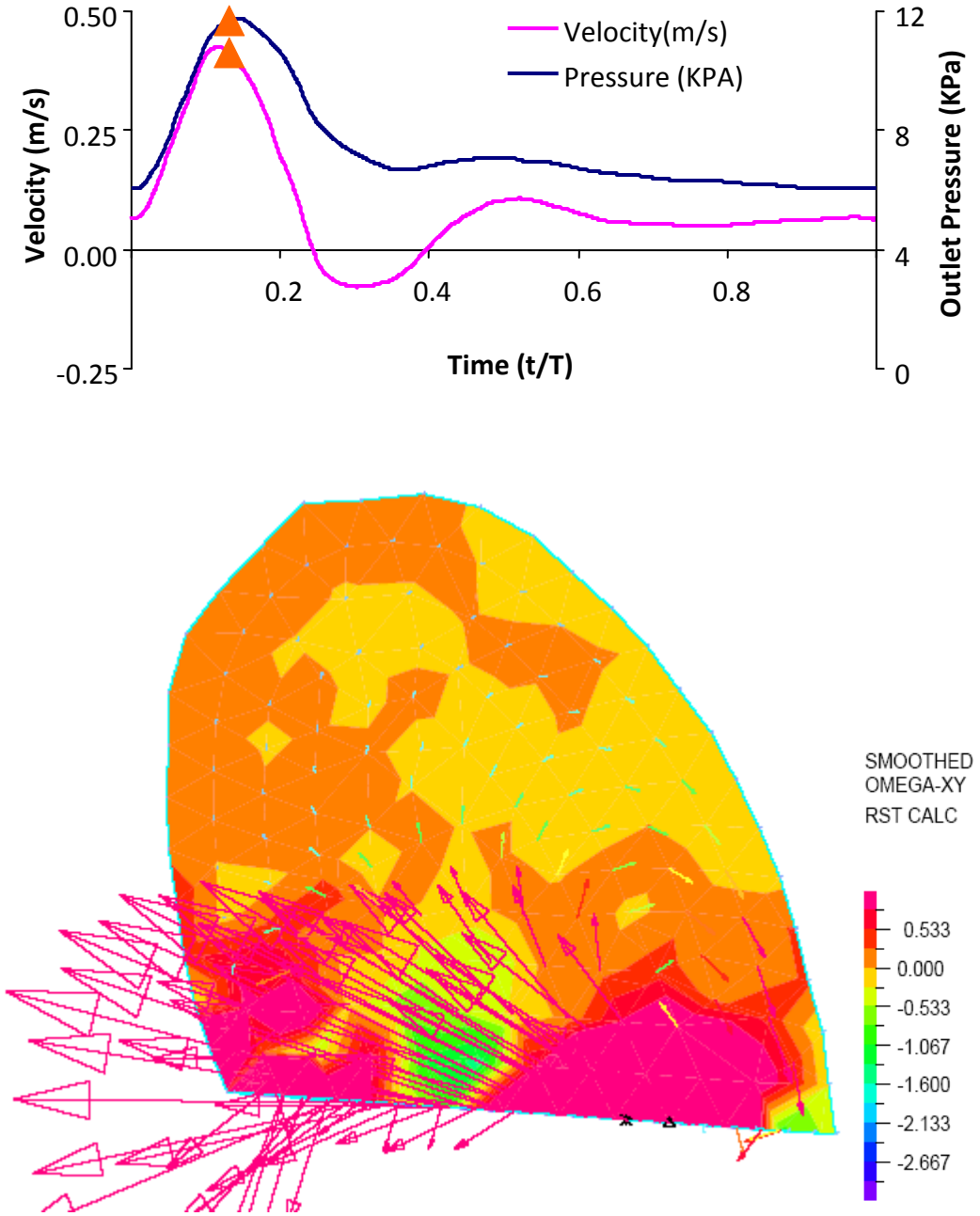

Figure 3-28. Contours of vorticity in the plane of symmetry of the aneurysm (x-y plane) at t/T =0.132 (orange triangle in the top inset). Vorticity units shown by the color scale are sec^{-1}. Velocity vectors are superposed on the vorticity contours.

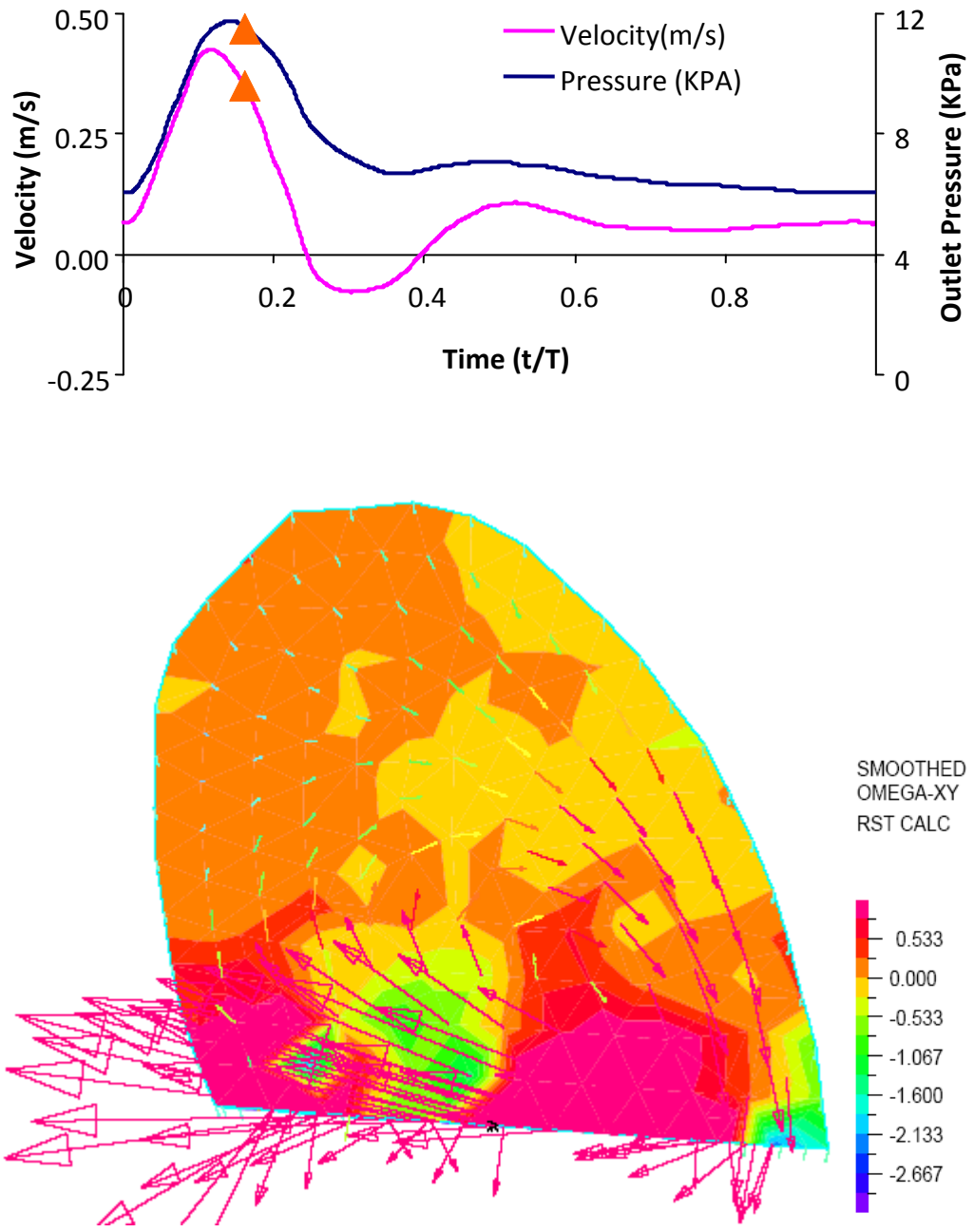

Figure 3-29. Contours of vorticity in the plane of symmetry of the aneurysm (x-y plane) at t/T =0.162 (orange triangle in the top inset). Vorticity units shown by the color scale are sec^{-1}. Velocity vectors are superposed on the vorticity contours.

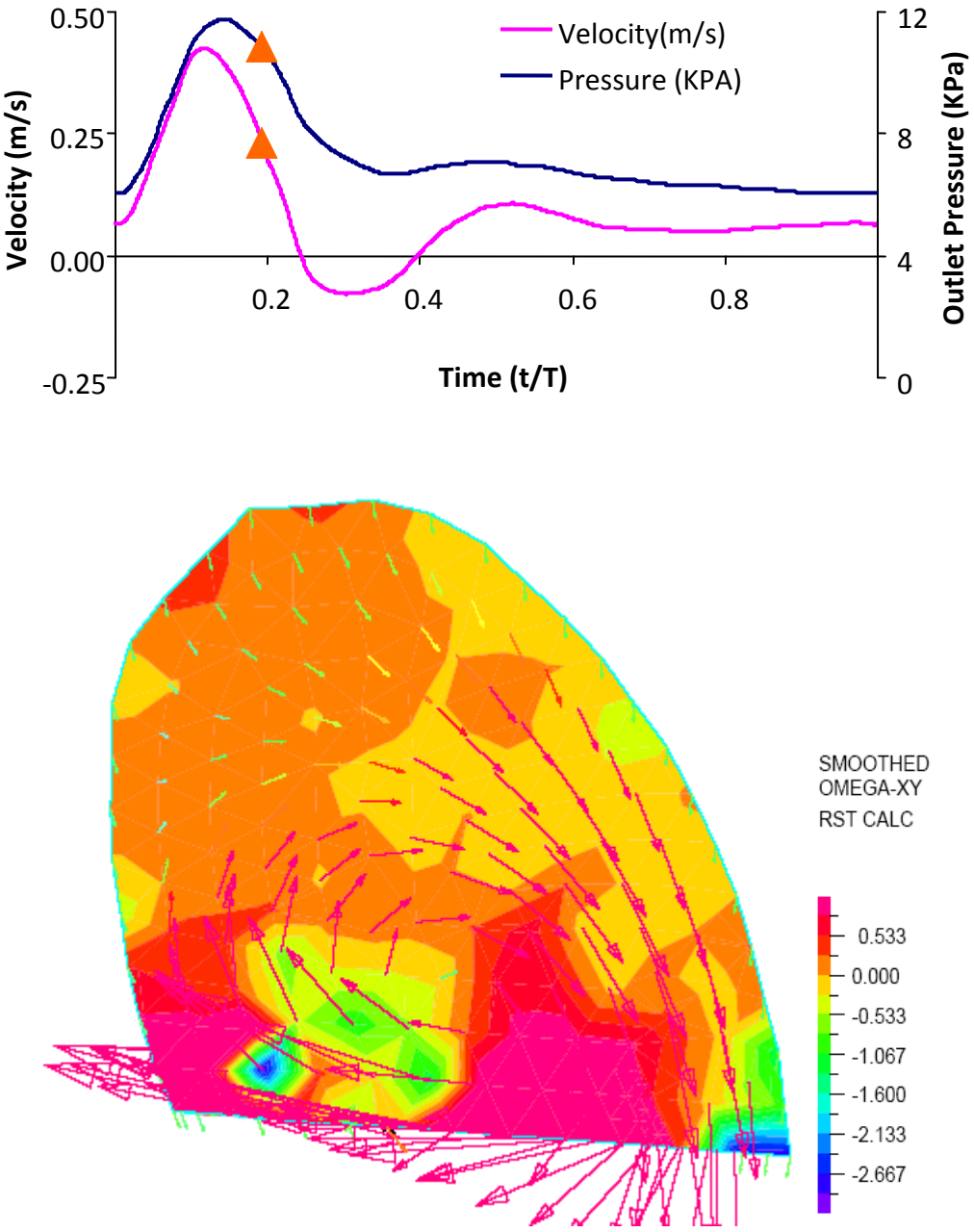

Figure 3-30. Contours of vorticity in the plane of symmetry of the aneurysm (x-y plane) at t/T =0.192 (orange triangle in the top inset). Vorticity units shown by the color scale are sec^{-1}. Velocity vectors are superposed on the vorticity contours.

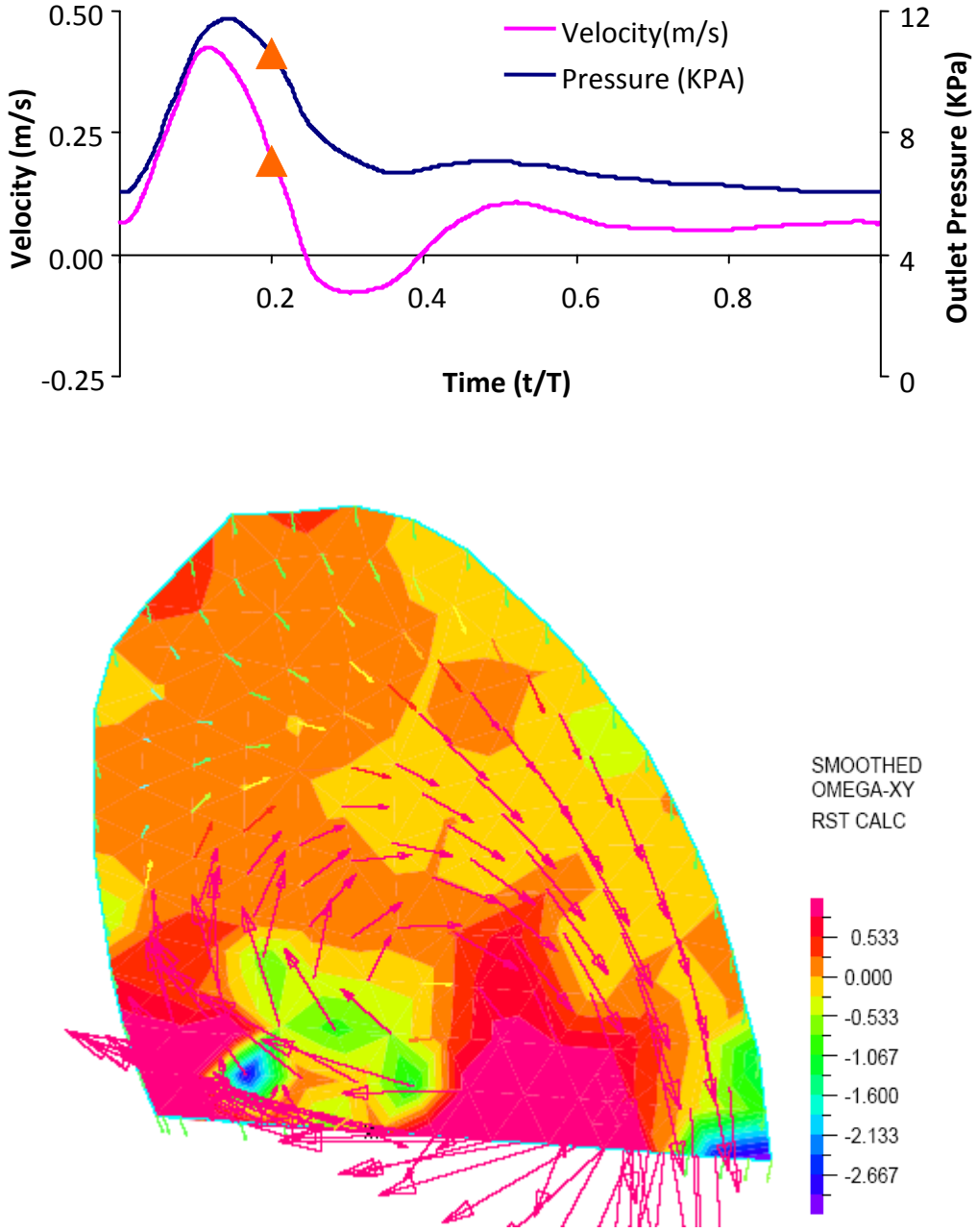

Figure 3-31. Contours of vorticity in the plane of symmetry of the aneurysm (x-y plane) at t/T =0.2 (orange triangle in the top inset). Vorticity units shown by the color scale are sec^{-1}. Velocity vectors are superposed on the vorticity contours.

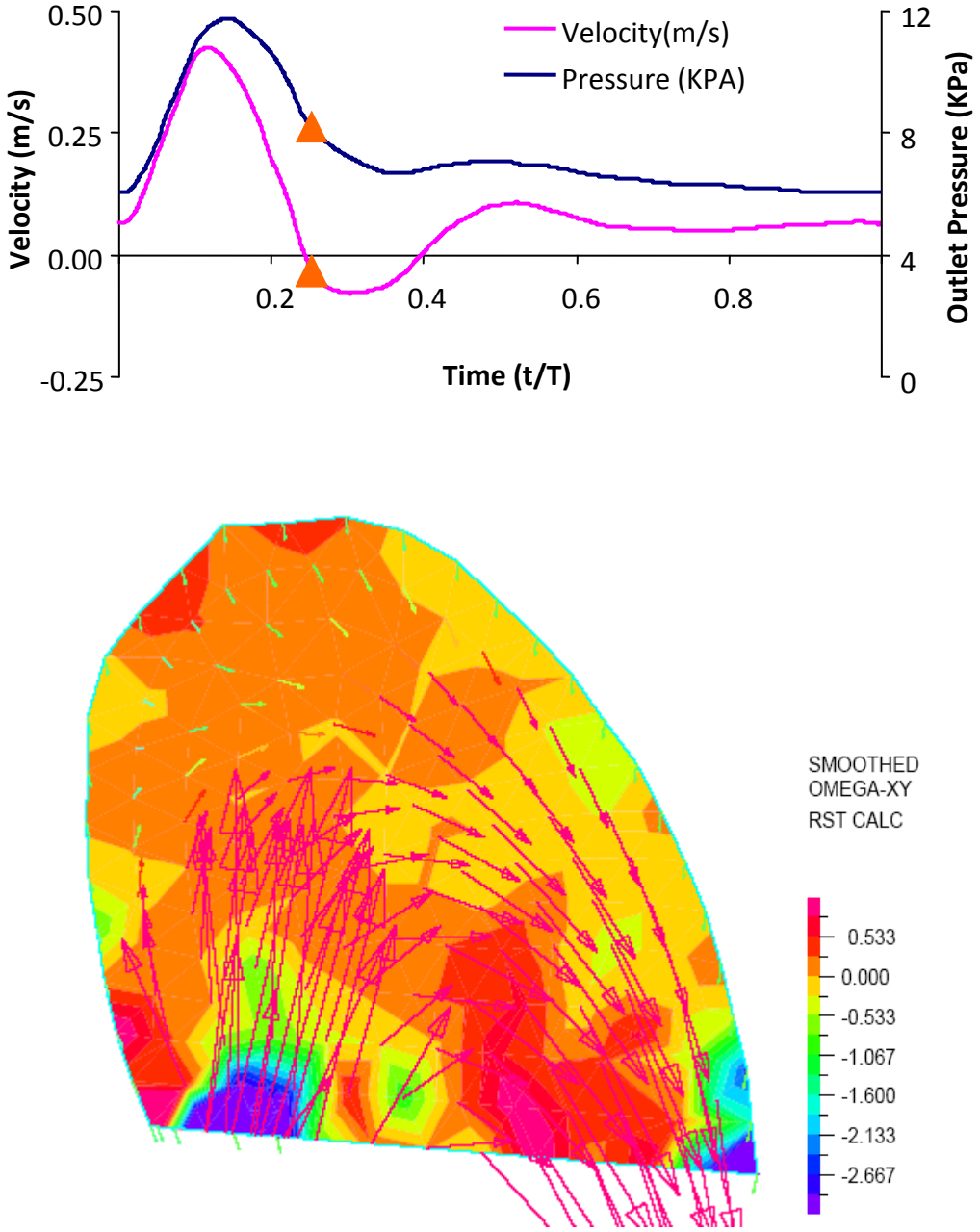

Figure 3-32. Contours of vorticity in the plane of symmetry of the aneurysm (x-y plane) at t/T =0.252 (orange triangle in the top inset). Vorticity units shown by the color scale are sec^{-1}. Velocity vectors are superposed on the vorticity contours.

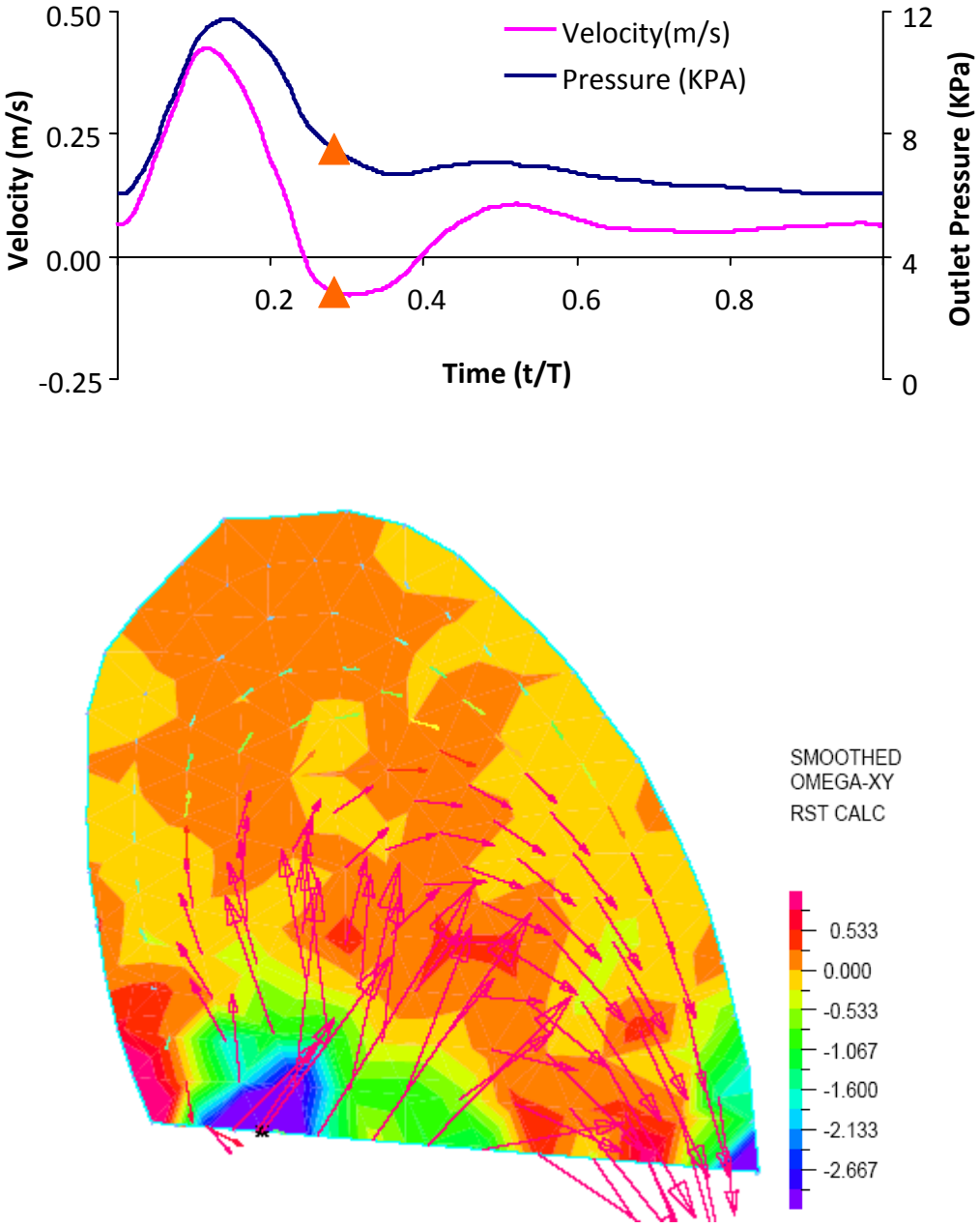

Figure 3-33. Contours of vorticity in the plane of symmetry of the aneurysm (x-y plane) at t/T =0.282 (orange triangle in the top inset). Vorticity units shown by the color scale are sec^{-1}. Velocity vectors are superposed on the vorticity contours.

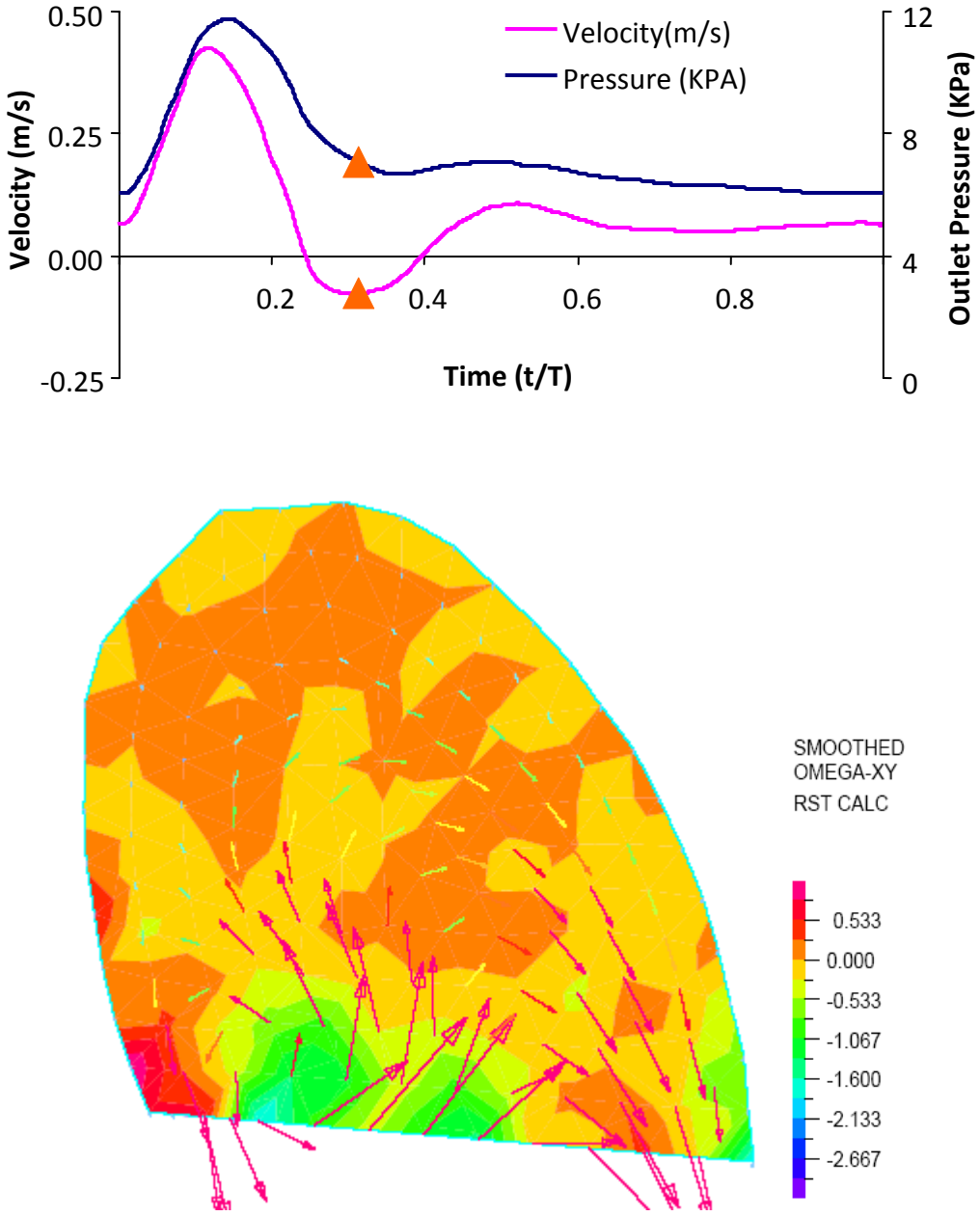

Figure 3-34. Contours of vorticity in the plane of symmetry of the aneurysm (x-y plane) at t/T =0.312 (orange triangle in the top inset). Vorticity units shown by the color scale are sec^{-1}. Velocity vectors are superposed on the vorticity contours.

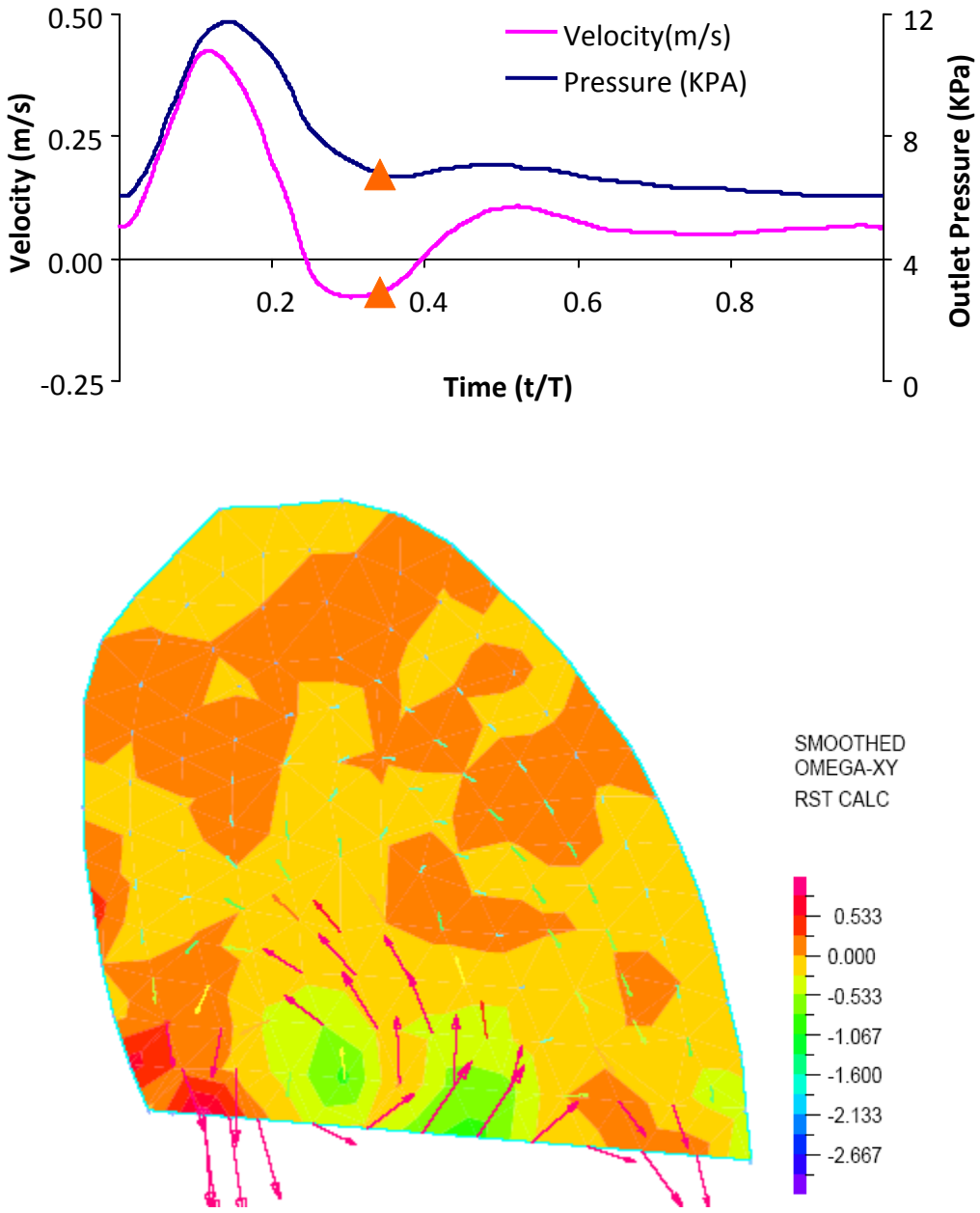

Figure 3-35. Contours of vorticity in the plane of symmetry of the aneurysm (x-y plane) at t/T =0.342 (orange triangle in the top inset). Vorticity units shown by the color scale are sec^{-1}. Velocity vectors are superposed on the vorticity contours.

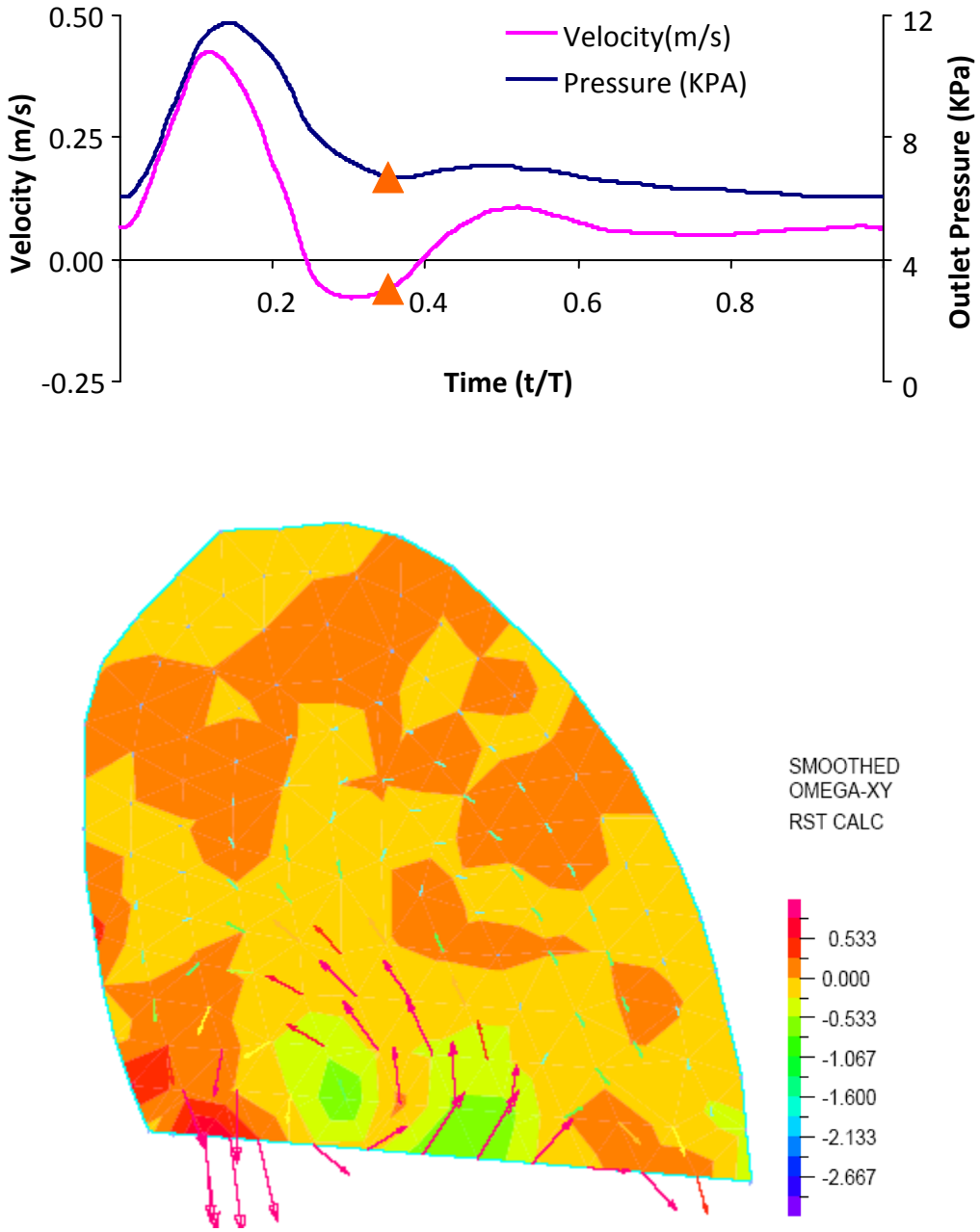

Figure 3-36. Contours of vorticity in the plane of symmetry of the aneurysm (x-y plane) at t/T =0.35 (orange triangle in the top inset). Vorticity units shown by the color scale are sec^{-1}. Velocity vectors are superposed on the vorticity contours.

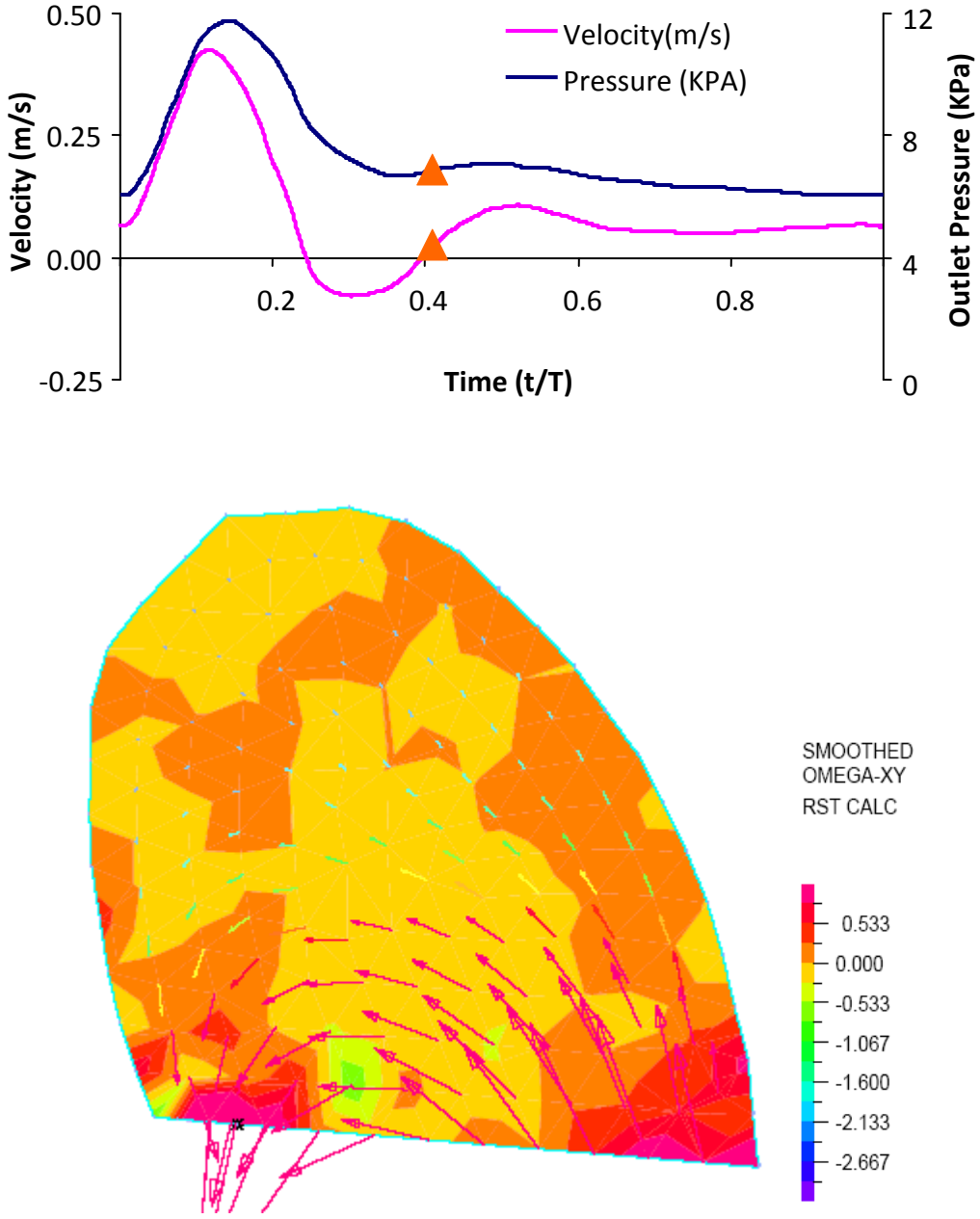

Figure 3-37. Contours of vorticity in the plane of symmetry of the aneurysm (x-y plane) at t/T =0.41 (orange triangle in the top inset). Vorticity units shown by the color scale are sec^{-1}. Velocity vectors are superposed on the vorticity contours.

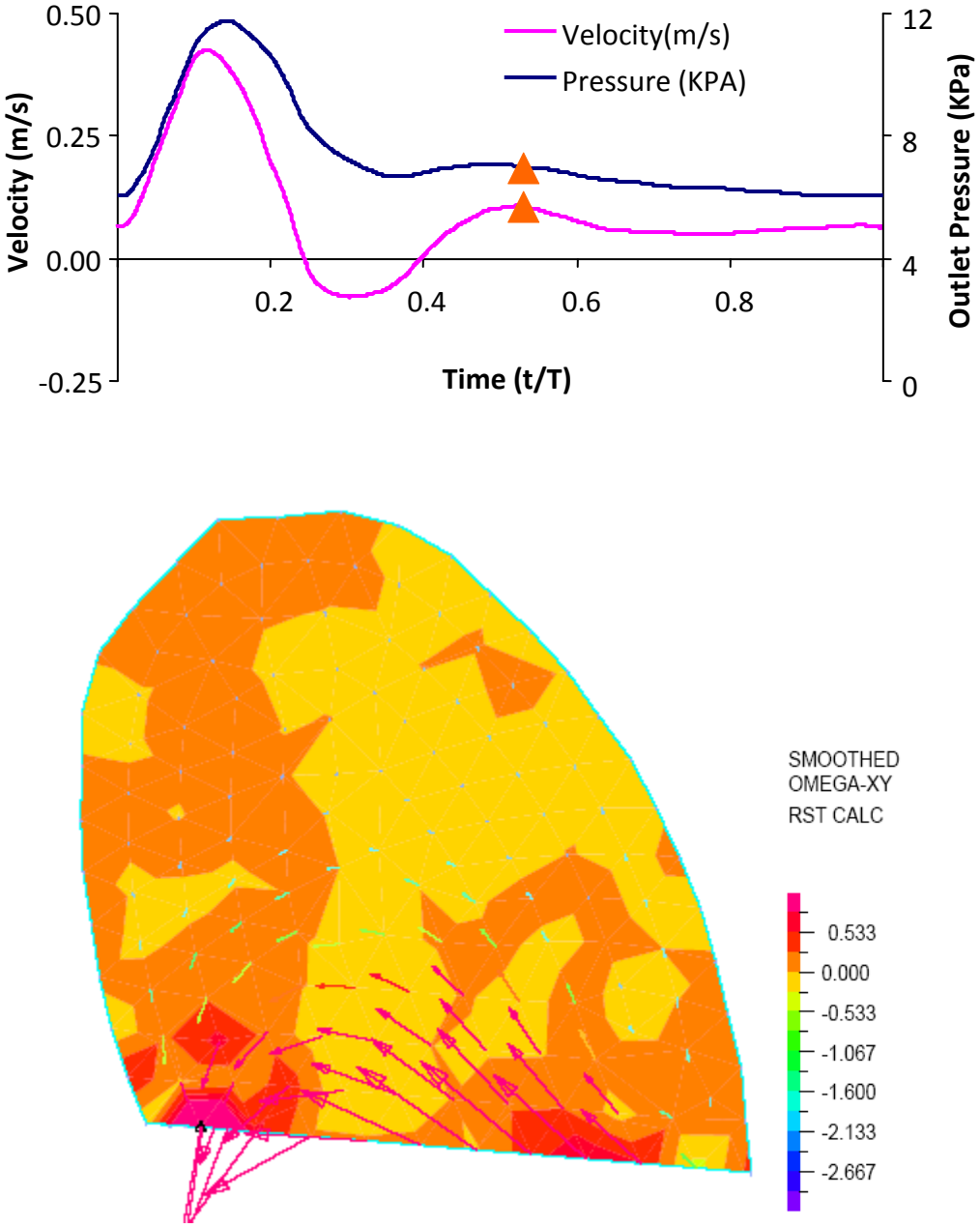

Figure 3-38. Contours of vorticity in the plane of symmetry of the aneurysm (x-y plane) at t/T =0.53 (orange triangle in the top inset). Vorticity units shown by the color scale are sec^{-1}. Velocity vectors are superposed on the vorticity contours.

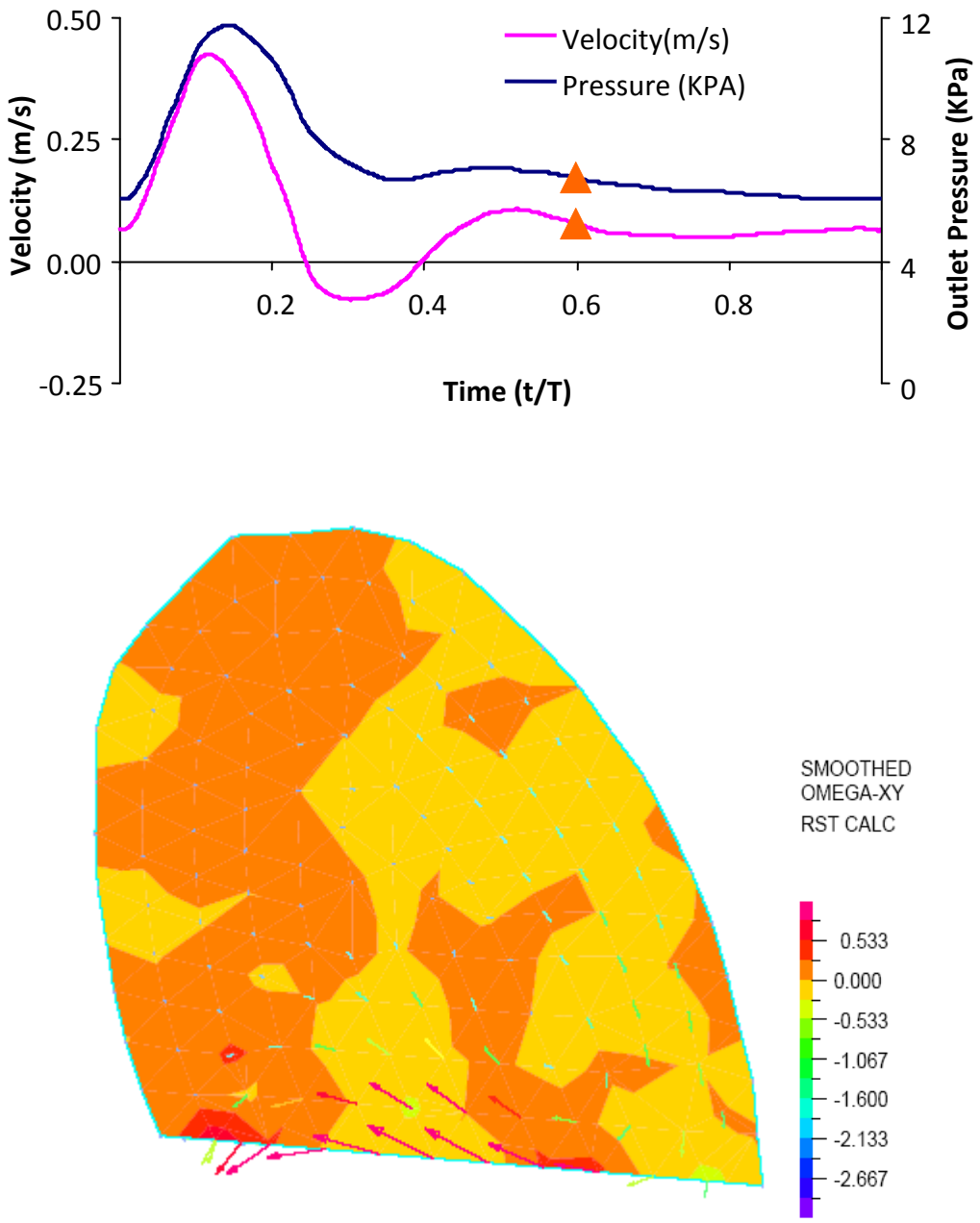

Figure 3-39. Contours of vorticity in the plane of symmetry of the aneurysm (x-y plane) at t/T =0.5975 (orange triangle in the top inset). Vorticity units shown by the color scale are sec^{-1}. Velocity vectors are superposed on the vorticity contours.

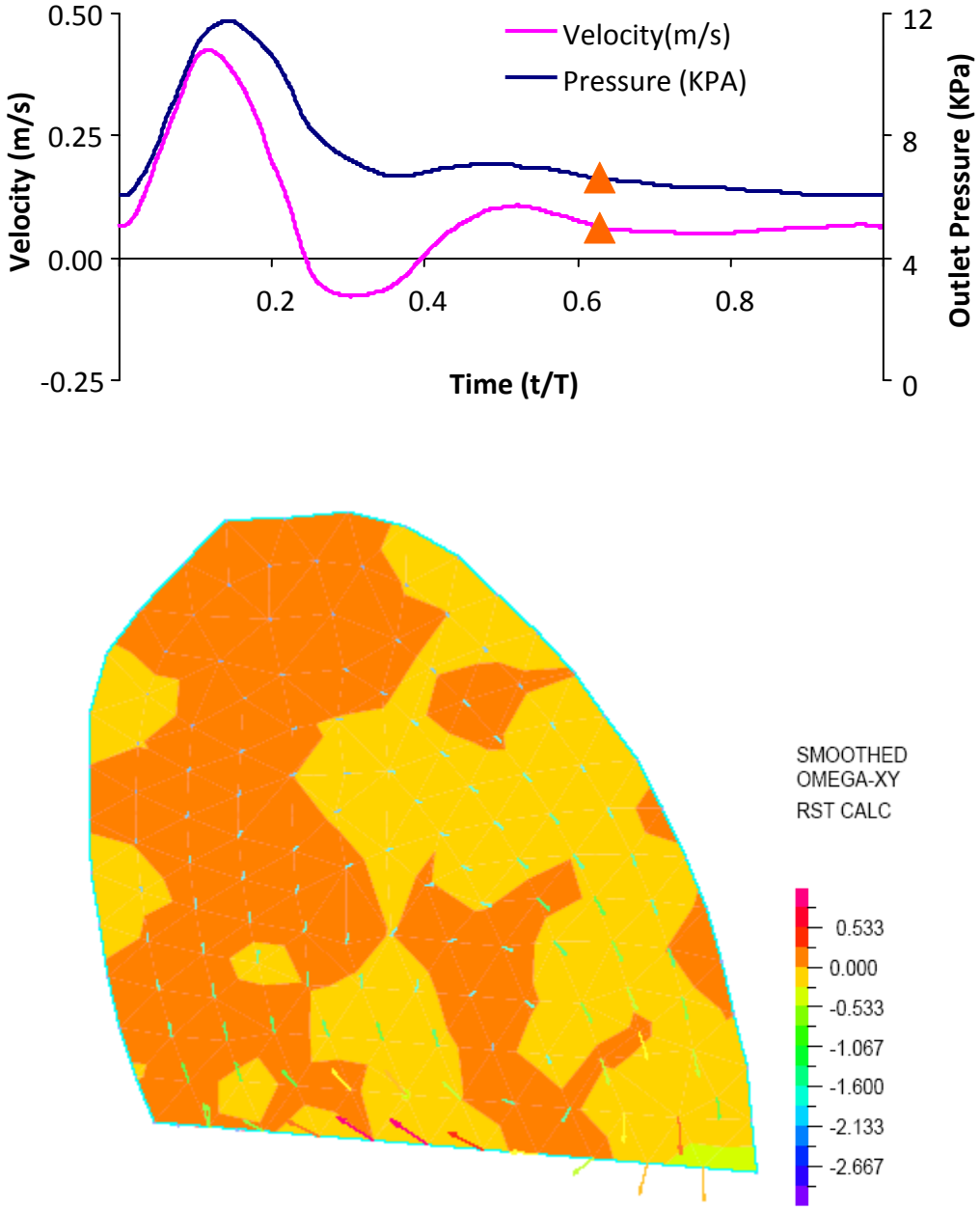

Figure 3-40. Contours of vorticity in the plane of symmetry of the aneurysm (x-y plane) at t/T =0.6275 (orange triangle in the top inset). Vorticity units shown by the color scale are sec^{-1}. Velocity vectors are superposed on the vorticity contours.

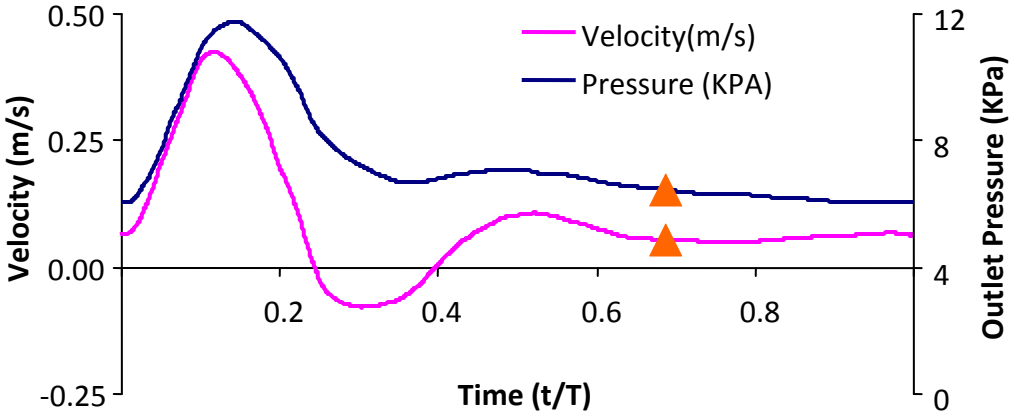

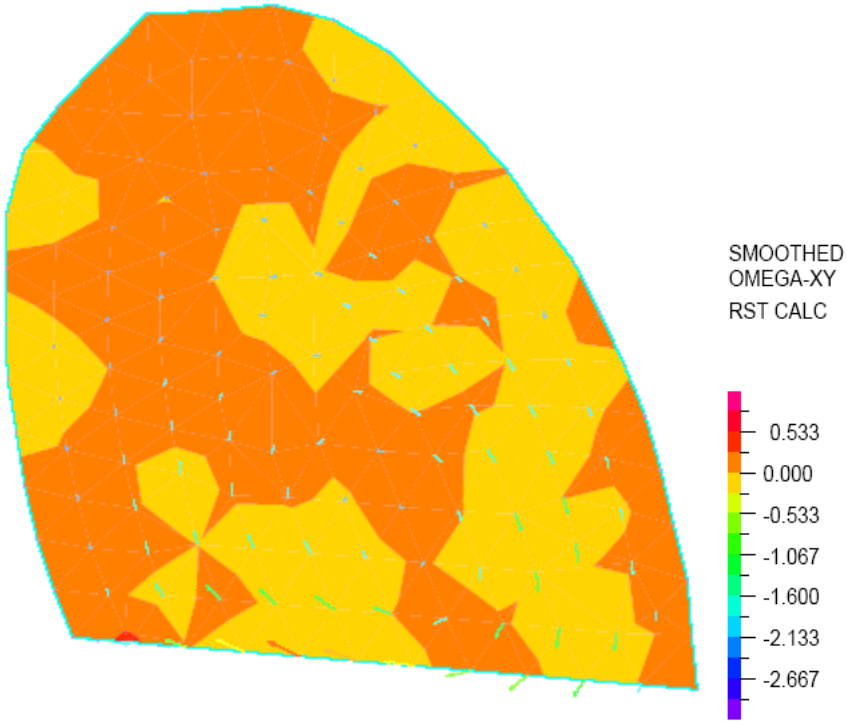

(r)

Figure 3-41. Contours of vorticity in the plane of symmetry of the aneurysm (x-y plane) at t/T =0.6875 (orange triangle in the top inset). Vorticity units shown by the color scale are sec^{-1}. Velocity vectors are superposed on the vorticity contours.

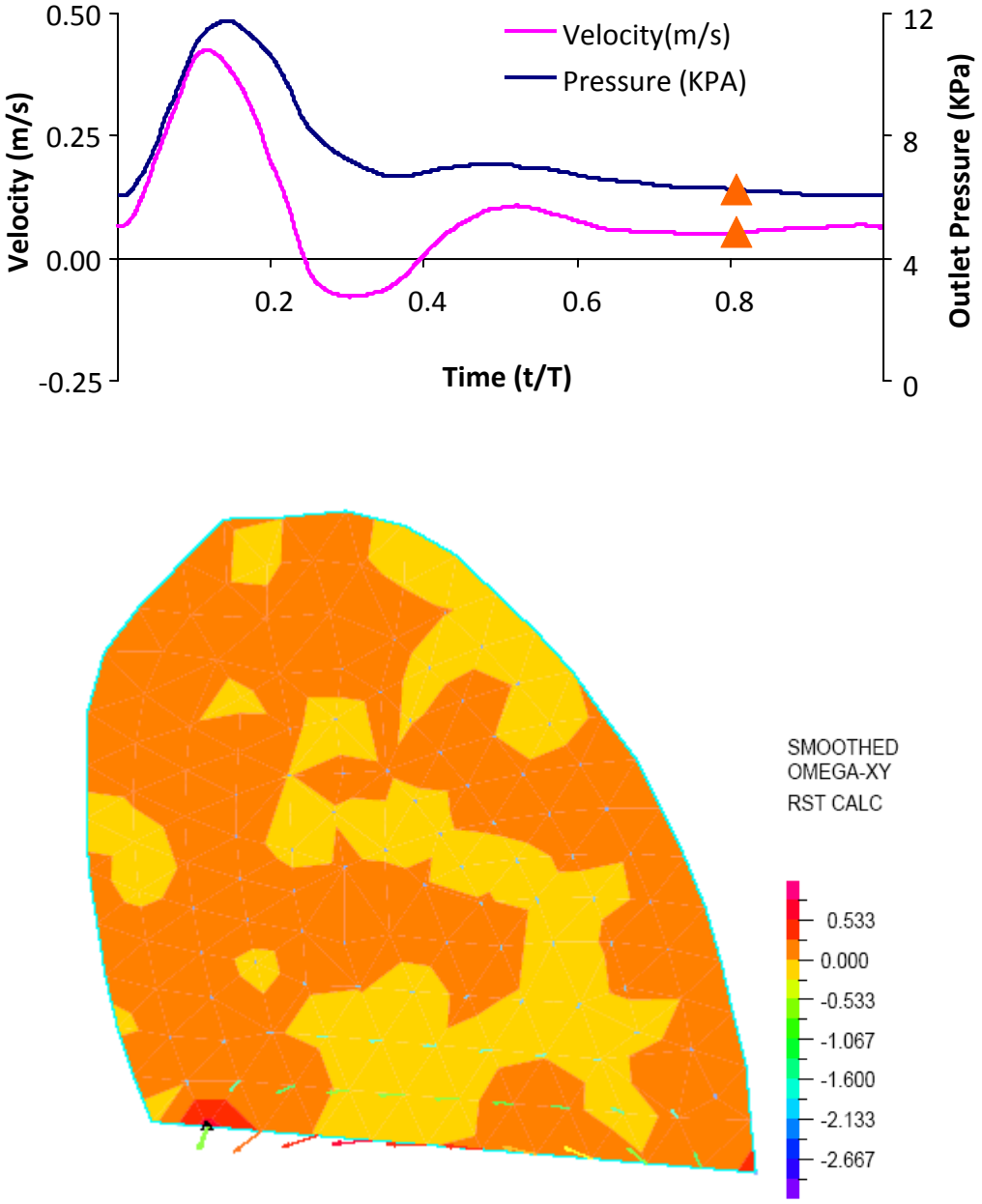

(s)

Figure 3-42. Contours of vorticity in the plane of symmetry of the aneurysm (x-y plane) at t/T =0.8075 (orange triangle in the top inset). Vorticity units shown by the color scale are sec^{-1}. Velocity vectors are superposed on the vorticity contours.

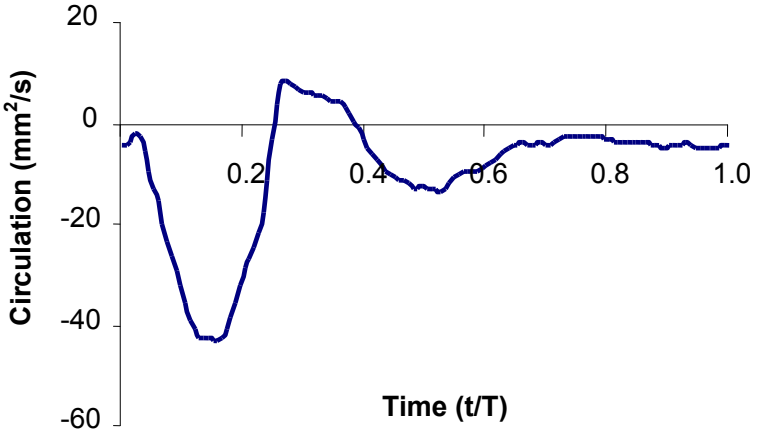

Figure 3-43. The hydrodynamic circulation in the plane of symmetry of the aneurysm sac.

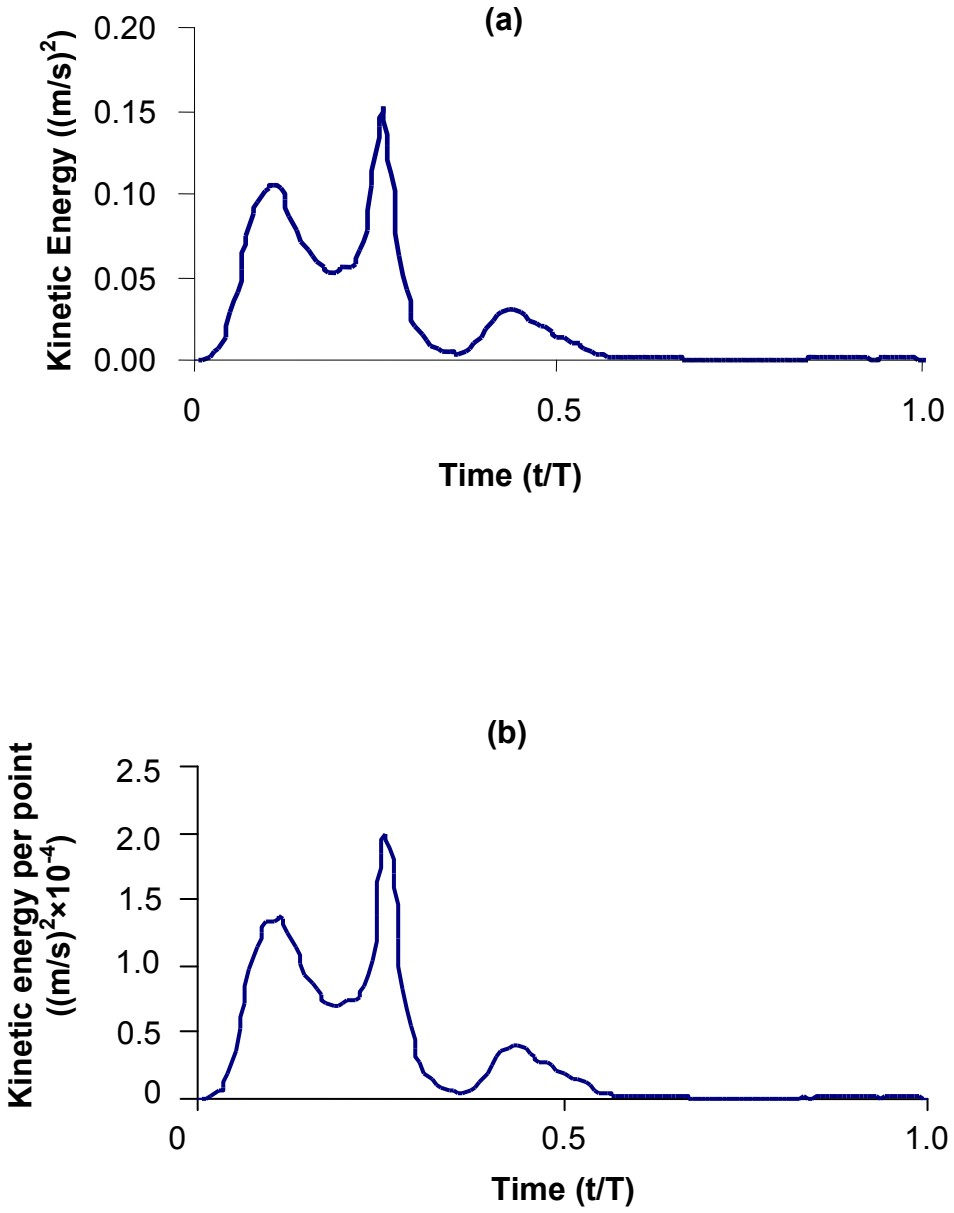

Figure 3-44 (a) The total kinetic energy inside the half aneurysm sac (based on 765 points). (b) The kinetic energy per point inside half aneurysm sac.

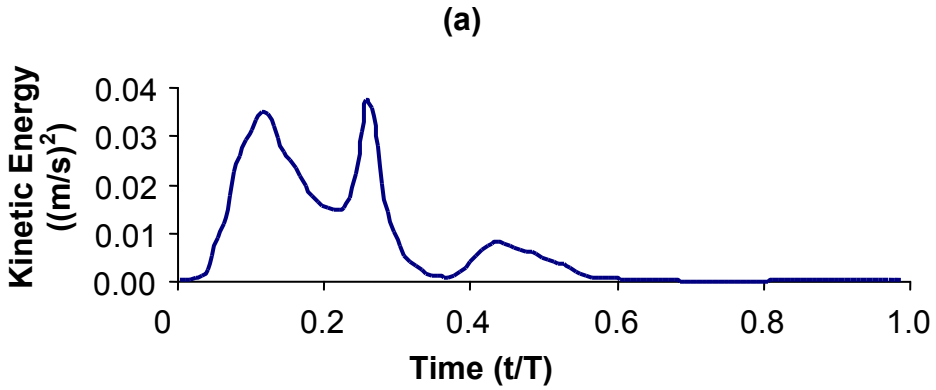

Figure 3-45 (a) The total kinetic energy on the symmetrical plane of the aneurysm sac (151 points)

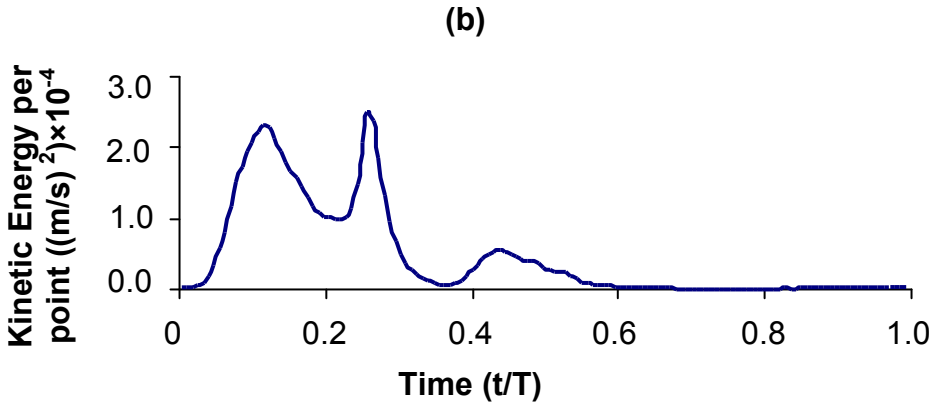

Figure 3-45 (b) The kinetic energy per point on the symmetrical plane of the aneurysm sac.

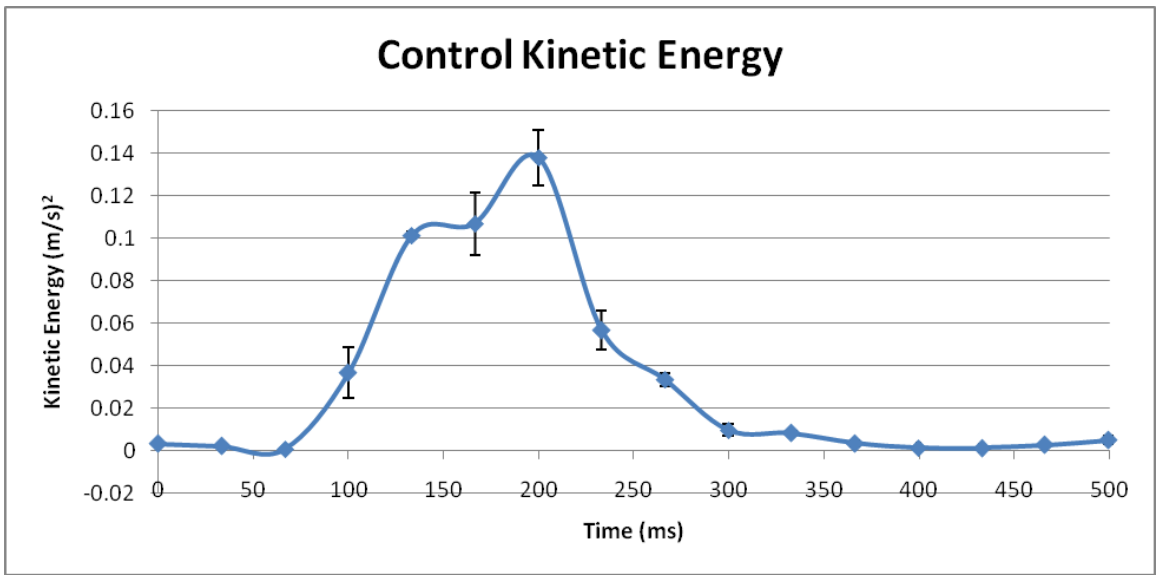

Figure 3-45 (c) The experimental kinetic energy from Trager 2010 (144 points)

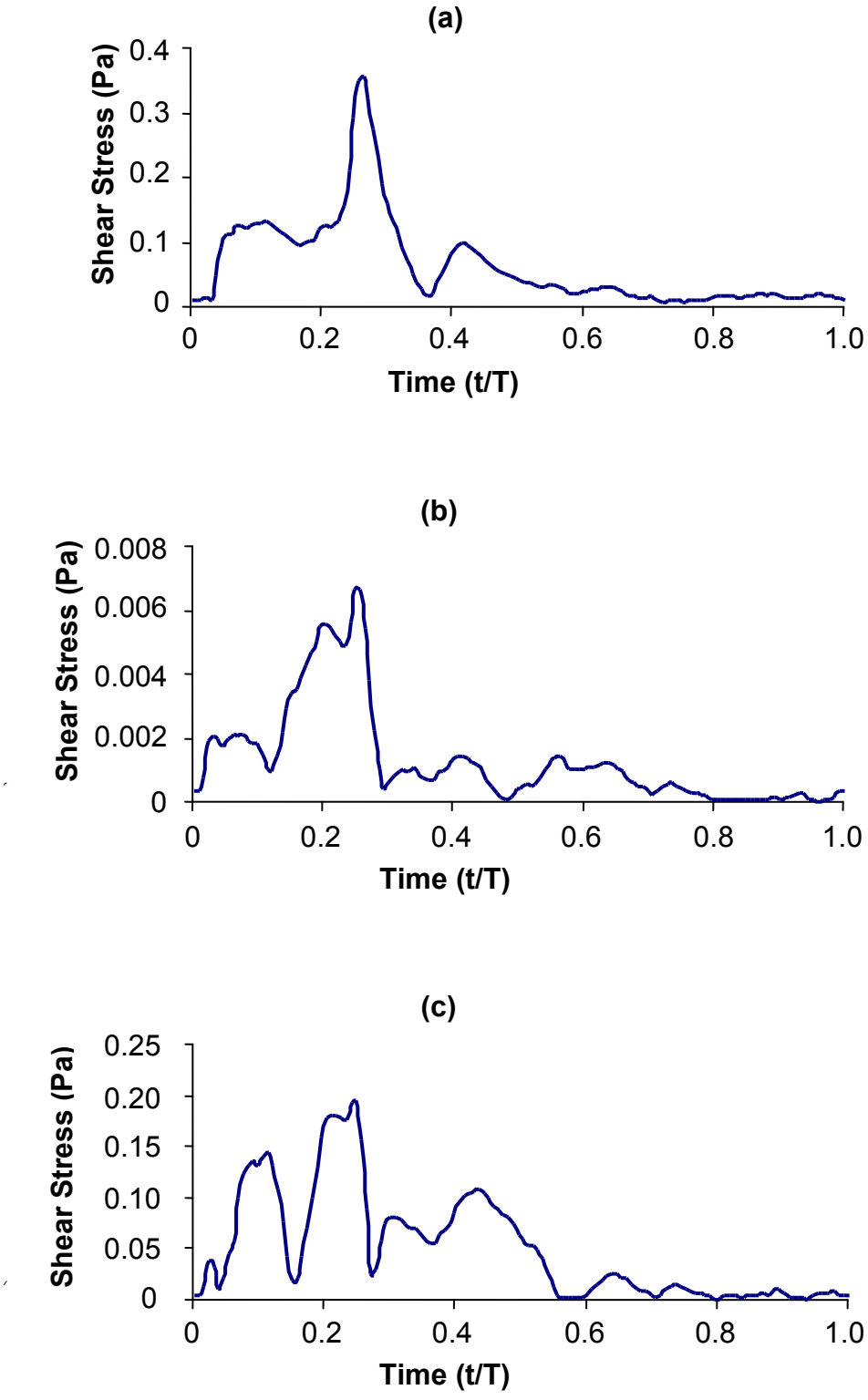

Figure 3-46. The shear stress in proximal neck (a), dome (b) and distal neck (c). See Figure 3-4 for the exact location of the shear stress

CHAPTER 4. DISCUSSION

Computational fluid-structure-interaction (FSI) has recently seen wide-spread use in the field of hemodynamics, particularly when flow in the major arteries is considered. The advantage of the use of FSI over CFD alone lies in the fact that the relation between pressure and flow (or pressure and velocity) can be elucidated and predictions of pressure drops in the pulsatile environment are therefore realistic. CFD calculations in a rigid wall environment do provide insight into the detail flow patterns in the physiological range, however the relation of these flow patterns to the physiological pressure waveform, the phasic relation between the pressure and flow and the mutual influence the wave propagation speed has on both pressure and flow could not be elucidated on the basis of CFD alone, since wave propagation speed in the rigid environment is too high and the energy exchange between the forward moving flow and the transverse flow into and out of the expanding arteries is missing. In addition, when using rigid wall calculations, the exit pressure is usually set to zero or some other constant value with disregard to the impedance distal to the truncated vascular bed of interest. Nevertheless, while the use of FSI is an improvement over CFD when considering hemodynamics, limitations persist. For example, the axial as well as the transverse traction at the inlet and outlets of the computational domain have to be kept unchanged to achieve a convergent solution. One way to minimize the influence of such obviously non-physiological boundary conditions is to extend the inlet and outlet tubes so as to move such conditions away from the region of interest (ROI). However, doing so comes at the expense of changing the details of the

entrance flow into the ROI which casts larger errors in calculations of higher order variables that are derived from the detailed flow patterns such as the wall shear stress.

In FSI the computational flow domain requires in addition to all other boundary conditions also inlet and outlet conditions on the flow domain. The common way to specify such conditions is to impose flow at the inlet and pressure at the outlet. In case of multiple exits from the computational domain, the specification of the various pressures is very important in order to achieve the desired mass flow ratios through the various branches. In this particular experiment there was one inlet and five outlets. Due to technical limitations it was not possible to measure the pressure simultaneously at all five outlets: the descending aorta, the right vertebral artery, the right subclavian artery, the left common carotid artery and the left subclavian artery. Since all 5 exit branches in the in vitro experiment were connected together before returning to the pump reservoir even if sufficient number of transducers were available, pressure measured in the small branches would have been effected by descending aorta pressure and vice versa. Alternating transducers has proven to be futile as well, since just the act of replacing the transducers at the various branches in itself produced enough variability in the pressure waveform to negate the production of a stable meaningful solution. To overcome such difficulties, in silico experiments on vascular geometries obtained from humans rely on the known properties of the vascular bed distal to the ROI and calculations of the unknown exit pressure from known velocity and known input as well as output impedance. In our experiment the distal impedance is not well characterized. Therefore detailed impedance calculations could not be executed.

Although directly applicable to the human circulation, three methods to obtain the unknown outflow condition have been developed and presented in the literature. The simplest one is resistance boundary condition (R-BC) that is based on the assumption that pressure and flow rate at each outlet are linearly dependent. [Grinberg, 2008]. However, this assumption ignores wave propagation and therefore it can generate aberrant pressure values in situations of flow reversal [Vignon-Clementtel, 2010]. The second method makes use of the Windkessel model to generate the boundary condition and the third method employs the impedance. In essence the second and the third method are similar in a sense that they use the impedance of the circulation distal to the truncated vascular bed used in the computations. The difference between the two lies in the complexity of the model used to construct the impedance.

To make use of the Windkessel model, we need to estimate the values of resistance (R), compliance (C), and inductance (L), of the experimental system for two compartments – one compartment which consists of the model itself and one compartment distal to the exits – and thus estimate the outlet pressure from inlet pressure and inlet flow rate [Berger, 1992]. However, the model parameters cannot be estimated from the available data.

Transmission line theory has not been used yet in the calculation of outlet flow conditions. An initial attempt was made to compute the outlet pressure using transmission line theory. However, the application of the obtained pressure at the outlet did not yield the expected flow patterns. The reasons for the inadequacy of the results from transmission line theory probably lie in the fact that an attempt was made only to project the changes between the inlet and the outlet while disregarding the rest

of the circuit back to the pump reservoir and its possible interaction with the model. Also, the expected small velocities in the aneurysm may not have been captured by the extrapolation of the inlet pressure by the linear one dimensional theory.

In this investigation, we selected a dataset for the inlet and outlet boundary conditions which is available in the literature [Raines, 1974]. The advantage of this set is that the pressure flow relation is carefully documented. However, the drawback of this dataset is that it does not represent our experimental conditions precisely. Particularly, the beat duration of this dataset is twice as long as the one used in our experiments. Simply rescaling the waveforms duration will not yield the desired effect since the shape of the waveforms themselves depends also on the frequency of the pulsatility. Therefore, quantitative differences between the numerical and experimental results are expected. Nevertheless, the numerical results do demonstrate qualitative agreement with the flow patterns that were observed experimentally. For example, the peak flow rate was set to 25 ml/s in the model, and the flow ratio between the four small branches and the descending aorta is very close to the experiment. The flow pattern in the model of aneurysm sac shows similarities with PIV images and clearly catch the vortex generation, immigration and dissipation out of the aneurysm sac. The kinetic energy can help reveal the activity level inside the aneurysm sac and kinetic energy in one cycle in the model changes in a similar way as the experimental results.

As the velocity field is elucidated, the wall shear stress can be evaluated. In this model the wall shear stress at the dome is low. It is well understood that the rabbit elastase induced aneurysm is not a model suitable for aneurysm rupture. Nevertheless,

these computational results are supported by low intraaneurysmal wall shear stress values that were obtained *in vitro* in the same model (Seong, 2007), and in a rigid wall computational study [Zeng, 2010]. In Zeng's paper, for high aspect ratio cases (where the dome height vs. neck width ratio is 2.1), the wall shear stress in the dome is reported to be between 0 and 0.05 Pa. For the low aspect ratio cases (where dome height vs. neck width ratio is 1.0), the wall shear stress in the dome is reported to be between 0.4 to 0.6 Pa. In our model the aspect ratio is about 1.4, closer to the low aspect ratio case, but the shape of aneurysm is similar to the high aspect ratio case. The maximum wall shear stress in the dome is about 0.0065 Pa. Although the values differ, our results show similarity with their study in a sense that minimum wall shear stress occurs in the dome and increases along the neck. Whether this low oscillatory shear is associated with endothelial cell necrosis, wall denudation of the endothelium and subsequent thrombosis at the aneurysm dome in this model as suggested by [Kadirvel, 2007] is still debatable.

In order to utilize this FSI model for optimization of flow diverters or other aneurysm flow altering devices better control of the inflow/outflow boundary conditions is required. The use of wave propagation theory to predict the outlet pressure from inlet pressure and/or flow is a possibility that needs to be investigated. While the distances travelled are relatively short, wave propagation is from the ascending aorta to five exits. As the model undergoes notable geometrical changes, it is reasonable to expect that the pressure waveforms at the various exits differ from each other not only in magnitude but also in shape. In this investigation we assumed for simplicity that the outlet pressures at these four small branches are 0.6 mmHg

lower than that of the descending aorta, which induces rapid low level oscillations in the flow rates through these branches. A more comprehensive consideration of wave propagation along all branches, will, of course, generate different pressure waves at the five outlets, but might be able to smooth out the flow waveforms.

CHAPTER 5. CONCLUSIONS

Animal experiments and recent clinical trials of flow diverters [Sadasivan 2009; Kallmes 2007 &2009, Kulcsar 2010, Fiorella 2008 & 2010, Lylyk 2009] have demonstrated the utility of this new technology for the treatment and exclusion of brain aneurysms from the circulation. The arduous task of optimization of the technology is just beginning. One such initial effort has been conducted by our lab using a mock circulatory loop with a model aneurysm using PIV. While experimental techniques are a valid approach to such an optimization, computer based models are ideally suited for such a task. Once the mathematical model has been setup and validated, it is relatively easy to make changes to the design parameters of the device and investigate changes of the hemodynamics thereof. Further, computer modeling can reduce the cost of the design iterations since no actual devices need to be constructed for each iterative step.

The FSI solution strategy was first tested on a single tube since a theoretical solution is available for such flow both in a rigid and flexible tube under pulsatile flow conditions. After the solution strategy was successfully developed, the FSI was applied to a model vascular bed, the same one that was used in the experiments, to prepare a computational tool which can help elucidate the hemodynamics inside the aneurysm sac.

This study shows that a successful FSI simulation, even of a linearly elastic model with one inlet and five outlets depends upon accurate inlet/outlet flow and pressure waves and the phasic relation which couples the two. Experimental data

needs to be carefully examined to ensure that pressure and flow match such that reasonably well behaved impedance relates the two. Post processing of the numerical results is needed to examine the pressure gradient between the inlet and outlet of the flow domain. Unreasonable variations in the pressure gradient are good indicator that the phasic pressure-flow relationship is inaccurate.

Further development of this FSI model will allow simulations of this arterial bed with flow diverters of various designs to help optimize the changes in local hemodynamics due to such devices. The additional challenge here is that the very thin wires of the flow diverter will have to be meshed as a solid with different properties than the wall and the fluid mesh around these thin wires will have to have an increased resolution resulting in a mesh of much larger numbers of elements which ultimately will require a substantial amount of computing resources.

REFERENCES

Aenis, M., Stancampiano, A.P., Wakhloo, A.K., Lieber, B.B., "Modeling of Flow in a Straight Stented and Nonstented Side Wall Aneurysm Model", Journal of Biomechanical Engineering 199(1997):206-212.

Altes, T.A., Cloft, H.J., Short, J.G., DeGast, A., Do, H.M., Helm, G.A., Kallmus, D.F., "Creation of Saccular Aneurysms in the Rabbit: a Model Suitable for Testing Endovascular Devices", American Journal of Roentgenology 174(2000):349-354.

American Heart Association (AHA), "Heart Disease and Stroke Statistics – 2009 update", 2009.

Barath, K., Cassot, F., Rufenacht, D. A., and Fasel, J. H. D., "Anatomically Shaped Internal Carotid Artery Aneurysm an vitro Model for Flow Analysis to Evaluate Stent effect," AJNR Am. J. Neuroradiol., 25 (2004): 1750–1759.

Bathe, K.J., Ledezma, G.A., "Benchmark Problems for Incompressible Fluid Flows with Structural Interactions", Computers & Structures 85 (2007): 628-644

Bathe, K.J., "Finite Element Procedure", 2006

Bathe, K.J, Zhang, H., "Finite Element Developments for General Fluid Flows with Structural Interactions", Int. J. Numer. Meth. Engng 2004; 60:213–232

Berger SA, "Flow in Large Blood Vessels," Fluid Dynamics in Biology, Contemporary Math. Series, Eds. AY. Cheer and c.P. Van Dam, Amer. Math. Sec., Providence, 1992, pp. 479-518.

Boussel L, Rayz V, Martin A, Acevedo-Bolton G, Lawton MT, Higashida R, Smith WS, Young WL, Saloner D. "Phase-Contrast Magnetic Resonance Imaging Measurements in Intracranial Aneurysms in vivo of Flow Patterns, Velocity Fields, and Wall Shear Stress: Comparison with Computational Fluid Dynamics", Magn Reson Med. 2009 Feb;61(2):409-17.

Brisman JL, Song JK, Newell DW., "Cerebral aneurysms", N Engl J Med. 2006 Aug 31;355(9):928-39.

Caton,G., Levy,D.L., Lasheras, J.C., and Nelson, P.K., "Flow Changes Caused by the Sequential Placement of Stents Across the Neck of Sidewall Cerebral Aneurysms", J. Neurosurg., 103 (2005): 891–902.

Carew TE, Vaishnav R.N., Patel D.J, "Compressibility and Constuitive Equation of Arterial Wall", Circ. Res. 23(1968,): 61-68

Castro MA, Putman CM, Cebral JR., "Patient-specific Computational Modeling of Cerebral Aneurysms with Multiple Avenues of Flow from 3D Rotational Angiography Images", Acad Radiol. 13(2006): 811-21.

Cebral, J.R. and R. Lohner, "Efficient Simulation of Blood Flow Past Complex Endovascular Devices Using an Adaptive Embedding Technique", IEEE Transactions on Medical Imaging", 24(2005): 468-476

Cekirgea, S.H., K. Yavuza, S. Geyika and I. Saatcia, "HyperForm Balloon-Assisted Endovascular Neck Bypass Technique to Perform Balloon or Stent-Assisted Treatment of Cerebral Aneurysms", American Journal of Neuroradiology 28 (2007):1388-1390

Chuong CJ, Fung YC., "On residual stresses in arteries." J Biomech Eng. 108(1986):189-92

Chien A, Tateshima S, Castro M, Sayre J, Cebral J, Viñuela F , "Patient-specific Flow Analysis of Brain Aneurysms at a Single Location: Comparison of Hemodynamic Characteristics in Small Aneurysms.", Med Biol Eng Comput. 46(2008):1113-20

Cloft, H.J., Altes, T.A., Marx, W.F., Raible, R.J., Hudson, S.B., Helm, G.A., Mandell, J.W., Jensen, M.E., Dion, J.E., Kallmes, D.F., "Endovascular Creation of an in vivo Bifurcation Aneurysm Model in Rabbits", Radiology 213(1999):223-228

Fiorella D, Woo HH, Albuquerque FC, Nelson PK, "Definitive Reconstruction of Circumferential, Fusiform Intracranial Aneurysms with the Pipeline Embolization Device", Neurosurgery. 2008 May;62(5):1115-20; discussion 1120-1.

Fiorella D, Hsu D, Woo HH, Tarr RW, Nelson PK, "Very Late Thrombosis of a Pipeline Embolization Device Construct: Case Report", Neurosurgery. 2010 Sep;67 (3 Suppl Operative):E313-4; discussion E314.

Ford MD, Nikolov HN, Milner JS, Lownie SP, Demont EM, Kalata W, Loth F, Holdsworth DW, Steinman DA, "PIV-measured versus CFD-predicted Flow Dynamics in Anatomically Realistic Cerebral Aneurysm Models", J Biomech Eng. 130(2008):021015

Ford MD, Stuhne GR, Nikolov HN, Habets DF, Lownie SP, Holdsworth DW, Steinman DA., "Virtual Angiography for Visualization and Validation of Computational Models of Aneurysm Hemodynamics", IEEE Trans Med Imaging. 24(2005): 1586-92

Geremia G, Haklin M, Brennecke L., "Embolization of Experimentally Created Aneurysms with Intravascular Stent Devices", AJNR Am J Neuroradiol, 15(1994):1223-31.

Hoi Y, Woodward SH, Kim M, Taulbee DB, Meng H., "Validation of CFD Simulations of Cerebral Aneurysms with Implication of Geometric Variations", J Biomech Eng, 128(2006): 844-51

Humphrey J.D., "Mechanics of the Arterial Wall: Review and Directions", Critical Review in Biomedical Engineering, 23(1995):1-62

International Subarachnoid Aneurysm Trial (ISAT) Collaborative Group, "International Subarachnoid Aneurysm Trial (ISAT) of neurosurgical clipping versus endovascular coiling in 2143 patients with ruptured intracranial aneurysms: a randomised trial" Lancet, 360(2002): 1267-1274.

Kadirvel R, Ding YH, Dai D, Zakaria H, Robertson AM, Danielson MA, Lewis DA, Cloft HJ, Kallmes DF, "The Influence of Hemodynamic Forces on Biomarkers in the Walls of Elastase-Induced Aneurysms in Rabbits", Neuroradiology. 2007 Dec;49(12):1041-53.

Kallmes DF, Ding YH, Dai D, Kadirvel R, Lewis DA, Cloft HJ. "A New Endoluminal, Flow-Disrupting Device for Treatment of Aaccular Aneurysms", Stroke. 2007 Aug;38(8):2346-52.

Kallmes DF, Ding YH, Dai D, Kadirvel R, Lewis DA, Cloft HJ, "A Second-Generation, Endoluminal, Flow-Disrupting Device for Treatment of Saccular Aneurysms", AJNR Am J Neuroradiol. 2009 Jun;30(6):1153-8.

Kassell NF, Torner JC, Haley EC Jr, Jane JA, Adams HP, Kongable GL, "The International Cooperative Study on the Timing of Aneurysm Surgery. Part 1: Overall management results", J. Neurosurg. 1990 Jul;73(1):18-36.

Ku DN, Giddens DP, Zarins CK, Glagov S., "Pulsatile Flow and Atherosclerosis in the Human Carotid Bifurcation. Positive Correlation Between Plaque Location and low Oscillating Shear Stress", Arteriosclerosis. 1985 May-Jun;5(3):293-302.

Kulcsár Z, Ernemann U, Wetzel SG, Bock A, Goericke S, Panagiotopoulos V, Forsting M, Ruefenacht DA, Wanke I., "High-Profile Flow Diverter (silk) Implantation in the Basilar Artery: Efficacy in the Treatment of Aneurysms and the Role of the Perforators", Stroke. 2010 Aug;41(8):1690-6.

Lieber, B.B., Livescu, V., Hopkins, L.N., Wakhloo. A.K., "Particle Image Velocimetry Assessment of Stent Design Influence on intra-Aneurysmal Flow." Annals of Biomedical Engineering 30(2002):768-777.

Lieber BB, Gounis MJ, "The Physics of Endoluminal Stenting in the Treatment of Cerebrovascular Aneurysms", Neurol Res. 2002; 24 Suppl 1:S33-42.

Lieber BB, Nikolaidis N, Wakhloo AK: Flow Patterns in an Intracranial Side Wall Aneurysm Model Using Particle Image Velocimetry. Adv Bioeng, ASME Publication, 1998; 39: 49-50.

Lieber BB, Sadasivan C, "Hemodynamics, Macrocirculatory" in "Encyclopedia of Biomaterials and Biomedical Engineering", 2006, Taylor & Francis

Lieber BB, Stancampiano AP, Wakhloo AK, "Alteration of Hemodynamics in Aneurysm Models by Stenting: Influence of Stent Porosity", Ann Biomed Eng. 1997 May-Jun; 25(3):460-9.

Liou, T., Liou, S., Chu, K., "Intra-aneurysmal Flow with Helix and Mesh Stent Placement across Side-Wall Aneurysm Pore of a Straight Parent Vessel" Journal of Biomechanical Engineering 36(2004):36-43.

Lubicz, B., Xavier Leclerc, Jean-Yves Gauvrit, Jean-Paul Lejeune, and Jean-Pierre Pruvo, "Three-Dimensional Packing with Complex Orbit Coils for the Endovascular Treatment of Intracranial Aneurysms", AJNR Am. J. Neuroradiol., 2005; 26: 1342 - 1348.

Lubicz, B. Xavier Leclerc, Jean-Yves Gauvrit, Jean-Paul Lejeune, and Jean-Pierre Pruvo. "Endovascular Treatment of Intracranial Aneurysms with Matrix Coils: A Preliminary Study of Immediate Post-treatment Results", AJNR Am. J. Neuroradiol., 2005; 26: 373 - 375.

Lylyk, P., Ceratto, R., Hurvitz, D., Basso, A., "Treatment of a Vertebral Dissecting Aneurysm with Sstents and Coils: Technical CaseRreport." Neurosurgery 43(1998):385-388.

Lylyk P, Miranda C, Ceratto R, Ferrario A, Scrivano E, Luna HR, Berez AL, Tran Q, Nelson PK, Fiorella D., "Curative Endovascular Reconstruction of Cerebral Aneurysms with the Pipeline Embolization Device: the Buenos Aires Experience", Neurosurgery. 2009 Apr; 64(4):632-42; discussion 642-3; quiz N6.

Massoud, T.F., Turjman, F., Ji, C., Vinuelas, F., Guglieli, G., Gobin, Y.P., Duckwiler, G.R., "Endovascular Treatment of Fusiform Aneurysms with Stents and Coils: Technical Feasibility in a Swine Model." American Journal of Neuroradiology 16(1995):1953-1963.

Maurice-Williams, R. S. and Lafuente, J., "Intracranial Aneurysm Surgery and Its Future", Journal of the Royal Society of Medicine 96(2003):540-543.

McKissock, W., Richardson, A., Walsh, L., "Anterior Communicating Aneurysms: A Trial of Conservative and Surgical Treatment", Lancet 285 (Apr. 1965):873-876.

McKissock, W., Richardson, A., Walsh, L., "Middle-Cerebral Aneurysms", Lancet, 280(Sep. 1962):417-421.

McKissock, W., Richardson, A., Walsh, L., "Posterior-Communicating Aneurysms", Lancet 275(1960):1203-1206.

Milnor, WR, "Hemadyanics", 1989, 2nd edition, Williams & Wilkinns

Miskolczi, L., Guterman, L.R., Flaherty, J.D., Szikora I., Hopkins, L.N., "Rapid Aaccular Aneurysm Induction by Elastase Application in vitro." Neurosurgery 41(1997):220-229.

Miskolczi, L., Guterman, L.R., Flaherty, J.D., Hopkins, L.N., "Saccular Aneurysm. Induction by Elastase Digestion of the Arterial Wall: A New Animal Model", Neurosurgery 43(1998):595-600.

Mitchell, P., Gholkar, A., Vindlacheruvu, R. R., and Mendelow, A. D., "Unruptured Intracranial Aneurysms: Benign Curiosity or Ticking Bomb?" Lancet Neurol., 2004. 3: 85–92

Onizuka, M., Miskolczi, L., Gounis, M.J., Seong, J., Lieber, B.B., Wakhloo, A.K., "Elastase-Induced Aneurysms in Rabbits: Effect of Post-Construction Geometry onFinal Size." American Journal of Neuroradiology, 2006 May;27(5):1129-31.

Rayz VL, Boussel L, Acevedo-Bolton G, Martin AJ, Young WL, Lawton MT, Higashida R, Saloner D., "Numerical Simulations of Flow in Cerebral Aneurysms: Comparison of CFD Results and in vivo MRI Measurements", J Biomech Eng. 2008 Oct;130(5):051011.

Rhee, K., Han, M. H., and Cha, S. H., 2002, "Changes of Flow Characteristics by Stenting in Aneurysm Models: Influence of Aneurysm Geometry and Stent Porosity," Ann. Biomed. Eng., 30, pp. 894–904.

Raines JK, Jaffrin MY, Shapiro AH., "A Computer Simulation of Arterial Dynamics in the Human Leg. J Biomech. 1974 Jan;7(1):77-91.

Sadasivan C, Cesar L, Seong J, Wakhloo AK, Lieber BB., "Treatment of Rabbit Elastase-Induced Aneurysm Models by Flow Diverters: Development of Quantifiable Indexes of Device Performance Using Digital Subtraction Angiography", IEEE Trans Med Imaging. 2009 Jul;28(7):1117-25.

Sadasivan C, Cesar L, Seong J, Rakian A, Hao Q, Tio FO, Wakhloo AK, Lieber BB., "An Original Flow Diversion Device for the Treatment of Intracranial Aneurysms: Evaluation in the Rabbit Elastase-Induced Model", Stroke. 2009 Mar;40(3):952-8

Scotti C, Shu F, Vandenberghe S, Seong J, Antaki J, Lieber B, Finol E, "Validation of Abdominal Aortic Aneurysm Dynamics: A Comparative Analysis of PIV, CFD, and FSI", 2009 Summer Bioengineering Conference

Seong J, Sadasivan C, Onizuka M, Gounis MJ, Christian F, Miskolczi L, Wakhloo AK, Lieber BB. Morphology of Elastase-Induced Cerebral Aneurysm Model in Rabbit and Rapid Prototyping of Elastomeric Transparent Replicas. Biorheology, 2005; 42(5):345-61.

Seong J, Wakhloo AK, Lieber BB., "In vitro Evaluation of Flow Divertors in an Elastase-Induced Saccular Aneurysm Model in Rabbit.", J Biomech Eng. 2007 Dec;129(6):863-72.

Sforza DM, Putman CM, Scrivano E, Lylyk P, Cebral JR. "Blood-flow Characteristics in a Terminal Basilar Tip Aneurysm Prior to Its Fatal Rupture", AJNR Am J Neuroradiol. 2010 Jun; 31(6):1127-31.

Short, J.G., Fujiwara, N.H., Marx, W.F., Helm, G.A., Cloft, H.J., Kallmes, D.F., "Elastase-Induced Saccular Aneurysms in Rabbits: Comparison of Geometric Features with those of human aneurysms." American Journal of Neuroradiology 22(2001):1833-1837.

Simon SD, Lopes DK, Mericle RA., "Use of Intracranial Stenting to Secure Unstable Liquid Embolic Casts in Wide-Neck Sidewall Intracranial Aneurysms:, Neurosurgery, 2010 Mar;66(3 Suppl Operative):92-7; discussion 97-8.

Stehbens WE., "Histological Changes in Chronic Experimental Aneurysms Surgically Fashioned in Sheep", Pathology. 1997 Nov; 29(4):374-9.

Trager, A. "Evaluation of an Optimized Flow Diverting Device on Intra-Aneurysmal Flow and a Newly Developed Adjuvant Therapy" 2010, Ph.D. Dissertation, University of Miami

Tsuei YS, Matsumoto Y, Ohta M, Nakayama T, Ezura M, Takahashi A. "Vertebrobasilar Junction Fenestration with Dumbbell-Shaped Aneurysms Formation: Computational Fluid Dynamics Analysis", Surg Neurol. 2009 Dec;72 Suppl 2:S11-9.

Turjman F, Acevedo G, Moll T, Duquesnel J, Eloy R, Sindou M., "Treatment of Experimental Carotid Aneurysms by Endoprosthesis Implantation: Preliminary Report.", Neurol Res. 1993 Jun;15(3):181-4

Van Loock K, Menovsky T, Voormolen MH, Plazier M, Parizel P, De Ridder D, Maas AI, Hernesniemi JA. "Microsurgical Removal of Onyx HD-500 from an Aneurysm for Relief of Brainstem Compression", J Neurosurg. 2009 Nov 6.

Wakhloo, A.K., Lanzino, G., Lieber, B.B., Hopkins, L.N., "Stent for Intracranial Aneurysms: the Beginning of a New Endovascular Era?" Neurosurgery 43(1998):377-379

Wakhloo, A.K., Schellhammer, F., de Vries, J., Haberstroh, J., Schumacher, M., "Selfexpanding and Ballon-Expandable Stents in the Treatment of Carotid Aneurysms: an Experimental Study in a Canine Model." American Journal of Neuroradioloy, 15(1994):493-502

Westerhof, N., Stergiopulos, N., Noble, M.I.M., "Sanpshots of Hemodynbamics", Springer, 2005

Wolfe SQ, Farhat H, Moftakhar R, Elhammady MS, Aziz-Sultan MA. "Intraaneurysmal Balloon Assistance for Navigation Across a Wide-Necked Aneurysm", J Neurosurg. 2010 Jun; 112(6):1222-6.

Yu, S.C.M., Zhao, J.B., "A Steady Flow Analysis on the Stented and Non-Stented Sidewall Aneurysm Models." Medical Engineering & Physics 21(1999):133-141.

Zamir, M., "The Physics of Pulsatile Flow", Springer, 2005

Zeng, Z, Kallmes, D, Durka, M., Y. Ding, Lewis D., Kadirvel R., Robertson A., "Sensitivity of CFD Based Hemodynamic Results in Rabbit Aneurysm Models to Idealizations in Surrounding Vasculature", ASME Journal of Biomechanical Engineering, Vol 132 Sept 2010 091009

Zhang, H., Zhang, X., Ji S., Guo Y., Ledezma, G., Elabbasi N., deCougny H., "Recent Development of Fluid–Structure Interaction Capabilities in the ADINA system", 2003, Computers and Structures 81, 1071–1085

Zhao S.Z., X Y Xu and MW Collins, "The Numerical Analysis of Fluid–Solid Interactions for Blood Flow in Arterial Structures Part 1: a Review of Models for Arterial Wall Behaviour, and Part 2: Development of Coupled Fluid–Solid Algorithms", Proc Instn Mech Engrs 1998 Vol 212 (4):229-40